An Indoor Resource Optimisation for TDMA Incorporating a Convex Space Building Configuration and Accurate Ray-Tracing

by

Eamonn M. Kenny

Master of Science

A Thesis submitted to
The University of Dublin
for the degree of

Doctor of Philosophy

Department of Electrical and Electronic Engineering,
University of Dublin,
Trinity College

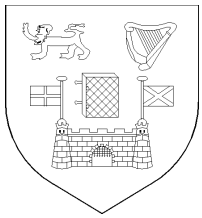

October, 2003

Declaration

This thesis has not been submitted as an exercise for a degree at any other University. Except where otherwise stated, the work described herein has been carried out by the author alone. This thesis may be borrowed or copied upon request with the permission of the Librarian, University of Dublin, Trinity College. The copyright belongs jointly to the University of Dublin and Eamonn M. Kenny.

Signature of Author .....

Eamonn M. Kenny October, 2003

Summary

The contents of this work are designed for planning wireless telecommunication systems in indoor environments with application intended for time division multiple access (TDMA) systems. The term resource optimisation mentioned in the title refers to the optimisation of the resources that make up a communication system, such as the power, server and mobile unit costs.

Defined here is a resource optimisation algorithm that uses at its core a ray-tracing engine. The ray-tracing provides propagation signal strength (coverage) information. The base stations are positioned within predefined cells contained in the building and can be moved subject to a number of constraints at each iteration of the optimisation. Each constraint is related to the capacity requirement of a user, in other words the signal to interference requirement.

For an optimisation procedure to be reliable, it is expected that the ray-tracing solution be calculated to a very high degree of accuracy so as to provide the algorithm with adequate information. Using a full wave solution such as an integral equation technique instead to give better results is virtually impossible due to the computational complexity of the problem. In the past authors have relied on empirical coverage calculations that are known to work excellently in outdoor models but are not at all reliable in indoor propagation due to the diffraction and reflection paths being neglected.

The problem using a ray-tracing engine at the heart of an optimisation algorithm is that it may require the continual creation of a visibility list every time a server is moved, if that visibility list is dependant on the location of the transmitter. Many well known ray-tracing algorithms depend on a visibility algorithm which assumes

the transmitter is at a fixed location. It will be shown that this is not the case for the new ray-tracing algorithm described here. This means that the ray-tracing allows the optimisation procedures to operate with reasonable computational times, while providing far more accurate propagation coverage in the building than empirical methods. The description of an algorithm that converts the building into convex spaces is one of the main achievements of this work, showing how the building is broken up, and how a visibility algorithm is formed.

The optimisation algorithms presented by previous authors use path-loss based models instead of signal to interference ratio based models. This is adequate for GSM but not for TDMA systems where the servers are not communicating directly with one another by cabling, in other words each acts as a separate entity.

The chapters of this thesis have a very deliberate progression, going through a process of building the inner workings of an optimisation tool before describing the optimisation itself. The majority of the work consists of using well-known ray-tracing methods such as method of images for reflections, uniform theory of diffraction (UTD) for diffraction paths, and transmissions through and inside different types of media.

The shortcomings of ray-tracing are highlighted and novel techniques to correct reflection, transmission and diffraction coefficients are presented in great detail.

A brief look at linear programming methods is followed by a downlink and uplink optimisation procedure married together with the ray-tracing results. The algorithm uses a method previously described in the literature, with considerable alteration making it novel in its own right. An attempt is then made to obtain good simulations of a TDMA system finding the best positions of the servers whilst giving the highest possible bit rates to the users of the system.

Acknowledgements

I would like to formally thank Enterprise Ireland for funding this PhD. The work on Software Tool for Indoor Wireless Resource Optimisation (STIWRO) helped to make up the contents of this thesis. The project was funded under the National Development Plan 2000-2006.

I want to thank Peter Cullen my previous supervisor for making this project possible and for his many hours in the past of editing my work to make it well polished and succinct. His friendship and encourage were invaluable.

I would also like to thank Prof. Frank Boland for taking on the supervision of my thesis during Peter's sabbatical.

Also to my colleagues Conor and Gerry. Conor was a great help and provided codes to produce comparisons with integral equation results and generally knocking ideas off. Gerry helped me understand the downlink and uplink optimisation problem.

Last but by no means least I would like to thank my wife Sandra for her encouragement and support.

Contents

List of Figures

List of Tables

List of Acronyms

BTS	Base Transceiver Station
CDMA	Code Division Multiple Access
CFIE	Combined Field Integral Equation
CGS	Conjugate Gradient Squares
EEC	Equivalent Edge Currents
EFIE	Electric Field Integral Equation
FDD	Frequency Domain Duplexing
FDTD	Finite Difference Time Domain
FTF	Fresnel Transition Function
GSM	Global System for Mobile Communciations
GTD	Geometrical Theory of Diffraction
ILDC	Incremental Length Diffraction Coefficient
RWG	Rao-Wilton-Glisson
MFIE	Magnetic Field Integral Equation
MoM	Method of Moments
PEC	Perfect Electric Conductor
PTD	Physical Theory of Diffraction
PTDEEC	Physical Theory of Diffraction Equivalent Edge Currents
RCS	Radar Cross-Section
SIR	Signal to Inteference Ratio
STIWRO	Software Tool for Indoor Wireless Resource Optimisation
SUMT	Sequential Unconstrained Minimisation Technique

TDD	Time Domain Duplexing
TDMA	Time Division Multiple Access
THP	Truncated Half-Plane
TIM	Tabulated Interaction Method
UE	Unit Equipment
UHF	Ultra High Frequency
UMTS	Universal Mobile Telecommunication System
UTD	Uniform Theory of Diffraction
WCDMA	Wide-band Code Division Multiple Access
WIFI	Wireless Fidelity

Chapter 1

Introduction

The work of this thesis is intended for time division multiple access (TDMA) system applications but can also be extended to work in CDMA, WIFI, UMTS and WCDMA systems. The term resource optimisation mentioned in the title refers to the optimisation of the resources that make up a communication system. The system provider may attempt to save financially by providing cheaper services while maintaining good coverage. Examples of where the provider may incur large costs are in:

- antenna costs - antennas are costed according to type, ranging from very expensive smart antennas down to omni-directional antennas.
- location costs - the position in a building where the antenna needs to be mounted may be expensive or cheap.
- capacity requirements of the user - may be low in the case of voice links or high in the case of data links. The higher the bit rate required by the user equipment (UE) the better the planning of the system should be to give each user adequate service.
- environmental safety issues - planning the antennas in an area that will not effect nature or humans.

This thesis will concern itself with defining a resource optimisation algorithm that uses at its core a raytracing engine to provide propagation coverage information.

The optimisation problem will be defined as follows: Generate the least number of base stations at optimal locations giving adequate coverage to a set of users with a predetermined capacity requirement.

When a simulation is performed to obtain the optimal positions of base stations while providing the largest number of possible users wanting a connection to the system, this is usually performed in two stages known as downlink and uplink optimisation. In a telecommunications system the downlink is the connection from many servers in a network to many user equipments (UEs). User equipment (UE) is a general term given to laptops, palmtops, palmpilots, mobile phones, etc, that use wireless technologies. The uplink is the connection from the UE back to a receiving server. Servers are also called base transceiver stations (BTS) with the ability to both send and receive information. They can contain one or more antennas in a working system. For our system we will assume that the downlink optimisation requires a number of user equipments with a particular capacity requirement assigned to each, assumed already to be connected to the system.

The capacity requirements of the user will depend on what is known as the signal to interference ratio (SIR). This is a measure of the signal strength received by a user in the presence of possible interfering base stations. The other base stations which are possibly emitting at the one time can drown out the signal from the best server. This needs to be avoided where possible, and this is why an optimally positioned set of base stations is necessary. The uplink optimisation determines how many users can connect to the system assuming that each UE is possibly interfering with one another and that they are randomly distributed in the building.

The optimisation algorithm depends heavily on propagation effects which must be computed to give the signal to intererence ratios (SIR). Without accurate values for the signal strength it can not be assumed that the simulation of the system is reliable. The decision was made to use asymptotic methods to obtain the signal strength (path-loss) values.

Accurate field strength is virtually impossible to attain using a direct three dimensional integral equation formulation of the full wave solution over large surface

areas. The computational complexity is far too great due to the dense matrix systems arising during the calculation of the current density. Asymptotic methods however, have the advantage of being accurate at very high frequencies and are known to be computationally fast to calculate. They do have limitations though, some of which will be discussed at length in this thesis.

In the case of UMTS (specifically CDMA) we deal with frequencies of the order of 2GHz, that is a wavelength of 3/20 metres giving reasonable results for asymptotic methods. The electromagnetic wave is assumed to impinge upon surfaces at a point. This gives rise to reflection and transmission points on surfaces and diffraction points on edges. The asymptotic solutions most widely used are ray optic techniques calculating direct line of site (LOS), reflections and diffractions from a server to a UE. The ray-tracing method we consider uses the method of images to calculate reflected and transmitted rays. Two papers in the literature use very similar electromagnetic wave equations to the ones mentioned in this thesis. The first is a planning tool called CINDOOR[1] by Torres [81] containing a full three dimensional ray-tracing code for indoor wireless systems in enclosed spaces. The second is also an indoor wireless prediction tool described by Ji[39]. Other methods exist such as beamforming described by Funkhouser[25], allowing for faster computation of point to multipoint calculations. Authors such as Hassan-Ali[30] have used statistical models mixed with geometrical optics techniques to provide accurate coverage calculations. Multiple diffraction methods are sometimes incorporated such as the one described by Di Giampaolo[22].

The novelty in this thesis will be in the application of ray-tracing methods within optimisation algorithms. In the past authors such as Rappaport[71] used empirical propagation procedures in their optimisation software because it was fast to calculate. Many avoid using ray-tracing in a location optimisation because the ray-tracing needs to be recalculated each time the transmitter is moved. Many ray-tracing algorithms depend on a visibility algorithm assuming the transmitter is at a fixed location. It will be shown that this is not the case for the new ray-tracing algorithm described here. This means that the ray-tracing allows the optimisation procedures to operate

[1]All references are alphabethically ordered by surname of the first author not by order of appearance.

with reasonable computational times, while providing far more accurate propagation coverage in the building than empirical methods.

It turns out that a similar ray-tracing method to the one in this thesis was presented in 2002 by Yun[86] for a two dimensional outdoor environment problem. Our initial results where presented to Enterprise Ireland in a technical report in December 2001. The methods are sufficiently different to warrant a very detailed description in this thesis.

The optimisation algorithms described by Rappaport[71] are very involved but excellent as a basis on which to build a better algorithm. They require field strength information but do not contain signal to interference ratio information. In other words it does not consider the capacity problem. The algorithm of Rappaport will be used as a skeleton to build a far more sophisicated algorithm that accounts for SIR values. Many unexplained variables will be replaced with realistic parameters based on statistics made available by Nokia [52].

The chapters are broken down as follows:

Chapter 2: The main focus of this chapter will be to outline reflection and transmission coefficients as described in Balanis[7] for PEC, lossless and lossy media. The UTD diffraction coefficients are described based on the work of Kouyoumjian, Pathak[51] for single diffraction cases. The UTD result is only applicable to PEC materials, so the method of Tiberio [80] is applied to give a heuristic dielectric results. The corner diffraction corrections to UTD are described based on the work of McNamara[58] and Burnside[19]. It should be noted that Michaeli[62] have comments on the validity of the corner diffraction method in certain cases. Results are presented for reflection, transmission and diffraction coefficients at the end of this chapter. The results confirm the correct implementation of each method. Each of these methods are necessary to build the electromagnetic components of the ray-tracing code given the ray-paths as described later in Chapter 4.

Chapter 3: Here we will concern ourselves primarily with corrections to the reflection, transmission and diffraction coefficients commonly used in ray-tracing techniques.

A number of authors used the methods of Burnside[18] to account for multiple internal reflections inside walls. Most recently the thesis of DeCoster[21] and planning software CINDOOR [81] gave mention to the method of Burnside [18]. Although the method is fast to compute it is inherently limited due to its plane wave approximation to the antenna source. A more accurate way of describing the solution for multiple scattering is to use a full ray-tracing technique, but this is far too slow to compute and is hardly worth the effort. Described in this chapter is a numerical technique that computes the internal reflections in a dielectric slab, using a technique based on the method of images applied in most ray-tracing techniques. Because of certain geometrical properties of the slab it will be shown that the method is easy to apply and gives different path-loss values when compared with Burnside's results. A numerical technique is necessary for obtaining the ray-tracing result in a lossless and lossy dielectric slab, since the method of images can not be used to define the exact location of the image in the slab. The angle of transmission inside the slab must be computed numerically to give an accurate result. Here also a comparison between a ray-tracing solution using UTD and an approximate numerical moment method solution described by Brennan[17] will show up discrepancies in the UTD solution. Brennan presents a numerically fast but accurate approximation to Harrington's[29] exact solution. It was found when investigating the correctness of these UTD coefficients on a rectangular plate, that the scattered field does not totally agree with the solution obtained by Brennan[17]. A simple technique for correcting the problem areas is described in this chapter.

Chapter 4: In this chapter a different approach to looking at the building will be assumed to the ones commonly stated in the literature. Usually as in De Coster[21] the building is split into facets and some form of visibility algorithm is applied to determine the diffraction edges and the tree of reflections of the transmitter to provide a method of images solution when obtaining the reflection paths. In the optimisation algorithm described in Chapter 7, the location of a number of transmitters is altered at every step. It is very important therefore to define the ray-tracing algorithm in such a way that the visibility algorithm is fast but not dependant on transmitter

location. If the algorithm is dependant on transmitter location it will require a lot of preprocessing of information to obtain all ray-paths. But a technique that stores spatial information only is not dependant on location and can be partially stored away for reuse.

Instead of describing just the walls, floors, doors and windows of the building as facets, the thickness is added, and the space contained in the rooms is modelled also. In fact the building will be stored as convex spaces. A convex space has the property that any line segment passing through it will always enter and exit at only two points. This has the effect of providing a link from one point in space to any other point in space in the building. It has the advantage of speeding up the calculation of the reflected fields. Finding the diffraction edges is relatively easy also. This chapter gives a complete description of the building as it would appear in the computer code, and algorithms are presented for calculating the reflection points on filled convex spaces. A diffraction edge tree and edge tree are also explained in detail.

Chapter 5 This chapter is concerned with testing the complete ray-tracing software. A number of selected tests are used to ensure that the reflected, transmitted and diffracted ray-paths are generated correctly. Where problems were found, they were corrected. Results are presented for all techniques in a building consisting of three stories. A measurement campaign was conducted to test the validity of the ray-tracing in an indoor environment. Two measurement sets were compared with ray-tracing results and the differences between the two were explained.

Chapter 6: This chapter serves as an introduction to optimisation methods used in Chapter 7. Convex, quasi-convex and non-linear algorithms are discussed cast in the form of programming problems. Path-following methods are described that lead to optimal or sub-optimal solutions in a finite number of steps. An example is given to show how the whole process works in practise.

Chapter 7: The optimisation of a system depends on many issues. The nature of the function to be optimised is one issue and the type of constraints is another. In this chapter the function will contain variables relating to the location of the base stations and constraints will be of the form of capacity requirements at UE

positions. The function to be optimised subject to some constraints in this case is described by a non-linear programming problem. Much of the background on convex problems or linear programming problems is covered by Boyd [12] but some of the techniques can be applied to non-linear programmes. The method for solution of a programming problem is usually sought by a path-following method as described in Chapter 6. Both the downlink and the uplink algorithms are described and results are presented for test buildings given the parameters of Nokia [52] as test statistics to obtain physically meaningful results. A tighter constraint problem is obtained by expressing the path-loss values as a mean path-loss value. This mean value is obtained by a random phase generator that is usually computationally time consuming. Here a fast numerical technique is presented that speeds up the computation considerably.

Chapter 8: Conclusions are presented based on the results obtained in each of the previous chapters.

Appendices: A description of future work and a user manual for the STIWRO tool are explained in detail.

Chapter 2

Ray Tracing for Indoor Environment

2.1 Ray-based coordinate system

We define the Helmholtz equation derived from Maxwells equations [7] with complex permittivity ϵ as:

$$\nabla^2 \mathbf{E}(\mathbf{r}, \omega) + k^2 \mathbf{E}(\mathbf{r}, \omega) = 0 \tag{2.1}$$

where $k^2 = \omega^2 \mu \epsilon$ and $\mathbf{E}$ is the time-harmonic electric field at the point $\mathbf{r}$, ω is the angular frequency, ϵ is the permittivity of free space and μ is the permeability of free space.

Adopting the Luneberg[56], Kline[47], guess solution of the isotropic source in a free space medium, we assume the asymptotic solution:

$$\mathbf{E}(\mathbf{r}, \omega) \approx e^{-jk\psi(\mathbf{r})} \sum_{i=0}^{\infty} \frac{\mathbf{E}_i(\mathbf{r})}{(j\omega)^i} \tag{2.2}$$

$$\mathbf{H}(\mathbf{r}, \omega) \approx e^{-jk\psi(\mathbf{r})} \sum_{n=0}^{\infty} \frac{\mathbf{H}_i(\mathbf{r})}{(j\omega)^i} \tag{2.3}$$

where $\psi(\mathbf{r})$ is the wave function referred to as the eikonal surface.

Equating like powers in ω leads to a further set of equations.

1. The eikonal function

$$\nabla \psi = \hat{\mathbf{r}} n \tag{2.4}$$

where n is the refractive index of the medium.

2. The transport equations

$$\begin{array}{rl} \frac{\partial \mathbf{E}_0}{\partial \mathbf{r}} + \frac{1}{2}\left\{\frac{\nabla^2\psi}{n}\right\}\mathbf{E}_0 = 0 & \text{for the first-order terms} \\ \frac{\partial \mathbf{E}_m}{\partial \mathbf{r}} + \frac{1}{2}\left\{\frac{\nabla^2\psi}{n}\right\}\mathbf{E}_m = \frac{v_p}{2}\nabla^2\mathbf{E}_{m-1} & \text{for the higher-order terms} \end{array} \tag{2.5}$$

where v_p is the wave velocity in the medium. This equation is used later to define the slope diffraction term in James[37], Balanis[7] Ch. 13.

3. The condition equations

$$\begin{array}{rl} \hat{s}\cdot\mathbf{E}_0 = 0 & \text{for the first-order terms} \\ \hat{s}\cdot\mathbf{E}_m = v_p\nabla\cdot\mathbf{E}_{m-1} & \text{for the first-order terms} \end{array} \tag{2.6}$$

As the radial frequency w tends to infinity in the asymptotic expansions, equation (2.2) and (2.3) yield:

$$\mathbf{E}(\mathbf{r},\omega) \approx e^{-jk\psi(\mathbf{r})}\mathbf{E}_0(\mathbf{r}) \tag{2.7}$$

$$\mathbf{H}(\mathbf{r},\omega) \approx e^{-jk\psi(\mathbf{r})}\mathbf{H}_0(\mathbf{r}) \tag{2.8}$$

Using these expressions forms a ray-optic solution to the Helmholtz equation formula. We must consider the cases of direct, reflected, transmitted and diffracted rays.

To define the formula for the direct ray all that remains to be defined is the amplitude factor A_s which gives the attenuation between any two points along a ray-path. Because the conservation of energy flux in a tube of rays must be preserved, for an isotropically emanating source point, we can conclude that

$$S_0 dA_0 = SdA \tag{2.9}$$

where S_0 is the radiation density at $r = 0$ and S is the radiation density at r, with cross-sectional areas given by dA_0 and dA respectively (see Figure 2-1). We also know that

$$\frac{|\mathbf{E}|}{|\mathbf{E}_0|} = \frac{dA_0}{dA} = \sqrt{\frac{\rho_1\rho_2}{(\rho_1+s)(\rho_2+s)}} \tag{2.10}$$

which defines the spatial attenuation factor $A_s(s)$.

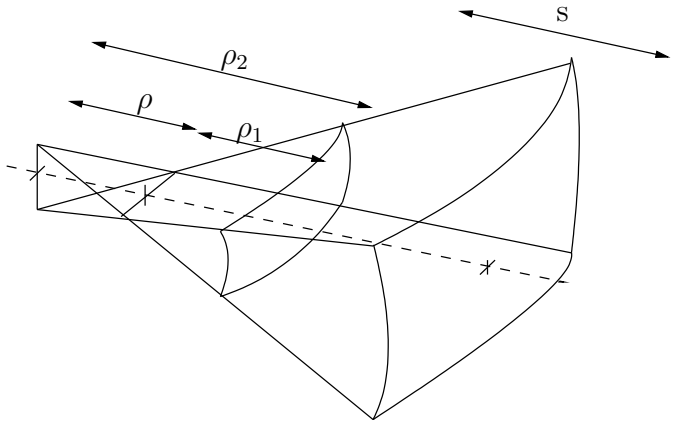

Figure 2-1: A astigmatic ray generated by two narrow beams.

For different sources the astigmatic attenuation factor changes over distance when the wave is propagating through free space. For instance, in the case of a line-source which is isotropic and transverse magnetic in z (TM_z) with a field observed at position ρ relative to the source, we know that the source extends to infinity in the z-direction giving the first radius of curvature, $\rho_1 = +\infty$ and the second radius of curvature is $\rho_2 = \rho$, the distance of the observer from the source. In the case of a spherical wave the radii of curvature are equal, ($\rho_1 = \rho_2 = \rho$).

The following results for the astigmatic attenuation factor $A_s(s)$ hold:

type	ρ_1	ρ_2	$A_s(s)$
plane wave	∞	∞	$\frac{1}{s}$
line source	∞	ρ	$\sqrt{\frac{\rho}{\rho+s}}$
point source	ρ	ρ	$\frac{\rho}{\rho+s}$

(2.11)

2.2 Reflection from Planar Surfaces

If the reflecting surface can be approximated by a plane tangent at P and the wave front of the incident field is assumed to be planar, then the reflected field as given by Balanis[7], Ch.13, is defined to be

$$\mathbf{E}^r(s) \;=\; \mathbf{E}^i(\mathbf{P}) \cdot \overline{R} \sqrt{\frac{\rho_1^r \rho_2^r}{(\rho_1^r + s)(\rho_2^r + s)}} e^{-jks} \tag{2.12}$$

where ρ_1^r, ρ_2^r are the principle radii of curvature of the reflected wave front at the

point of reflection **P**. $\overline{R}$ is the reflection coefficient matrix and $\mathbf{E}_i$ is the incident field at the point of reflection **P** (see figure 2-2).

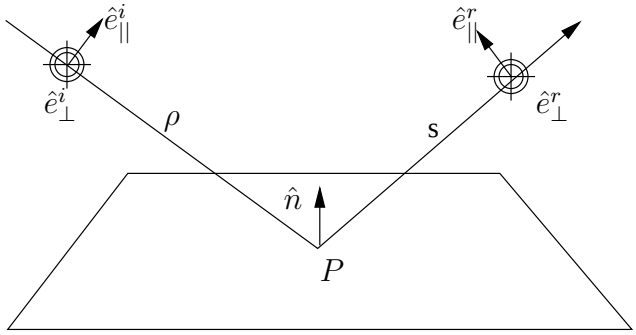

Figure 2-2: The reflected ray from a flat plate.

The electric field is split into the parallel and perpendicular components with respect to the direction of the ray. The incident directions $\hat{e}^i_{\perp}$ and $\hat{e}^i_{||}$ are defined as

$$\hat{e}^i_{\perp} = \frac{\hat{s}_i \times \hat{n}}{|\hat{s}_i \times \hat{n}|} \tag{2.13}$$

$$\hat{e}^i_{||} = \hat{s}_i \times \hat{e}^i_{\perp} \tag{2.14}$$

and the outgoing reflected ray has directions:

$$\hat{e}^r_{\perp} = \hat{e}^i_{\perp} \tag{2.15}$$

$$\hat{e}^r_{||} = \hat{s}_r \times \hat{e}^r_{\perp} \tag{2.16}$$

These components are refered to as the components of the ray-based coordinate system. Using them we can define the incident field as:

$$\mathbf{E}^i(R) = (\mathbf{E}^i(R) \cdot \hat{e}^i_{||})\hat{e}^i_{||} + (\mathbf{E}^i(R) \cdot \hat{e}^i_{\perp})\hat{e}^i_{\perp} \tag{2.17}$$

In turn the matrix $\overline{R}$ is defined in terms of the ray-based coordinate system as:

$$\overline{R} = \begin{bmatrix} R_{\perp} & 0 \\ 0 & R_{||} \end{bmatrix} \tag{2.18}$$

where

$$R_{\perp} = = \frac{\eta_2 \cos\theta_i - \eta_1 \cos\theta_t}{\eta_2 \cos\theta_i + \eta_1 \cos\theta_t} \tag{2.19}$$

$$R_{||} = = \frac{-\eta_1 \cos\theta_i + \eta_2 \cos\theta_t}{\eta_1 \cos\theta_i + \eta_2 \cos\theta_t} \tag{2.20}$$

where $\eta_i = \sqrt{\frac{\mu_i}{\epsilon_i}}$, μ_i is the permeability of medium i, and ϵ_i is the real or complex permittivity of medium i (see Balanis[7], Ch. 5). Snell's law of refraction holds giving

$$k_1 \sin\theta_i \;=\; k_2 \sin\theta_t \tag{2.21}$$

giving $\cos\theta_t = \sqrt{1-(k_1/k_2)^2\sin^2\theta_i}$, where $k_i = \omega\sqrt{\mu_i\epsilon_i}$ is the wave number in medium i, θ_i is the angle of incidence made with the outward normal to the surface of contact and the incident ray, and θ_t is the angle after refraction inside medium 2 (see Figure 2-3).

2.3 Reflection and Transmission Coefficients

With all the information above it is now possible to define the reflection coefficient and transmission coefficient through a dielectric medium assuming that we are travelling from free space initially. Assuming that free space is medium 1 and the dielectric slab is medium 2 as in Figure 2-3 we must define the reflection and transmission coefficient for perfect electric conductors (PEC), lossless and lossy media.

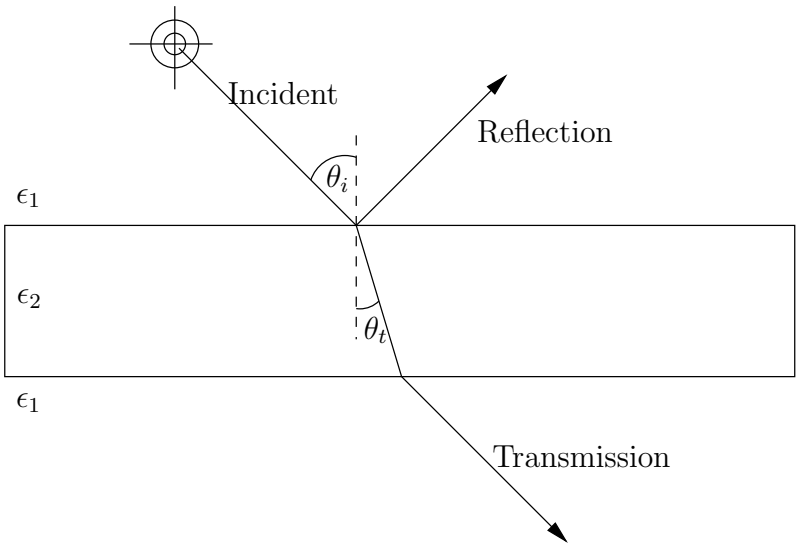

Figure 2-3: The reflected and transmitted ray in a dielectric slab.

2.3.1 Perfect Electric Conductor (PEC) Case

In this case $\epsilon_2 = -j\infty$ so that the reflection coefficient for medium 1 to medium 2 given by $\overline{R}$ is defined as

$$\overline{R} = \begin{bmatrix} R_\perp & 0 \\ 0 & R_{||} \end{bmatrix} = \begin{bmatrix} -1 & 0 \\ 0 & 1 \end{bmatrix} \tag{2.22}$$

In this case there is no transmission into the planar surfaces.

2.3.2 Lossless and Lossy Case

In this case $\epsilon_2 = \epsilon_1\epsilon'$ where ϵ_1 is the permittivity of free space and ϵ' is the relative permittivity of the dielectric slab. Knowing $\mu_2 = \mu_1$ and $k_1/k_2 = 1/\epsilon'$ leads to the expression of the reflection coefficients in equations (2.19) and (2.20) as

$$R_\perp = \frac{\cos\theta_i - \sqrt{\epsilon' - \sin^2\theta_i}}{\cos\theta_i + \sqrt{\epsilon' - \sin^2\theta_i}} \tag{2.23}$$

$$R_{||} = \frac{-\epsilon'\cos\theta_i + \sqrt{\epsilon' - \sin^2\theta_i}}{\epsilon'\cos\theta_i + \sqrt{\epsilon' - \sin^2\theta_i}} \tag{2.24}$$

The corresponding transmission coefficients in the perpendicular and parallel directions from free space into the dielectric medium are given by

$$T_\perp^{12} = \frac{2\cos\theta_i}{\cos\theta_i + \sqrt{\epsilon' - \sin^2\theta_i}} \tag{2.25}$$

$$T_{||}^{12} = \frac{2\sqrt{\epsilon'}\cos\theta_i}{\epsilon'\cos\theta_i + \sqrt{\epsilon' - \sin^2\theta_i}} \tag{2.26}$$

and the transmission coefficients out of the dielectric medium are given by

$$T_\perp^{23} = \frac{2\sqrt{\epsilon' - \sin^2\theta_i}}{\cos\theta_i + \sqrt{\epsilon' - \sin^2\theta_i}} \tag{2.27}$$

$$T_{||}^{23} = \frac{2\sqrt{\epsilon'}\sqrt{\epsilon' - \sin^2\theta_i}}{\epsilon'\cos\theta_i + \sqrt{\epsilon' - \sin^2\theta_i}} \tag{2.28}$$

In the case of the lossy medium the relative permittivity is defined to be

$$\epsilon' = \epsilon_r - j\sigma/\omega \tag{2.29}$$

where $k_i = \alpha_i + j\beta_i$ and

$$\alpha_i = \omega\sqrt{\mu_i\epsilon_i}\left\{\frac{1}{2}\left[\sqrt{1+\left(\frac{\sigma_i}{\omega\epsilon_i}\right)^2}-1\right]\right\} \tag{2.30}$$

$$\beta_i = \omega\sqrt{\mu_i\epsilon_i}\left\{\frac{1}{2}\left[\sqrt{1+\left(\frac{\sigma_i}{\omega\epsilon_i}\right)^2}+1\right]\right\} \tag{2.31}$$

as defined by Balanis[7], Ch. 5.

2.4 Transmission Through a Dielectric Slab

When a planewave propagates into a dielectric slab it bends on contact meaning that the time spent inside the slab is longer than if it could pass through at the angle of incidence (see Figure 2-4). The phase also changes inside the slab. For this reason it is important to correct the transmitted field through the slab. If the phase of the field entering the slab is $e^{-jk_1 s}$ then the phase and attenuation must be altered so that the field takes the form:

$$e^{-jk_1 s} \rightarrow \overline{T}_{12}\overline{T}_{23}e^{-jk_1 s}e^{-jk_1\rho_1}e^{-jk_2 l}e^{+jk_1\rho_2} \tag{2.32}$$

as defined in Burnside[18], where l is the length of the ray inside the slab, ρ_1 is the extra distance covered by the incident ray before it bends, ρ_2 is the distance covered by the ray inside the slab if it were to travel straight through without refraction, and $t = \rho_2 - \rho_1$. See Figure 2-4 to clarify the meaning of variables.

The term $e^{-jk_2 l}$ is the actual phase due to the transmission in the slab. The term $e^{-jk_1 t} = e^{-jk_1(\rho_2-\rho_1)}$ is what would be calculated by the ray-tracing, because the bending in the slab is not accounted for. Together they give the necessary correction to the field.

If d is the width of the slab then the value of t and l are given by the following formulae:

$$t = l\cos(\theta_i - \theta_t) \tag{2.33}$$

$$= \frac{d\cos\theta_i\sqrt{\epsilon' - \sin^2\theta_i} + d\sin^2\theta_i}{\sqrt{\epsilon - \sin^2\theta_i}} \tag{2.34}$$

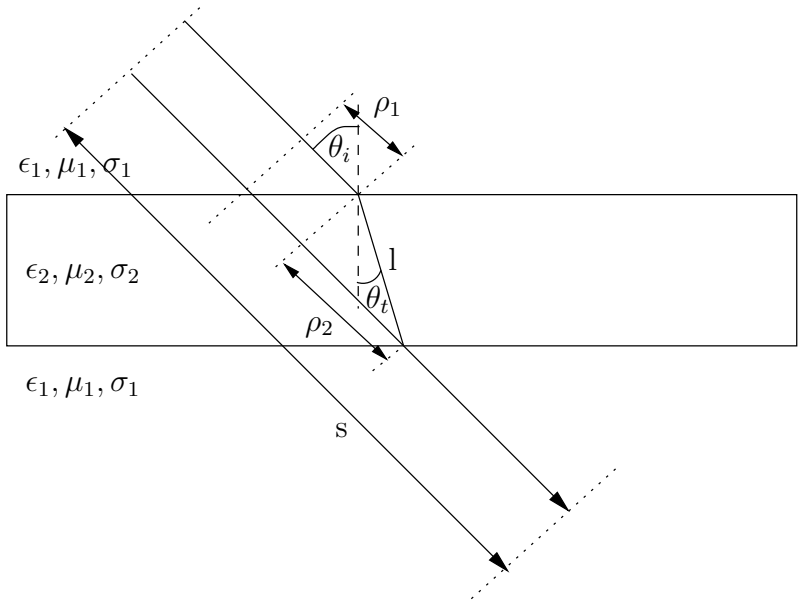

Figure 2-4: The planewave transmission through a slab.

$$l = \frac{d}{\cos\theta_t} = \frac{d\sqrt{\epsilon'}}{\sqrt{\epsilon' - \sin^2\theta_i}} \tag{2.35}$$

2.5 Three Dimensional Diffraction Coefficients

The use of the localised coordinate system is not only used for the reflection and transmission coefficients but also for the diffraction coefficients. Instead of a ray-based coordinate system as in the case of reflections and transmissions, an edge-based coordinate system is created for an incoming ray striking a wedge at a diffraction point and scattering from that point in many directions which lie on the Keller cone. For an angle β_0 made with the edge e and the source point, the angle made with e and some observation point must also be β_0 (see Figure 2-5).

The standard two dimensional diffraction coefficient is extended to three dimensions so that the dyadic coefficient is defined by McNamara[58] as:

$$\mathbf{E}^d = \mathbf{E}^i(\mathbf{P})\overline{D}\sqrt{\frac{\rho}{s(\rho+s)}}e^{-jk_1 s} \tag{2.36}$$

where $\mathbf{E}^i(\mathbf{P})$ is the incident field at the point $\mathbf{P}$ from a source point, $\overline{D}$ is the diffraction matrix defined by Pathak, Kouyoumjian[51]. The square root term is

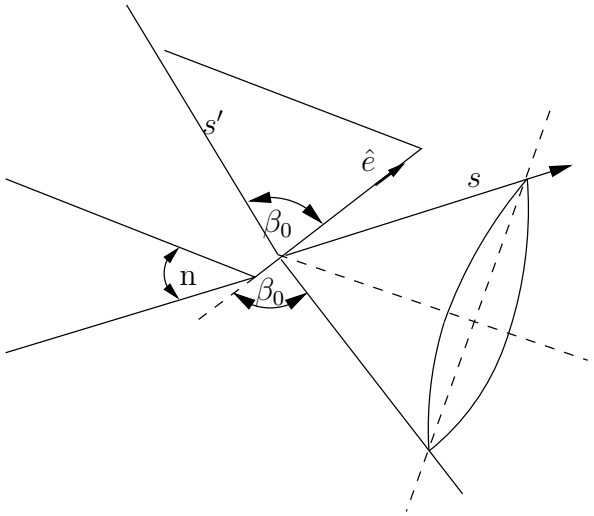

Figure 2-5: The diffraction wedge and Keller cone.

the attenuation factor due to diffraction from a point source, and the phase term is related to the distance travelled from the diffraction point to the receiver point.

The diffraction coefficient of Pathak, Kouyoumjian for a PEC is given by:

$$\overline{D} = \begin{bmatrix} -D_s & 0 \\ 0 & -D_h \end{bmatrix} \tag{2.37}$$

where

$$D_s = C\left[D_e^+(\xi^-) + D_e^-(\xi^-) + R_0^\perp D_e^-(\xi^+) + R_1^\perp D_e^+(\xi^+)\right] \tag{2.38}$$

$$D_h = C\left[D_e^+(\xi^-) + D_e^-(\xi^-) + R_0^{||} D_e^-(\xi^+) + R_1^{||} D_e^+(\xi^+)\right] \tag{2.39}$$

where

$$\xi^\mp = \phi \mp \phi' \tag{2.40}$$

$$D_e^\mp(\xi^\pm) = \cot\left(\frac{\pi \mp \xi^\pm}{2n}\right)\mathcal{F}(kLa^\mp(\xi^\pm)) \tag{2.41}$$

$$\mathcal{F}(x) = 2j\sqrt{x}e^{jx}\int_{\sqrt{x}}^{\infty} e^{-j\tau^2}d\tau \tag{2.42}$$

$$a^\mp(\xi^\pm) = 2\cos^2\left(\frac{2n\pi N^\pm - \xi^\pm}{2}\right) \tag{2.43}$$

$$2n\pi N^\pm - \xi^\pm \approx \pm\pi \tag{2.44}$$

$$L = \frac{ss'}{s+s'}\sin^2\beta_0 \tag{2.45}$$

where $N^\pm$ is the nearest integer satisfying equation (2.44).

Setting up the ray-based coordinate system $\hat{s}', \phi', \beta_0'$ for the incoming ray and $\hat{s}, \phi, \beta_0$ for the outgoing ray, it is possible to write the coordinates as:

$$\hat{\phi}' = \frac{-\hat{e} \times \hat{s}'}{\mid \hat{e} \times \hat{s}' \mid}, \hat{\beta}_0' = \hat{\phi}' \times \hat{s}' \tag{2.46}$$

$$\hat{\phi} = \frac{\hat{e} \times \hat{s}}{\mid \hat{e} \times \hat{s} \mid}, \hat{\beta}_0 = \hat{\phi} \times \hat{s} \tag{2.47}$$

where $\hat{n}_i$ is the unit outward normal to the i^{th} planar surface B_i of the wedge.

The construction of the angle ϕ' is achieved by the following steps:

- construct the unit vector $\hat{t}_0$ pointing along the 0^{th} planar surface which is perpendicular to the unit vector $\hat{e}$.

$$\hat{t}_0 = \hat{n}_0 \times \hat{e} \tag{2.48}$$

- construct the unit vector $\hat{s}_t'$ obtained by projecting the vector $\hat{s}'$ onto a plane containing $\hat{t}_0$.

$$\hat{s}_t' = \frac{s_t'}{\mid s_t' \mid} = \frac{s' - (s'.\hat{e})\hat{e}}{\mid s' - (s'.\hat{e})\hat{e} \mid} \tag{2.49}$$

  It should be noted that there is a type setting error in McNamara's[58] otherwise excellent book when defining both s_t' and s_t, although the final formula is correct.

- ϕ' is the angle between the unit vectors t_0 and s_t'. The angle ϕ is constructed in a similar manner.

$$\phi' = \pi - \left[\pi - \cos^{-1}(-\hat{s}_t) \cdot \hat{t}_0'\right] \mathrm{sgn}(-\hat{s}_t' \cdot \hat{n}_0) \tag{2.50}$$

$$\phi = \pi - \left[\pi - \cos^{-1}(-\hat{s}_t \cdot \hat{t}_0)\right] \mathrm{sgn}(-\hat{s}_t' \cdot \hat{n}_0) \tag{2.51}$$

where sgn is the sign function defined as

$$\mathrm{sgn(x)} = \begin{cases} 1 & \text{if } x \geq 0 \\ -1 & \text{if } x < 0 \end{cases} \tag{2.52}$$

The reflection coefficients $R_{\perp,||}^{0,1}$ from the planar surfaces numbered according to their relevant planes, are defined as in equations (2.23) and (2.24) to be:

$$R_{\perp}^{0,1} = \frac{\cos\theta_i^{0,1} - \sqrt{\epsilon' - \sin^2\theta_i^{0,1}}}{\cos\theta_i^{0,1} + \sqrt{\epsilon' - \sin^2\theta_i^{0,1}}} \tag{2.53}$$

$$R_{||}^{0,1} = \frac{-\epsilon'\cos\theta_i^{0,1} + \sqrt{\epsilon' - \sin^2\theta_i^{0,1}}}{\epsilon'\cos\theta_i^{0,1} + \sqrt{\epsilon' - \sin^2\theta_i^{0,1}}} \tag{2.54}$$

where

$$\cos\theta_i^0 = -\hat{s}_t' \cdot \hat{n}_0 \tag{2.55}$$

$$\cos\theta_i^1 = +\hat{s}_t' \cdot \hat{n}_1 \tag{2.56}$$

2.6 Corner Diffraction

The uniform theory of diffraction uses the concept of a wedge that extends infinitely along the edge. In practice this is not the case, and therefore a correction may be required to supplement the solution. Using corner diffraction provides a correction for this, and a correction for the case were there is a virtual diffraction point, that is a point which would lie on the diffraction edge if it were not a finite length.

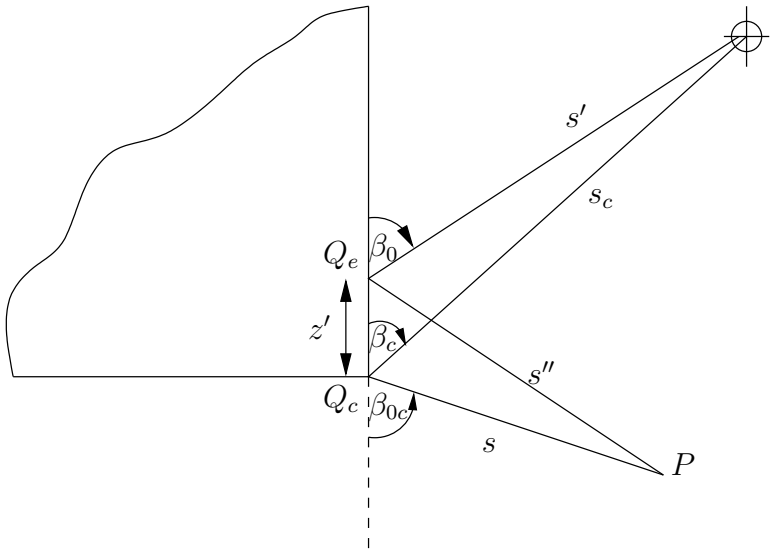

Figure 2-6: The geometry associated with a corner diffraction calculation.

The generalised corner diffraction formula described by both McNamara[58] and Burnside[19] for corners that do not meet at 90^0 degrees to one another is given by

$$\begin{bmatrix} \mathbf{E}_{\beta_0^c} \\ \mathbf{E}_{\phi}^c \end{bmatrix} = \begin{bmatrix} I \\ M \end{bmatrix} \frac{\sqrt{\sin\beta_c \sin\beta_{0c}}}{\cos\beta_{0c} - \cos\beta_c} \mathcal{F}[k_1 L_c a(\pi + \beta_0 c - \beta_c)] \frac{e^{-jk_1 s}}{4\pi s} \tag{2.57}$$

$$\begin{bmatrix} I \\ M \end{bmatrix} = \begin{bmatrix} \mathbf{E}_{\beta_0'}^i(Q_c) C_s(Q_e) \\ \mathbf{E}_{\phi_i}^i(Q_c) C_h(Q_e) \end{bmatrix} \sqrt{\frac{8\pi}{k_1}} e^{j\pi/4} \tag{2.58}$$

where the corner diffraction coefficients for both the electric and magnetic case are given by:

$$\begin{aligned} C_{s,h} = & \frac{-e^{j\pi/4}}{2n\sqrt{2\pi k_1}\sin\beta_0} \Bigg[\\ & \cot\left(\frac{\pi + \xi^-}{2n}\right) \mathcal{F}[k_1 L^i a(\xi^-)] \left| \mathcal{F}\left\{ \frac{L^i a(\xi^-)}{2\pi L_c a(\pi + \beta_{0c} - \beta_c} \right\} \right| \\ + & \cot\left(\frac{\pi - \xi^-}{2n}\right) \mathcal{F}[k_1 L^i a(\xi^-)] \left| \mathcal{F}\left\{ \frac{L^i a(\xi^-)}{2\pi L_c a(\pi + \beta_{0c} - \beta_c} \right\} \right| \\ \mp & \cot\left(\frac{\pi - \xi^+}{2n}\right) \mathcal{F}[k_1 L^{rn} a(\xi^+)] \left| \mathcal{F}\left\{ \frac{L^{rn} a(\xi^+)}{2\pi L_c a(\pi + \beta_{0c} - \beta_c} \right\} \right| \\ \mp & \cot\left(\frac{\pi - \xi^+}{2n}\right) \mathcal{F}[k_1 L^{ro} a(\xi^+)] \left| \mathcal{F}\left\{ \frac{L^{ro} a(\xi^+)}{2\pi L_c a(\pi + \beta_{0c} - \beta_c} \right\} \right| \Bigg] \end{aligned} \tag{2.59}$$

where $\mathcal{F}$ is the fresnel transition function (FTF), $a(x) = 2cos^2(x/2)$ and the attenuation due to the diffraction edge is given by

$$L = \frac{s's''}{s' + s''} \sin^2\beta_0 \tag{2.60}$$

The attenuation due to scattering from the corner when the edge is straight is given by

$$L_c = \frac{s_c s}{s_c + s} \tag{2.61}$$

2.7 Results

To confirm that the reflection, transmission and diffraction coefficients are correct, it is now necessary to compare the results from a C++ software implementation of the formulations against previously presented results.

2.7.1 Reflection and Transmission Coefficients

The perpendicular reflection and transmission coefficients defined in equations (2.23) and equation (2.25) are shown in Figure 2-7 to agree with the results of Balanis[7]. The parallel reflection and transmission coefficients defined in equations (2.24) and equation (2.26) are shown in Figure 2-8. All results are presented for lossless relative permittivity $\epsilon_r = 2.56, 9, 16, 25, 81$.

2.7.2 Uniform Theory of Diffraction Coefficients

The result for a two dimensional half-plane is now presented. The parameters are $\theta' = 30^0$, $\theta \in [0, 360^0]$, $n = 2\pi$, $\beta_0 = 90^0$, $L = \rho = 100\lambda$, $\lambda = 1$. The diffraction coefficient consisting of four terms can be broken up into two terms relating to the incident shadow boundary and another two relating to the reflective shadow boundary. The first term is unchanged whether considering electric or magnetic polarisation, while the second reflective term is positive for magnetic polarisation and negative for electric polarisation. The results obtained in Figure 2-9 agree with the results presented by Balanis[7].

2.7.3 Corner Diffraction Coefficients

The corner diffraction results are usually presented in the literature for far field scattering results or as radar cross sections (RCS). Changing some of the terms in the corner diffraction formula it should be possible to define the solution for the scattering from a $2d \times 2d$ rectangular plate excited by a monopole resting on its centre as shown in Figure 2-10.

The angle β_0' has the property that

$$\beta_0' = \cos^{-1}(\hat{e}_A \cdot \hat{s}) = \cos^{-1}(-\sin\theta\cos\Phi) \tag{2.62}$$

where $\Phi = 45^o$ is the outgoing planewave angle to obtain the far field scattering result. From this it is possible to obtain the diffraction point locations for Q_A, Q_B, Q_C and Q_D on each edge of the rectangular plate. The incident field at the corner diffraction

points is defined to be

$$\mathbf{E}^i_{\phi'} = -\frac{e^{-jk\sqrt{2}d}}{\sqrt{2}d} \tag{2.63}$$

In the example chosen it turns out that $\mathbf{E}^i_{\beta'_0} = 0$. The astigmatic attenuation factor is defined to be $A_s = 1/\sqrt{\rho'}$ for a planewave scattering from a point. The factors L and L_c must also change because of the planewave scattering to give:

$$L = \rho \sin^2 \beta_0 \tag{2.64}$$

$$L_c = \sqrt{2} \tag{2.65}$$

Also the phase factor is defined as $e^{-jk\hat{s}_r \cdot r_2}$ instead of e^{-jks}, where $r_2 = \sqrt{2}d\hat{x} + \sqrt{2}d\hat{y}$ in the case of edge A.

The scattered field $\mathbf{E}^c_\theta = \mathbf{E}^c_\phi(\hat{\phi} \cdot \hat{\theta})$ is presented in Figure 2-11. The results are identical to that presented in McNamara [58]. The length $d = 2.5\lambda$ for this particular example.

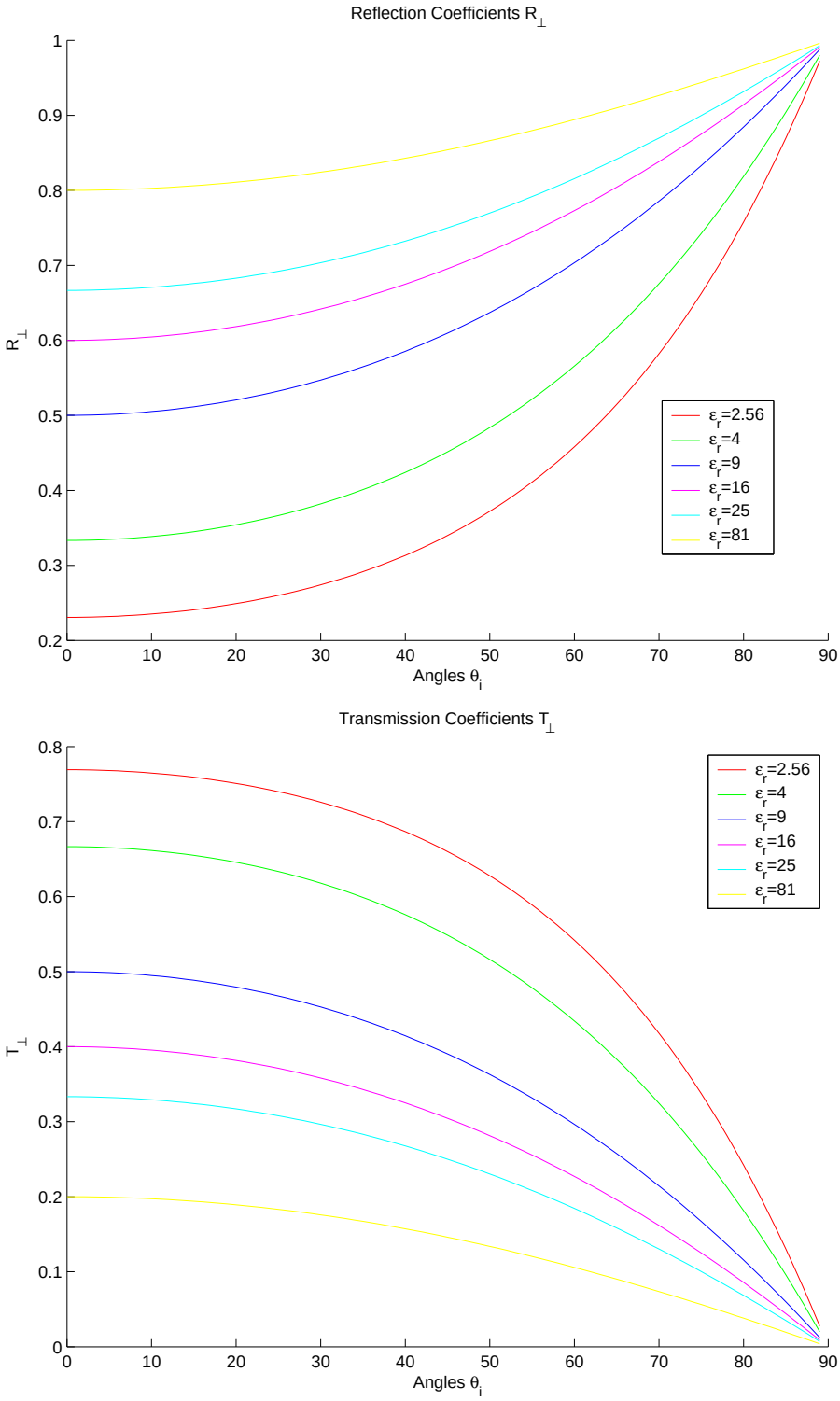

Figure 2-7: The perpendicular reflection and transmission coefficient plots for varying lossless relative permittivity ϵ_r.

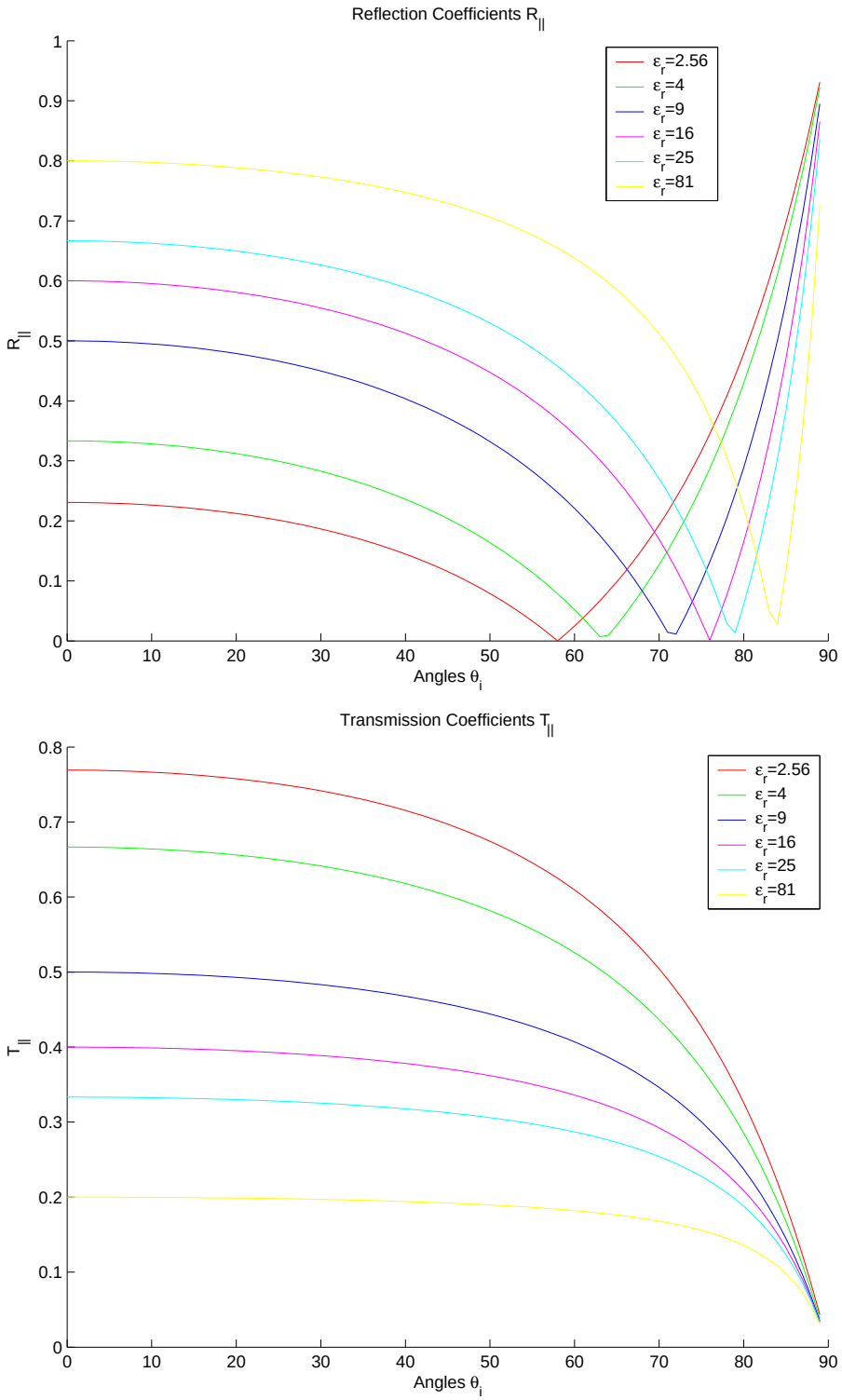

Figure 2-8: The parallel reflection and transmission coefficient plots for varying lossless relative permittivity ϵ_r.

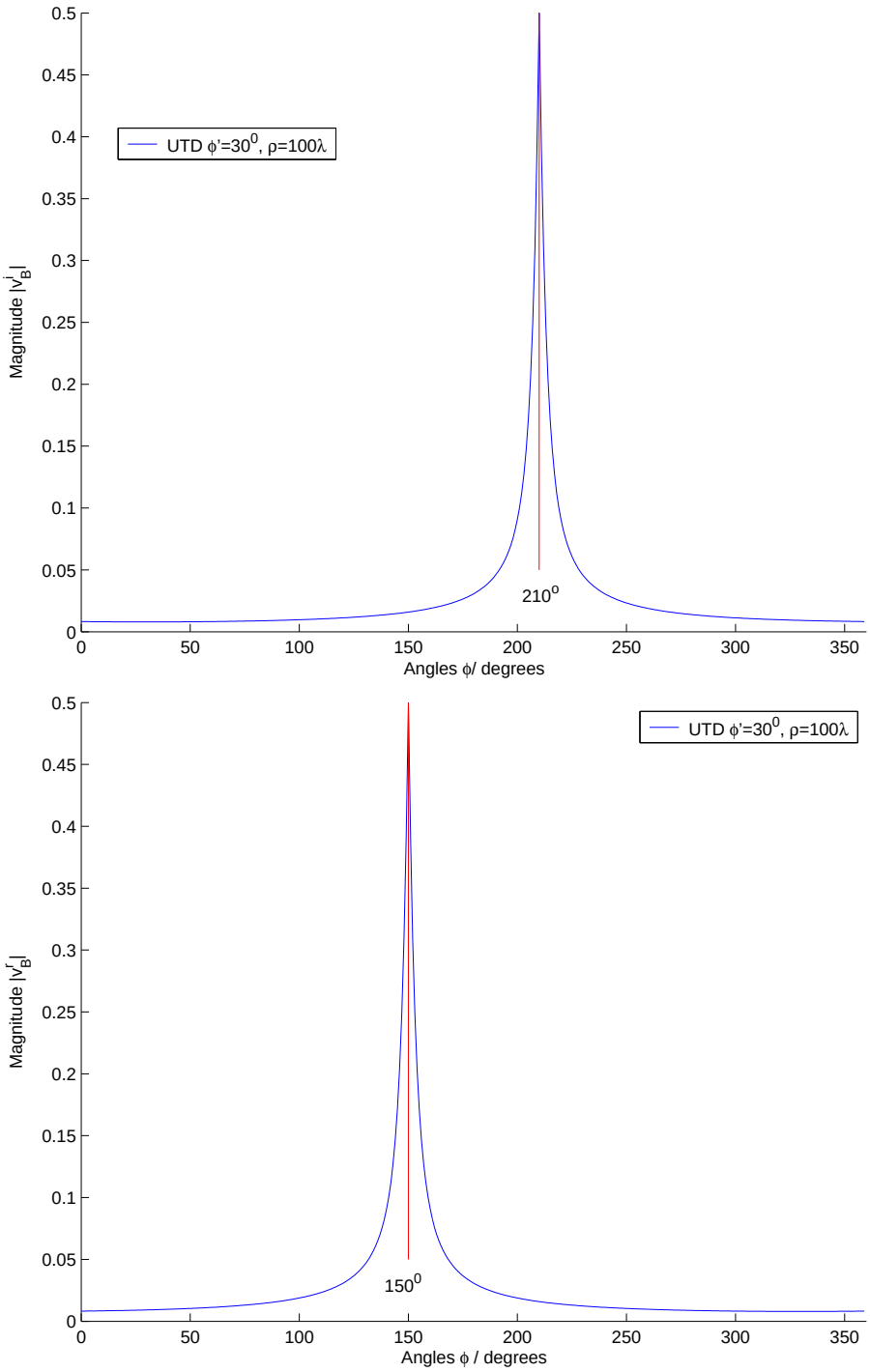

Figure 2-9: The diffraction coefficient terms for the incident and reflective shadow boundaries V_B^i and V_B^r.

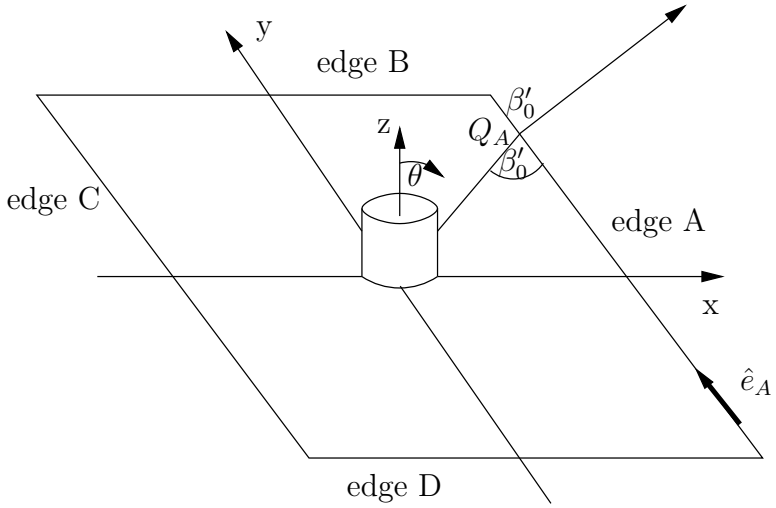

Figure 2-10: A monopole mounted over a rectangular plate.

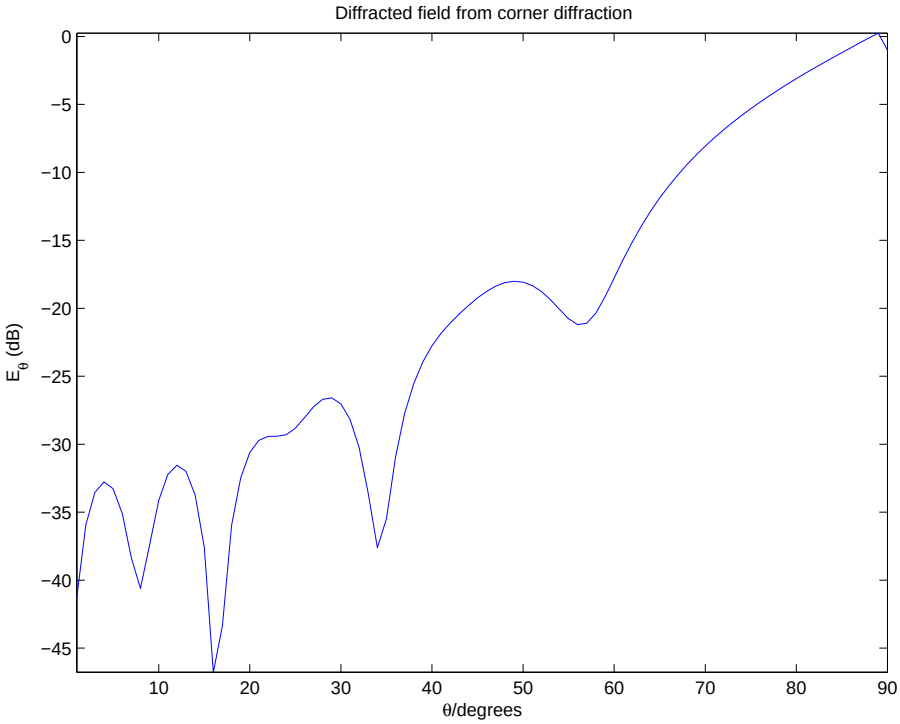

Figure 2-11: The scattered field $\mathbf{E}_\theta^c$ for a rectangular plate with $d = 2.5\lambda$, incorporating corner diffractions.

Chapter 3

Extensions to Ray-tracing

In this chapter amendments are made to known reflection, transmission and diffraction coefficients described in the literature. Many different types of methods can be applied to the three dimensional ray-tracing problem but it was felt that a closer examination at the dielectric slab problem would be advantageous. Before elaborating on the details of these methods a quick overview of existing methods is described here for completeness.

3.1 Overview of Existing Methods

Reflection coefficients and transmission coefficients are well explained by Balanis[7] and Born, Wolf[11]. Burnside[18] introduced an approximation that could be used to calculate internal reflections in dielectric slabs. A multi-layered dielectric structure as described by Thakur[79] could be considered, but will not be included in this work. The main concern mentioned in many papers is the treatment of the diffraction coefficient. The definitive works on the uniform theory of diffraction are presented by Kouyoumjian and Pathak[49], [51], [66]. An excellent overview of diffraction based methods is presented by Knott[48] in which the physical theory of diffraction (PTD) by Ufimtsev [82], the method of equivalent edge currents (EEC) of Michaeli [59]-[61], and physical optics are presented. The equivalent edge currents has since been combined with PTD to give the PTDEEC methods described by Jakobus[34], [35],

which incited remarks by Ufimtsev[83] due to inaccuracies in the definition of PTD.

An exact numerical formulation of the full wave solution using an integral equation approach was obtained by Harrington[29]. Later Rao, Wilton, Glisson[69] designed a basis function that allows the integral equation to be solved more easily. This method employs what is now known as the RWG basis set used in a moment method solution for small arbitrary shaped surfaces. The current density must be calculated at a very large number of points on the surface to obtain an accurate numerical solution, and because of this, the number of unknowns in the problem is very large. The storage of a full moment method impedance matrix is impossible for large plates because the matrix is dense. By dense, we mean that most of the entries in the matrix are non-zero. More recently the method by Brennan[17] was applied to rectangular plates using a forward-backward moment method solution that attempts to avoid the calculation of the complete impedance matrix. Again this method uses the RWG basis. The method stores the contribution to the current density from the impedance matrix in groups, and each group is updated in a new iteration throwing away the used impedance matrix contribution, thus allowing for larger plate sizes and faster computational times. Other solutions such as the finite difference time domain problems (FDTD) as described more recently by Yin[85] can also be used for three dimensional solutions of the Helmholtz equation.

3.2 Improvement of Reflection and Transmission Coefficients

Ray-optics methods including transmission coefficient calculations in lossless dielectric walls are well explained by Burnside [18].

The result of Burnside is obtained from an infinite geometric series of planewave reflection terms inside a dielectric slab. Each term is of the form

$$\overline{R}_m = T_1 T_2 R_1^{2m-1} P_d^{2m} P_a^m \tag{3.1}$$

where $\overline{R}_m$ is the m^{th} order internal reflection coefficient in the slab, $l = d/\cos\theta_t$ is the length of the ray reaching from one side of the slab to the other, $P_d = e^{-jk_2 l}$ is the

change in phase for the length of the ray, and $P_a = e^{jk2l\sin\theta_t \sin\theta_i}$ is a phase shift term due to the emergence of the ray from a different point in the slab. θ_i, θ_t and d are indicated on Figure 3-1. R_1 is the reflection coefficient from the free space medium into the dielectric slab as described in Section 2.3. T_1 and T_2 are the transmission coefficients into and out of the slab as described in Section 2.3 also.

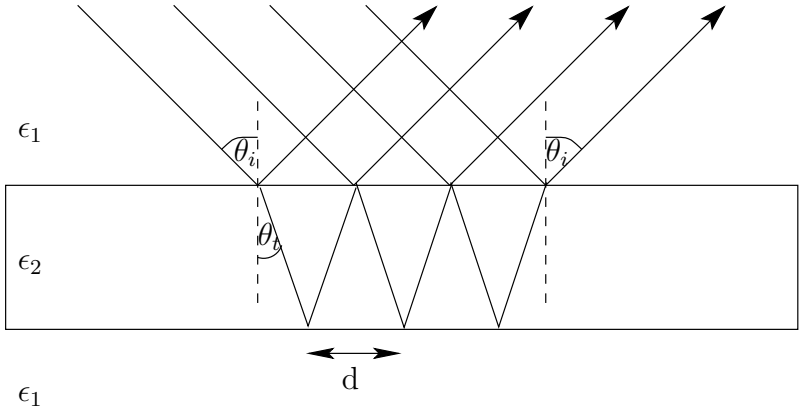

Figure 3-1: Infinite number of planewave reflections inside a lossless dielectric slab.

When the infinite series is summed in the case of the perpendicular and parallel components the following result was obtained:

$$R_{||,\perp} = \frac{R_{1(||,\perp)}(1 - P_d^2 P_a)}{1 - R_{1(||,\perp)}^2 P_d^2 P_a} \tag{3.2}$$

In an indoor environment we are dealing with short finite slabs meaning that the number of internal reflections are not infinite, therefore requiring the truncation of the infinite series expansion to a finite expansion. Also the transmitter is usually modelled using a line-source, point source or hertzian dipole which means that the angle of entry θ_i into the surface is decreasing as the number of internal reflections increases (see Figure 3-2), whereas a planewave assumptions says that the angle of entry into the surface never changes for each internal reflection. Although Burnside's approximation might be perfectly valid for the application of transmission in an indoor ray-tracing, we can not conclude this without closer investigation of the method. Many ray-tracing tools use Burnsides method to augment the reflection coefficient result usually because it is a simple formula to implement.

As an aside, we found that Burnside states that the transmission coefficient is

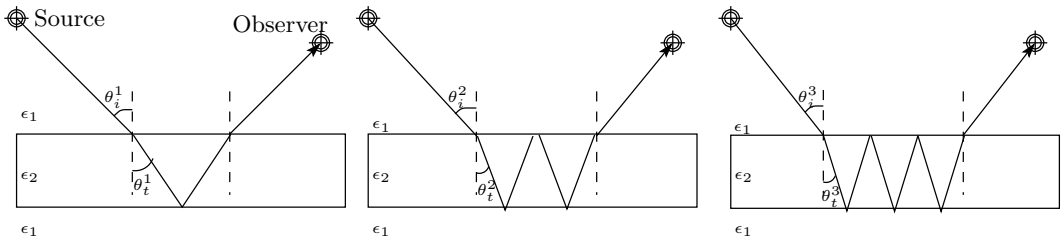

Figure 3-2: Different configuration that might be considered for slab penetration.

defined as $T_1 = 1 + R_1$ in the case of an electric and magnetic line source, but this is in fact incorrect, as can be seen from the derivation by Balanis[7], Ch. 5. This result is only correct for the electric (horizontal) polarisation case when $T_\perp = 1 + R_\perp$. In the case of the magnetic (vertical) polarisation case the formula should be of the form $\cos\theta_i(1 + R_{||}) = \cos\theta_t T_{||}$. Although the final result stated above in equation (3.2) is correct for both polarisations, the paper is confusing. For instance, Laurenson[53] stated that the result for the vertical polarisation case was neglected and proceeded to derive his own formula failing to notice that his formula reduced to the result of Burnside because of the identity $T_1T_2 = (1 - R_1^2)$ for both the electric and magnetic polarisation cases.

3.2.1 Internal reflections in a lossless dielectric slab

We propose that a full raytrace be compared with the result of Burnside. By full raytrace, we mean that in the case of a lossless dielectric slab, one can use the method of images to find a finite set of internal reflections in a slab of finite length. In the lossless dielectric case we will see that the derivation of a finite set of internal reflections in the slab is quite straight forward due to a clever geometrical construction, but the lossy case not derived by Burnside (see next section) is much trickier. Instead of recursively building an automated method of images obtaining the n^{th} order images of a transmitter leading to the calculation of the n^{th} order reflection coefficient in the dielectric slab, we can define a simple formula for any n^{th} order reflection without calculating any images using the method now stated below.

If we set up the geometry for a line-source, point-source or planewave as in Figure

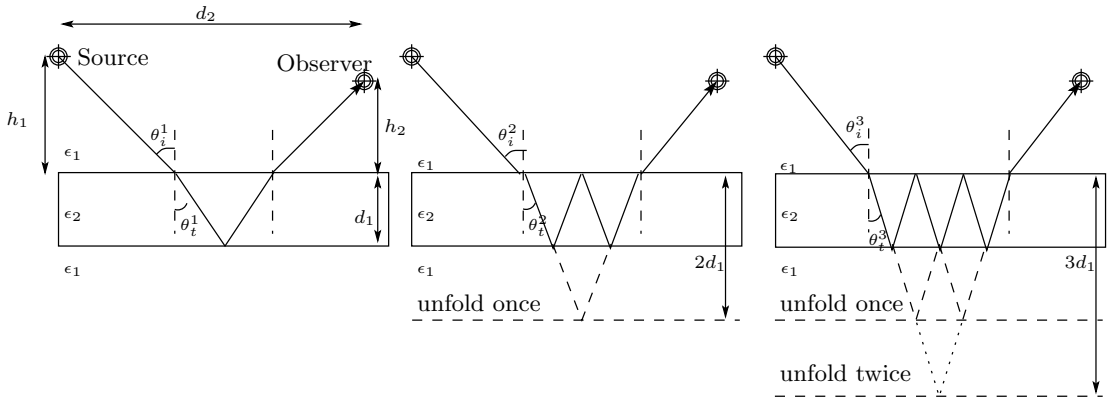

Figure 3-3: Geometrical construction for first, second and third order internal reflections

3-3, we see that we can define a simple formula with unknowns θ_i and θ_t as follows:

$$(h_1 + h_2)\tan\theta_i + 2d_1\tan\theta_t \quad = \quad d_2 \tag{3.3}$$

but we know also from Snell's law of refraction for lossless dielectrics that:

$$k_1 \sin\theta_i \quad = \quad k_2 \sin\theta_t \tag{3.4}$$

Substituting equation (3.4) into equation (3.3) and defining $x = \sin^2\theta_i$ we obtain the formula:

$$f(x) = 0 \quad = \quad d_2\sqrt{\epsilon_r - x(1+\epsilon_r) + x^2} - h\sqrt{\epsilon_r x - x^2} - 2d\sqrt{x - x^2} \tag{3.5}$$

where $h = h_1 + h_2$.

This formula looks cumbersome at first, but θ_i is easily obtained using one of two simple numerical techniques, the bisection algorithm or Newton Raphson formula (see Appendix A). In the case of the Newton Raphson formula we require the derivative of the function $f(x)$ as:

$$f'(x) = \frac{d_2(2x - (1+\epsilon_r))}{2\sqrt{\epsilon_r - x(1+\epsilon_r) + x^2}} - \frac{h(\epsilon_r - 2x)}{2\sqrt{\epsilon_r x - x^2}} - \frac{d_1(1-2x)}{\sqrt{x - x^2}} \tag{3.6}$$

It might be asked, why would we resort to a numerical technique when it is possible to construct the points of transmission exactly? The answer lies in the fact that we can not calculate the points of transmission using a standard method of images for the

lossless and lossy dielectric cases, and for that reason we use the numerical technique in both cases.

From this result we obtain the first order reflection coefficient for a point source given by:

$$R_{\perp} = \frac{\cos\theta_i - \sqrt{\epsilon_r - \sin^2\theta_i}}{\cos\theta_i + \sqrt{\epsilon_r - \sin^2\theta_i}} \tag{3.7}$$

$$R_{||} = -\frac{\epsilon_r\cos\theta_i + \sqrt{\epsilon_r - \sin^2\theta_i}}{\epsilon_r\cos\theta_i + \sqrt{\epsilon_r - \sin^2\theta_i}} \tag{3.8}$$

which leads to the reflected field $\mathbf{E}_r^1$ given by

$$\mathbf{E}_r^1 = \mathbf{E}^i(R_1)R_1T_1^{(1)}T_2^{(1)}A_s(s,l)e^{-jks}P_aP_d \tag{3.9}$$

where $T_1^{(1)}$ is the first order transmission in the dielectric slab, $T_2^{(1)}$ is the transmission coefficient of the re-emergent ray from the slab, $\mathbf{E}^i$ is the incident field at the point R_1 of entry into the slab, s is the distance travelled from the exit point of the slab to the receiver point, and $\mathbf{E}^i(R_1)R_1 = (\mathbf{E}^i_{\perp}R_{\perp})e^r_{\perp} + (\mathbf{E}^i_{||}R_{||})e^r_{||}$.

The attenuation factor of the n^{th} order internal reflected ray is defined as

$$A_s^{(n)}(s,l) = \frac{\rho}{\rho_1 + 2nl + s} \tag{3.10}$$

where s is the distance travelled out of the slab to the receiver point, ρ is the distance from the source to the entry point into the slab and $2nl$ is the distance covered by $2n$ bounces inside the slab.

Now if we reflect the slab as shown in Figure 3-3 for the second and third order internal reflections we see quickly that a similar formula exists for the calculation of both θ_i and θ_t as in equation (3.3) above. It is easily seen that the n^{th} order internal reflection results in a formula given by:

$$h\tan\theta_i^{(n)} + 2nd_1\tan\theta_t^{(n)} = d_2 \tag{3.11}$$

The resultant formula for the calculation of θ_i is given by:

$$f(x) = 0 = d_2\sqrt{\epsilon_r - x(1+\epsilon_r) + x^2} - h\sqrt{\epsilon_r x - x^2} - 2nd_1\sqrt{x - x^2} \tag{3.12}$$

Each term of the total reflection coefficient is similar to that given by equation (3.1) and the total reflection coefficient is therefore expressed as:

$$\overline{R} = R_1^{(0)} - \sum_{m=1}^{n} T_1^{(m)} T_2^{(m)} R_1^{(m)2m-1} P_d^{(m)2m} P_a^{(m)m} \tag{3.13}$$

except that each $R_1^{(m)}$ contains different angles of $\theta_i^{(m)}$ and $\theta_t^{(m)}$ for each m^{th} order internal reflection. Because the angles change in each term, the result does not collapse to a single term as in Burnside's geometric series expression.

3.2.2 Internal reflections in a lossy dielectric slab

As stated before, the case of internal reflections inside the lossy dielectric slab is much more cumbersome to formulate. A method of images solution does not hold because the complex permittivity of the slab alters the direction of the incoming wave. On entry into the slab, a planewave sets up a constant phase plane. The true angle of refraction is no longer θ_t as in the lossless case. In fact we will see that θ_t is itself complex. From Snells law of refraction we know that

$$\gamma_1 \sin\theta_i \;=\; \gamma_2 \sin\theta_t \tag{3.14}$$

where $\gamma_1 = j\beta_1 = j\omega\sqrt{\mu\epsilon_1}$ and $\gamma_2 = \alpha_2 + j\beta_2 = \sqrt{-\omega^2\mu\epsilon_2 + j\omega\mu\sigma}$ where σ is the conductivity of the slab, $\alpha_2 = k_1\sqrt{\frac{\epsilon'}{2}}\sqrt{\sqrt{1+\left(\frac{\sigma}{\omega\epsilon_2}\right)^2} - 1}$ and $\beta_2 = k_1\sqrt{\frac{\epsilon'}{2}}\sqrt{\sqrt{1+\left(\frac{\sigma}{\omega\epsilon_2}\right)^2} + 1}$. $\epsilon' = \epsilon_2/\epsilon_1$ is the relative permittivity in the slab. This is explained more in Balanis[7], Ch. 5.

It follows that:

$$\cos\theta_t \;=\; \sqrt{1-\sin^2\theta_t} = \sqrt{1 - \left(\frac{j\beta_1}{\alpha_2 + j\beta_2}\right)^2 \sin^2\theta_i} \tag{3.15}$$

$$\;=\; \sqrt{1 - \frac{\sin^2\theta_i}{\epsilon' - j\frac{\sigma}{\omega\epsilon_1}}} \tag{3.16}$$

$$\;=\; \sqrt{\frac{\epsilon'^2 + \left(\frac{\sigma}{\omega\epsilon_1}\right)^2 - \epsilon'\sin^2\theta_i - j\frac{\sigma}{\omega\epsilon_1}\sin^2\theta_i}{\epsilon'^2 + \left(\frac{\sigma}{\omega\epsilon_1}\right)^2}} \tag{3.17}$$

Now if we set $a = \epsilon'^2 + \left(\frac{\sigma}{\omega\epsilon_1}\right)^2 - \epsilon' \sin^2\theta_i$ and $b = -j\frac{\sigma}{\omega\epsilon_1}\sin^2\theta_i$ then

$$\overline{\alpha} = s\cos\zeta = \sqrt{\frac{a}{2\left(\epsilon'^2 + \left(\frac{\sigma}{\omega\epsilon_1}\right)^2\right)}}\sqrt{\sqrt{1+\left(\frac{b}{a}\right)^2} - 1} \tag{3.18}$$

$$\overline{\beta} = s\sin\zeta = \sqrt{\frac{a}{2\left(\epsilon'^2 + \left(\frac{\sigma}{\omega\epsilon_1}\right)^2\right)}}\sqrt{\sqrt{1+\left(\frac{b}{a}\right)^2} + 1} \tag{3.19}$$

$$p = s(\alpha_2\cos\zeta - \beta_2\cos\zeta) \tag{3.20}$$

$$q = s(\alpha_2\sin\zeta + \beta_2\cos\zeta) = \alpha_2\overline{\beta} + \beta_2\overline{\alpha} \tag{3.21}$$

For a uniform planewave travelling from medium 1 into medium 2, the transmitted field is then written as:

$$\mathbf{E}^t = \mathbf{E}_2\exp\{-(\alpha_2 + j\beta_2)(x\sin\theta_t + y\cos\theta_t)\} \tag{3.22}$$

$$= \mathbf{E}_2 e^{-yp}\exp\{-j(\beta_1 x\sin\theta_i + yq)\} \tag{3.23}$$

The transmitted field is clearly non-uniform but if we define the instantaneous field as:

$$\mathbf{E}^t = \Re(\mathbf{E}^t e^{j\omega t}) = \mathbf{E}_2 e^{-yp}\exp\{-j(\omega t - \beta_1 x\sin\theta_i + yq)\} \tag{3.24}$$

then we can define the imaginary coefficient to be a constant term if we set

$$t = \beta_1\sin\theta_i \tag{3.25}$$

then

$$\omega t - (\beta_1 x + yq) = \omega t - \sqrt{t^2+q^2}(x\sin\psi_2 + y\cos\psi_2) \tag{3.26}$$

$$= \omega t - k_{2e}(x\sin\psi_2 + y\cos\psi_2) \tag{3.27}$$

giving us an angle ψ_2 being the angle of transmission into the slab instead of θ_t, setting up constant phase planes perpendicular to the direction of propagation, which is what we would expect (see Figure 3-4).

Using the same setup as in the lossless case shown in Figure 3-3 we obtain the formula in θ_i and ψ_2 given by:

$$h\tan\theta_i + 2nd_1\tan\psi_2 = d_2 \tag{3.28}$$

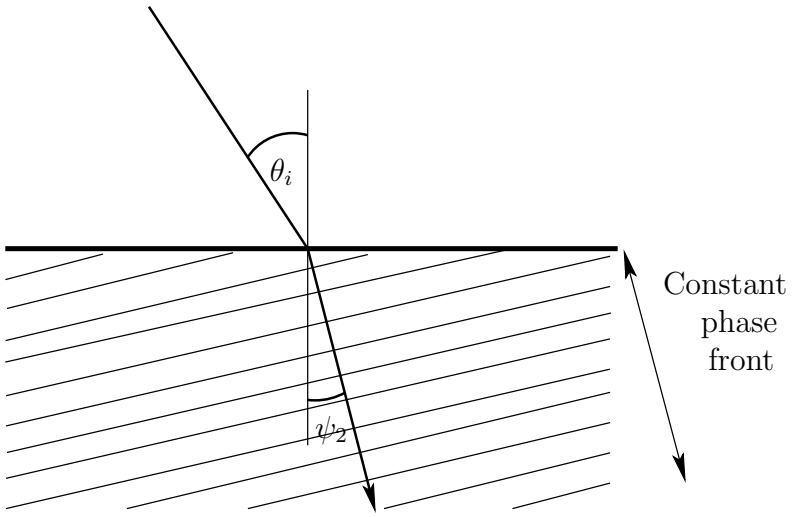

Figure 3-4: Planewave incidence on a lossy dielectric media.

which can be solved by the bisection algorithm or Newton Raphson method as stated for the lossless case.

It is important to realise that the terms in equation (3.13) are slightly different. The term P_d giving the phase related to the distance travelled in the dielectric from one side of the slab to the other is now given by: $P_d = e^{-jk_2 l} = e^{-yp} e^{-jk_{2e}(x \sin\psi_2 + z \sin\psi_2)}$. P_a also changes because our real valued angle is ψ_2 not θ_t as before, therefore $P_a = e^{jk2l \sin\psi_2 \sin\theta_i}$.

3.3 Results of Comparison with Burnside or Known Solutions

3.3.1 Example 1: Lossless Dielectric with Transmitter and Receiver Close Together

A dielectric slab of thickness $d_1 = 0.2$ metres was used to test the ray-tracing based solution for the internal reflections with the solution obtained by Burnside as explained in Section 3.2.1. The position of the line source was $(-r\cos\theta, 0, r\sin\theta)$ and the receiver is placed at $(r, 0, r)$ as shown in Figure 3-5. The angle θ was allowed to vary between 1^o and 90^o. r has a value of 10 metres for this calculation.

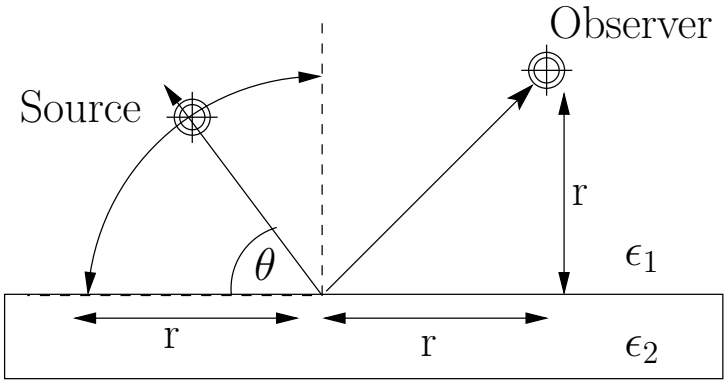

Figure 3-5: Dielectric slab with positioning of transmitter and receiver.

The constants $h_1 = r\sin\theta$, $h_2 = r$ and $d_2 = r\cos\theta + r$ are easily deduced and can be substituted into equation (3.11). The dielectric is firstly assumed to be lossless, but the lossy results will also be presented later. A relative permittivity of $\epsilon_r = 4.0$ was chosen for this particular example. The results obtained are shown in Figure 3-6.

The results are plotted for an infinite order ray-trace obtained by using the method in Section 3.2.1. In can be seen that the results vary around the first order reflection results. This result was obtained using only the incident field and the reflection off the plate. The solution of Burnside is significantly different that the result obtained from the ray-tracing solution as expected. The ray-tracing needs only to be run with up to 5^{th} order images in practice because the solution quickly converges to a stable solution, this is shown in Figure 3-7.

3.3.2 Example 2: Lossless Dielectric with Transmitter and Receiver Far Apart

For this next example, we assume the same geometry as in Figure 3-5 except that the radius r of the circle is redefined to be $10r$. The receiver point is left in the same position as before. All other variables remain the same also. The results are shown in Figure 3-8.

Again there is a sizable difference between Burnside's results and the full ray-tracing result.

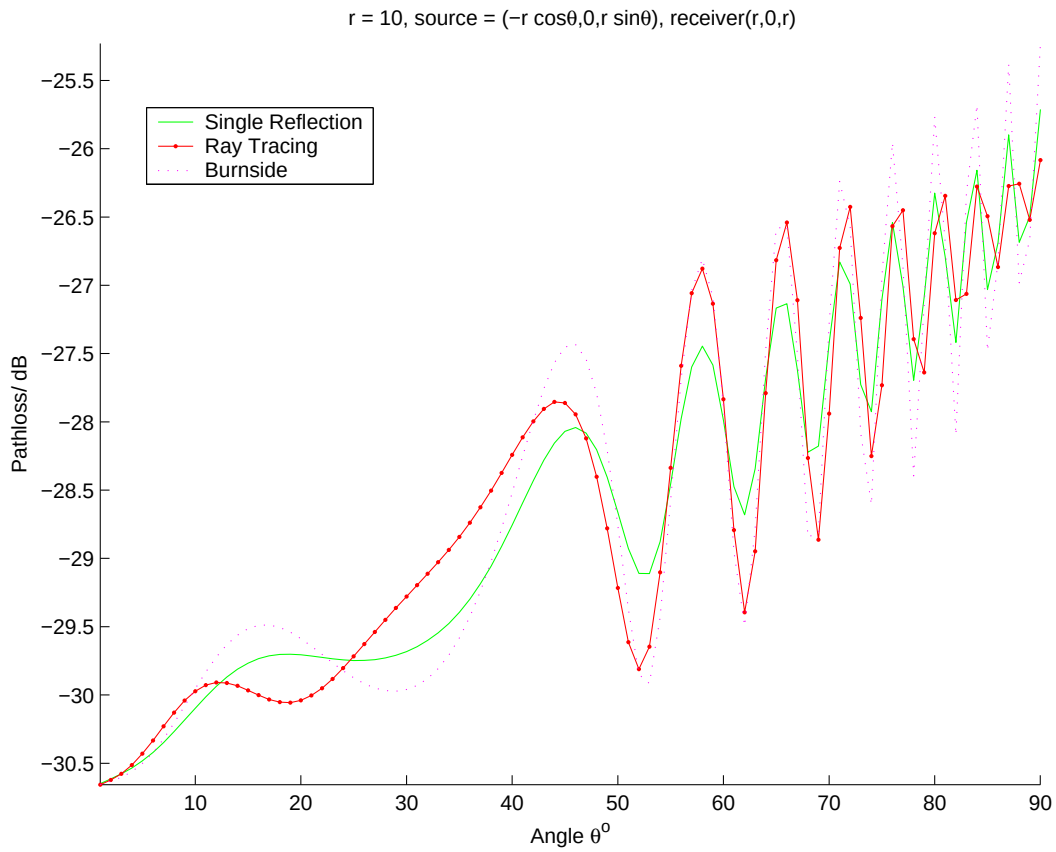

Figure 3-6: The results for the geometry in Figure 3-5 with lossless relative permittivity $\epsilon_r = 4$.

3.3.3 Example 3: Lossy Dielectric and Transmitter and Receiver Close Together

The values of the configuration are identical to the parameters in Example 1 except that the permittivity of the slab is complex. The permittivity is defined to be:

$$\epsilon_2 = \epsilon_1 \left(\epsilon_r - j \frac{\sigma}{\omega \epsilon_1} \right) \tag{3.29}$$

$$= \epsilon_1 \epsilon_r \tag{3.30}$$

where the relative permittivity is given by ϵ_r. For a typical concrete wall, the conductivity is of the order of 1.0×10^{-2}. In this case the relative permittivity has a value of $\epsilon_r = 4.0 - j0.08987$. The full raytracing solution versus the solution obtained by a single reflection is presented in Figure 3-9. Burnside does not have a solution for this problem so no results are presented here for comparison. There is a very

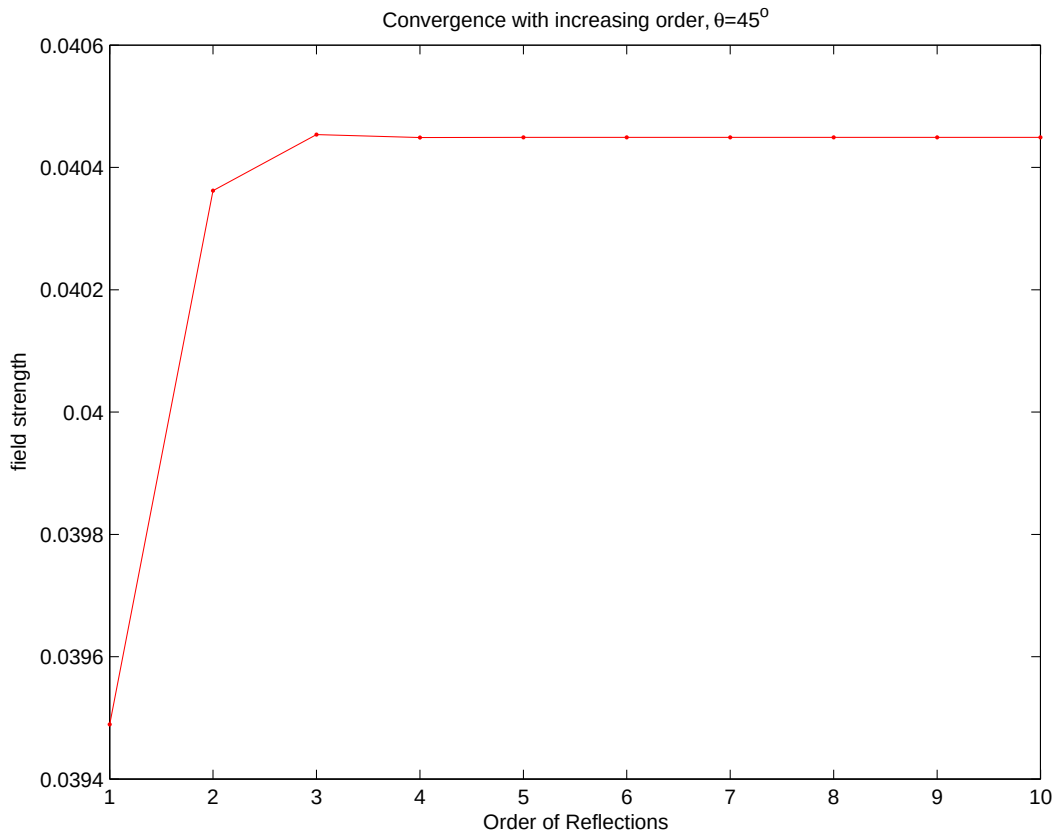

Figure 3-7: The convergence of the raytracing for increasing orders of reflection given that $\theta = 45^o$ and $r = 10$.

noticable difference between the full ray-tracing result and the 1^{st} order reflection result.

3.3.4 Example 4: Lossy Dielectric with Transmitter and Receiver Far Apart

For this example the configuration of Example 2 with the transmitter located on a circle of radius $10r$ is considered again. The complex permittivity of Example 3 is considered also. The comparison is made between the result for the full ray-tracing solution and the single reflection result. The results are quite different in places.

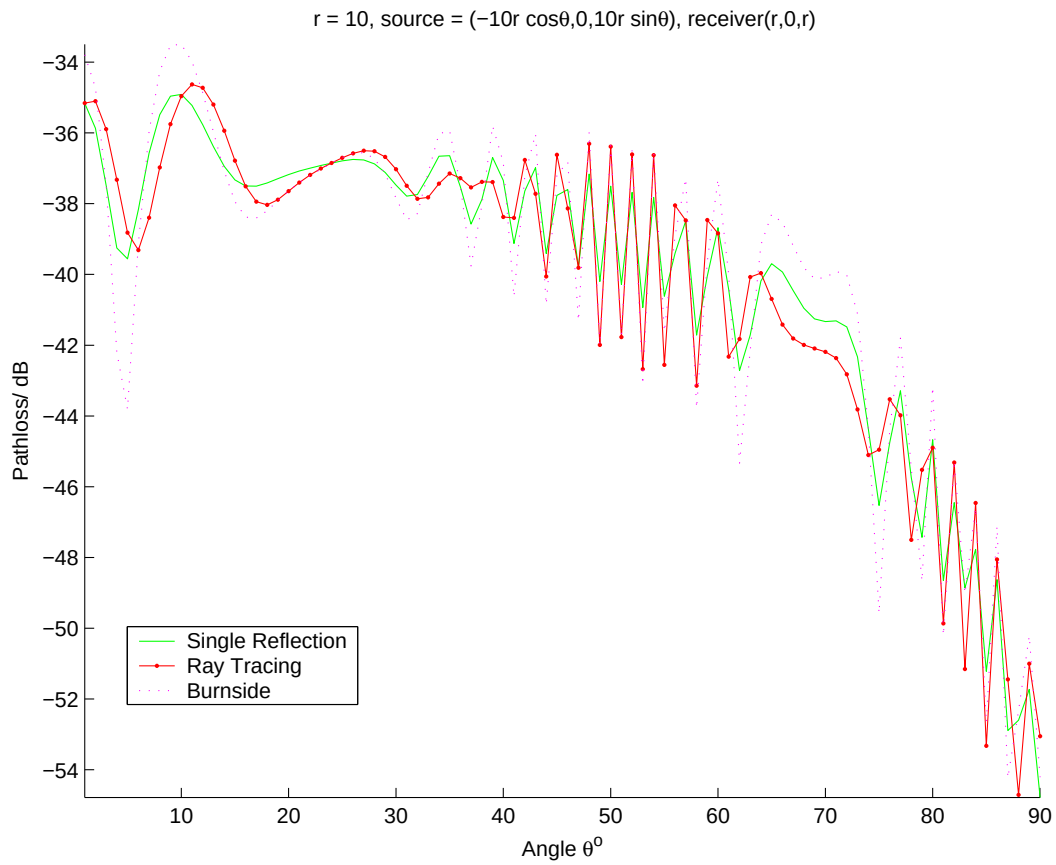

Figure 3-8: The results for the geometry in Figure 3-5 with a radius change r defined to be 10 times larger.

3.4 Problems Associated with UTD Diffracted Fields

There are a number of problems that exist in the UTD diffraction coefficients which need to be addressed. All of these have been highlighted before in previous papers and books. Six such problems are named here for completeness although more may exist. This section serves as a record of such issues that are partially addressed in the next section and are addressed in the literature using other methods.

The problems known in UTD are as follows:

1. In the UTD formulation described by Balanis [7], Ch. 13 for a simple perfect electrical conducting wedge, there are a number of problems that exist. The

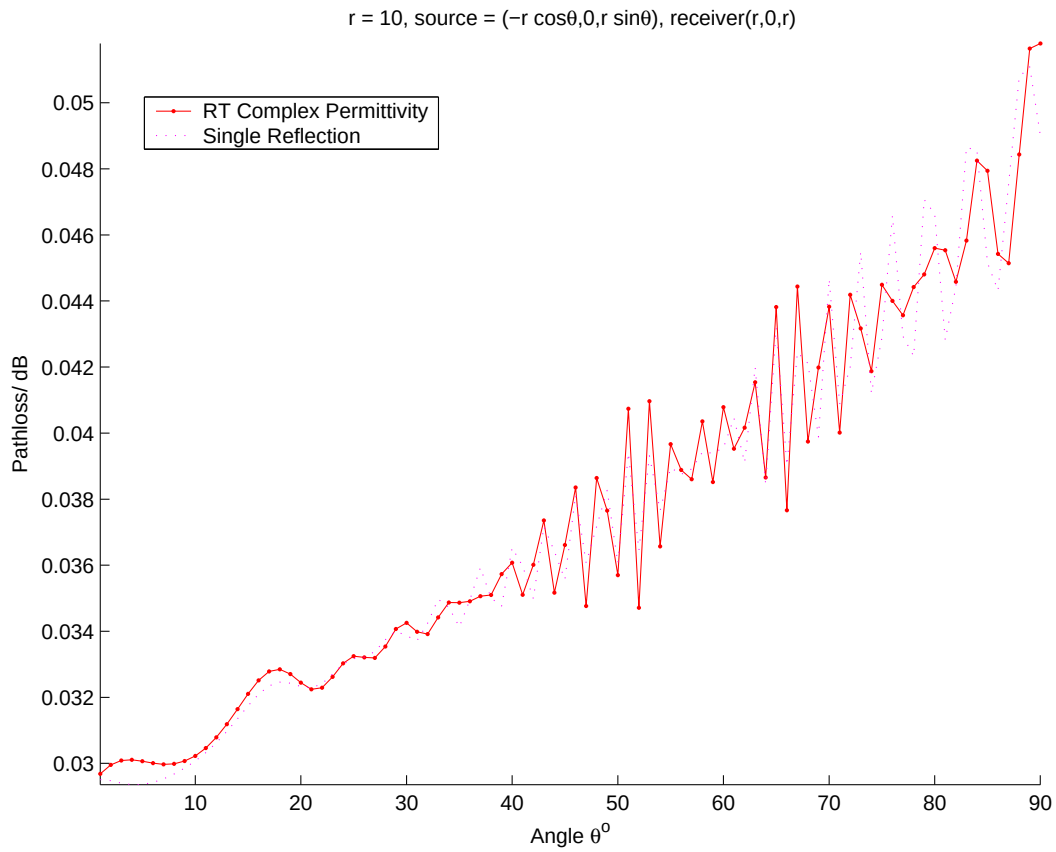

Figure 3-9: The results for the geometry in Figure 3-5 using ray-tracing for a lossy media.

assumption that $s' \gg 0$ leads to

$$H_0^{(2)} \cong \sqrt{\frac{2j}{\pi k s'}} e^{-jks'} \tag{3.31}$$

which becomes less accurate when $ks' < 3$. Also the assumption that $s \gg 0$ leads to the assumption that

$$\int_{\text{steepest descent path}} H(z) e^{ksh(z)} dz \tag{3.32}$$

can be evaluated. But $s \gg 0$ is not necessarily true since the receiver point may be placed close to the diffraction point (see Figure 3-11). Both assumptions give rise to the one problem. If a point it too near the diffraction point then the UTD formulation becomes invalid.

2. Low angles of incidence yield a soft diffraction coefficient $D_s \to 0$, but this is not correct. Slope diffraction as presented in Balanis[7], Ch. 13, James[37]

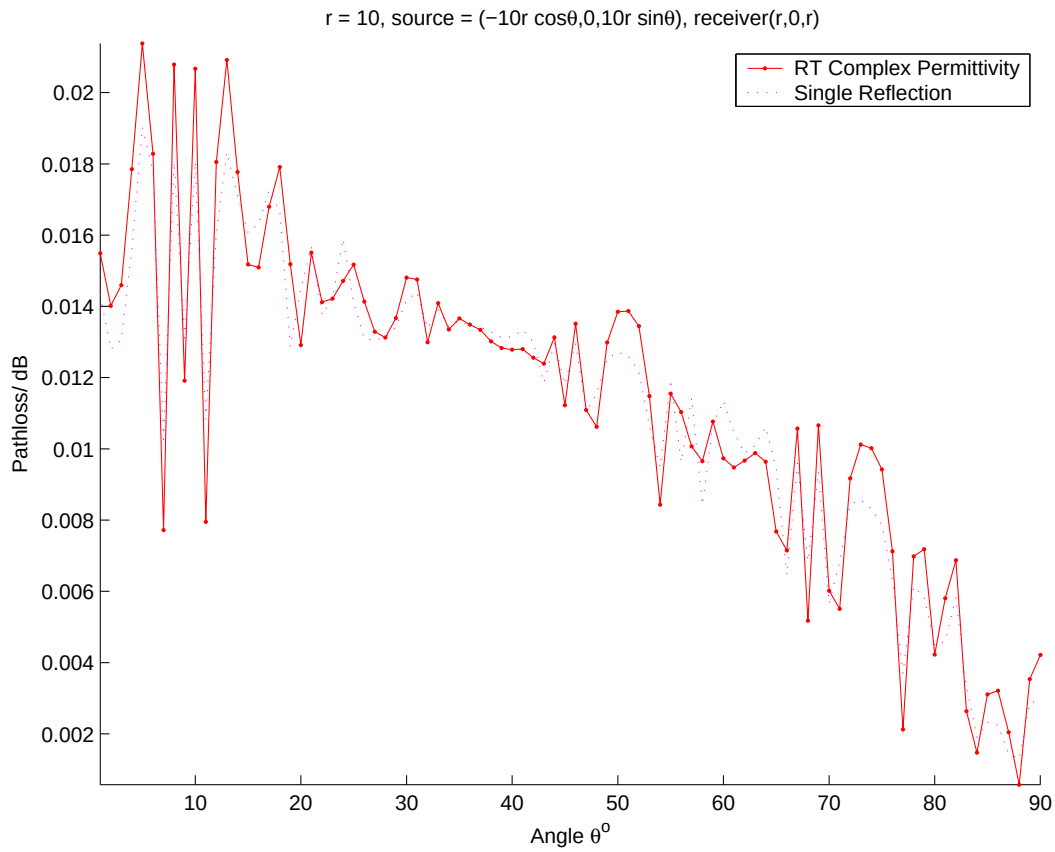

Figure 3-10: The results of the ray-tracing for a lossy media with transmitter and receiver far apart..

and Jones[41] is used to supplement the solution. Other references such as Cockrell[20] exist for specific antenna types.

3. Off Keller Cone diffraction points, may exist but be required to give a diffracted field (see Figure 3-12). These points will give zero field when using UTD. Many methods have been used to obtain fields in the off Keller cone regions, using methods such as modified physical optics [57], [1], [36], or incremental length diffraction coefficients (ILDC) [75], [84] and equivalent edge currents [40], [59]-[61].

4. El-Sallabi[23] states that Luebbers[74] dielectric formula gives poor results in Shadow regions. These results are not necessarily correct since there is no account of transmission through windows and doors taken into account. The

only way to confirm the results of this paper is to calculate the results in an anechoic chamber under controlled conditions.

5. If diffraction points are close together, then higher order terms such as double diffraction described by Balanis[7], Luebbers[74], Holm [31] need to be included to account for coupling between the wedge points.

6. Erricolo[24] states that when a source and observer have no line of sight as shown in Figure 3-13, that the single diffraction coefficient is no longer sufficient for good accuracy and therefore double diffraction must be introduced. Again Luebbers [74] is a good paper on the subject of double diffraction techniques.

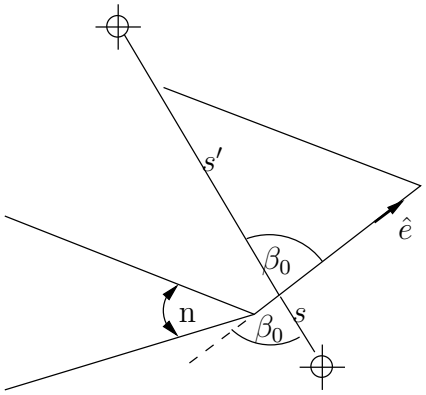

Figure 3-11: Wedge with receiver point a short distance from diffraction point.

3.5 Solution of 3D Plate Problem

The solution of the two dimensional flat plate problem is solved exactly using the three dimensional electric field integral equation solution to the Helmholtz equation given by:

$$\mathbf{E}^s = -j\omega\mathbf{A} - \nabla\mathbf{\Phi} \tag{3.33}$$

where the magnetic vector potential $\mathbf{A}$ is defined as

$$\mathbf{A}(\mathbf{r}) = \sqrt{\frac{\mu}{4\pi}}\int_S J\frac{e^{-jkR}}{R}dS' \tag{3.34}$$

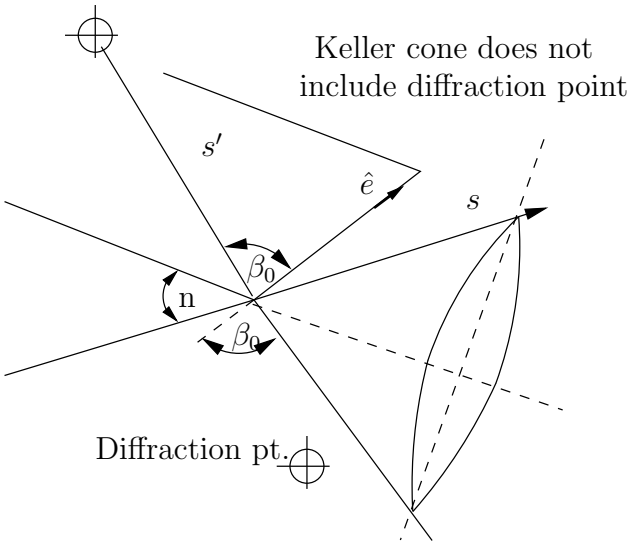

Figure 3-12: A diffraction point that yields no field because it is not on a Keller cone.

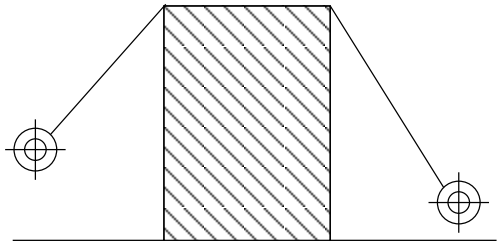

Figure 3-13: No single diffraction point exists between receiver and transmitter.

and the scalar potential $\mathbf{\Phi}$ is defined as:

$$\mathbf{\Phi}(\mathbf{r}) \;=\; \frac{1}{4\pi\epsilon}\int_S \sigma \frac{e^{-jkR}}{R} dS' \tag{3.35}$$

where σ is the surface charge density related to the surface divergence of $\mathbf{J}$ through the continuity equation

$$\nabla_s \cdot \mathbf{J} \;=\; -j\omega\sigma \tag{3.36}$$

The boundary conditions are enforced by using the condition that $\hat{n}\times(\mathbf{E}^i+\mathbf{E}^s) = 0$ on S the surface of the rectangular flat plate.

The full moment method solution is described by Rao, Wilson, Glisson[69]. The plate is split into triangular facets each of which have basis functions defined on their edges. This allows the current density $\mathbf{J}$ to be calculated numerically and following that, $\mathbf{E}^s$ can be derived by equation (3.34) substituted into equation (3.33). The

matrix equation resulting from the full solution is very time consuming to calculate and solve because the matrix is dense (most entries are non-zero). Many people have worked on methods to speed up the solution. Brennan[17] in particular has defined a method which iterates through the plate travelling across and back and up and down until the solution converges. The solution is not straight forward to calculate. He needed to introduce a buffer zone when iterating up the plate, to avoid spurious diffracted field interactions when solving for subsections of the plate in isolation. The results obtained by Brennan will serve as the canonical solution to the plate problem and will be used for comparisons with the scattered field obtained by using a full ray-trace incorporating UTD diffraction coefficients. By full ray-trace we mean that there can be one reflection from the surface and up to four diffractions, one from each edge of the plate (see Figure 3-14). Note that the scale of the rectangular plate is not in equal aspect ratio for this plot.

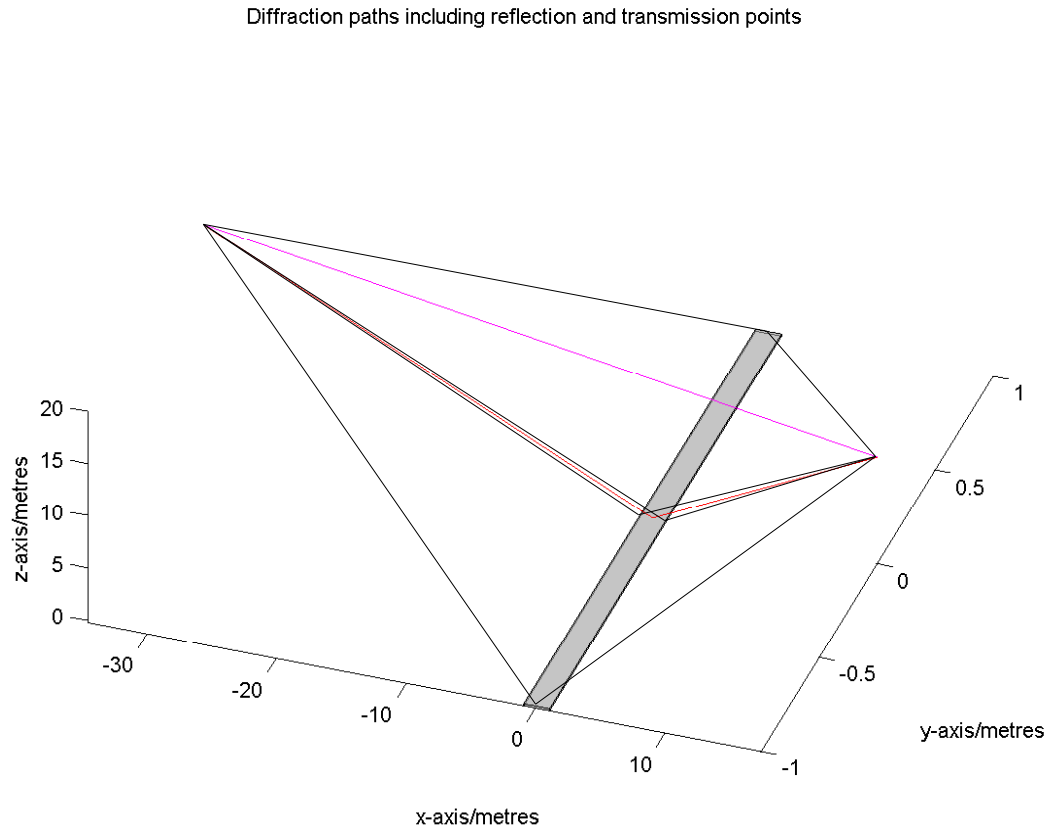

Figure 3-14: Ray-trace on 2D plate with one reflection and 4 diffractions.

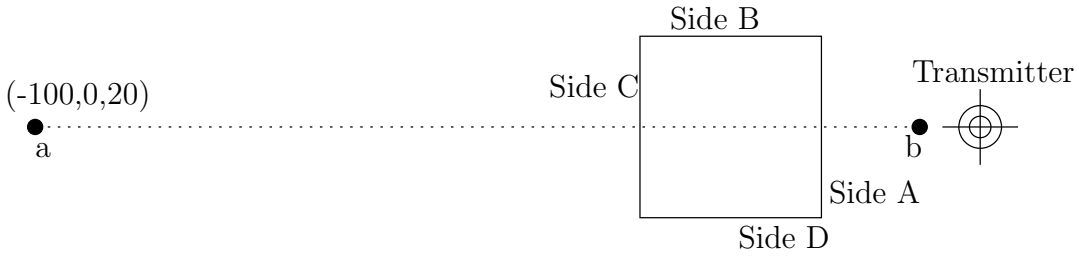

Figure 3-15: The geometry of a 3D plate, transmitter and receiver points on a line.

For a suitable test problem (see Figure 3-15) the integral equation was solved over a plate of size $6\lambda \times 6\lambda$ which at a frequency of 900MHz will give a plate of size 2 metres $\times$2 metres. The half-wave dipole position was defined to be located at $T_x = (r\sin\theta\cos\phi, r\sin\theta\sin\phi, r\cos\theta) = (10\sqrt{3}, 0, 10)$ when $r = 20, \theta = 60^o$ and $\phi = 0^o$.

The receiver points are defined along a line segment $[a, b]$ above the plate. The value $a = (-100, 0, 20)$ and $b = (20, 0, 20)$ and the interval of 0.1 between each point on the line results in 1201 receiver points. The results are shown in Figure 3-16 for the UTD. The plot shows the diffracted fields from side A, side B and D combined, side C and the reflected field. The complete scattered field is also shown made up of the sum of all diffracted fields and reflected field.

When comparing the scattered field with that obtained by Brennan as shown in Figure 3-17 the results do not agree. The reason for the mismatch seems to be due to the changing directions of the diffracted field curves. The diffracted rays obtained in the ray-tracing were checked and found to be correct. In Section 2.7.2 in the previous chapter the diffraction coefficients where shown to give perfect agreement with Balanis's results. Also all values such as ϕ, ϕ' and β_0 where checked for correctness. The fact that the plate is of short finite width is most likely the reason for the discrepancy. When running the solution for larger sized plates there is no large jump like the ones encountered here. Holm[31] shows exactly the same sort of result for a double knife edge diffraction problem with a large spike in the scattered field very similar to the one observed in Figure 3-16. Holm describes how it is possible to use higher order term to smooth out the spike but at a large computational expense.

The diffracted fields assume that each edge of the plate is along an infinite wedge,

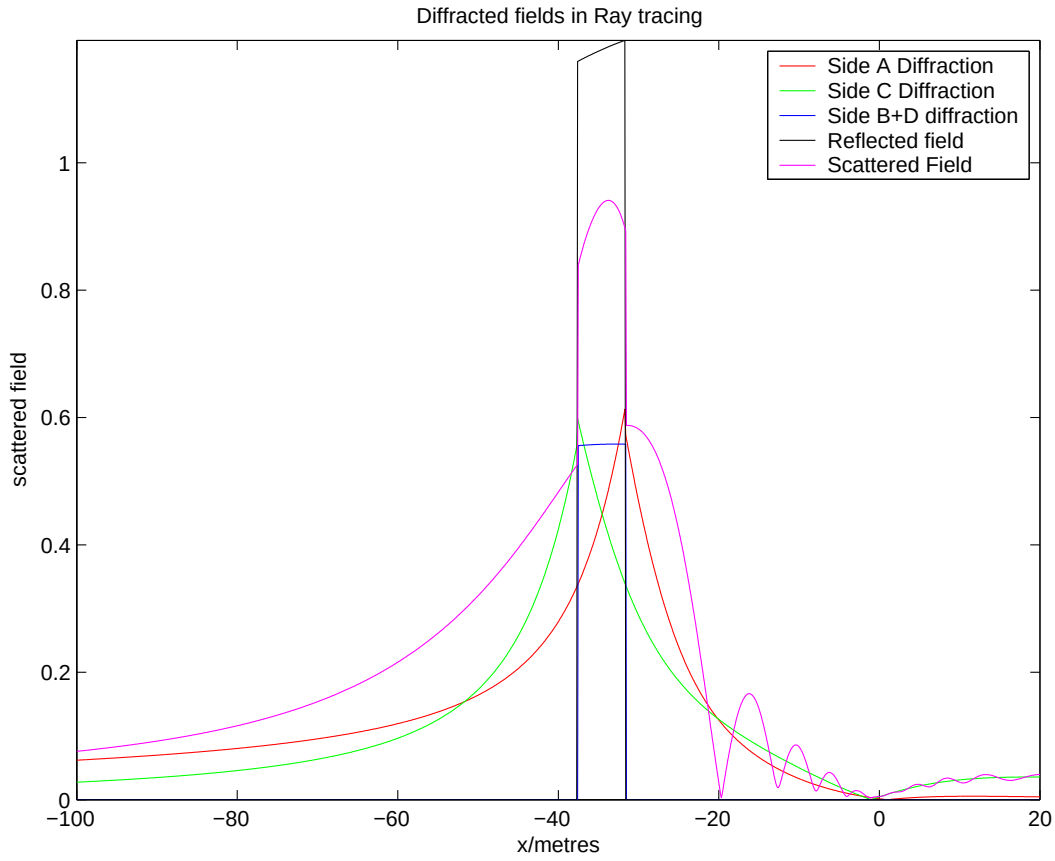

Figure 3-16: Diffracted field for ray-tracing plus reflected field.

which is definitely not correct. If we could define an analytical formula for the diffracted field that corrects UTD at low angles of incidence and removes the discrepancy of UTD while having a low computational cost, this would be a substantial achievement. The rest of this section will concern itself with the single plate problem and results are presented for a two dimensional truncated half-plane (THP) solution that helps correct the UTD solution in three dimensions.

3.6 Correction to Diffracted Fields Over a Flat Plate

The majority of the contribution to the scattered field should come from Sides A and C in the example just described. Since walls in buildings are usually connected to both floor and ceiling, they only have two diffraction edges. Keeping this in mind,

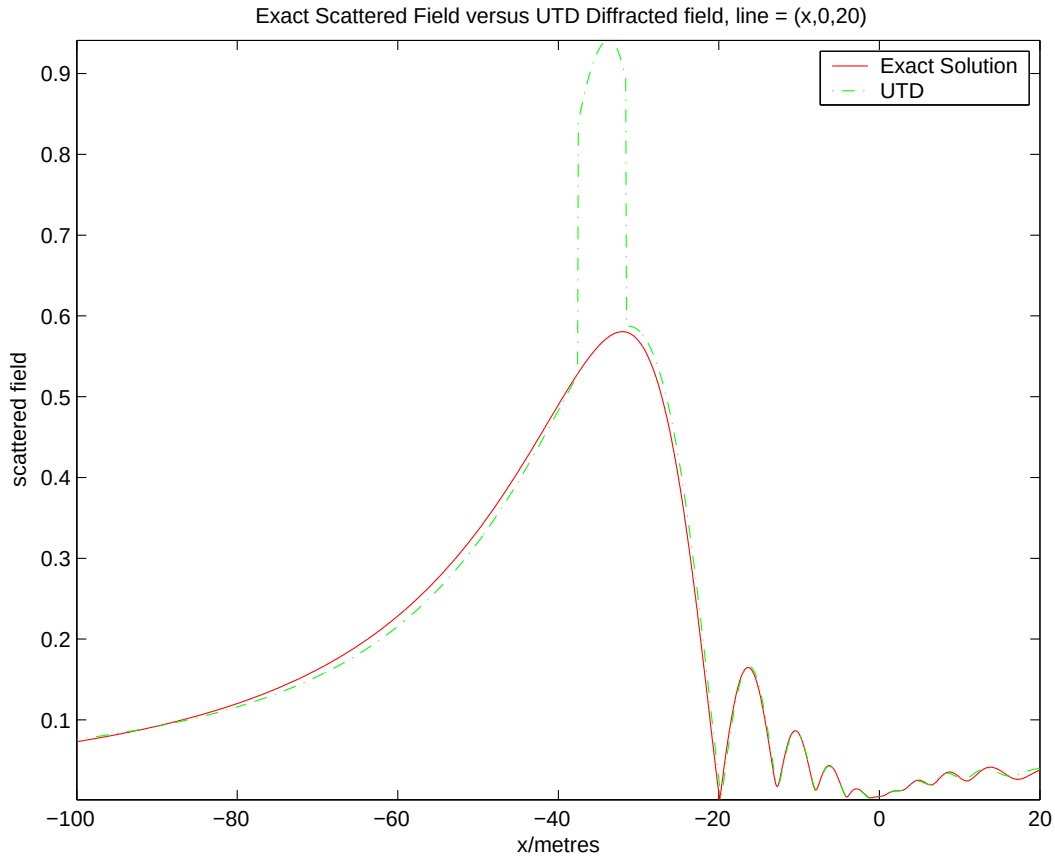

Figure 3-17: UTD solution versus canonical moment method solution.

what follows is a two dimensional solution to the scattered field over a finite plate which can then be modified to give the three dimensional result. The two dimensional formulation requires a line-source or planewave instead of a point-source to make the solution calculable.

3.6.1 The Electromagnetic Problem

The electromagnetic field is emitted by an antenna defined to be transverse magnetic in z (TM_z). The antenna is an isotropic line-source emitting into a lossless media in the presence of a perfect electrically conducting scatterer. The method of solution is the two-dimensional Helmholtz equation.

What we now want to derive is an expression which will be used for an electric field integral equation.

We start with the Wiener-Hopf technique (see [37], [33]) for a half-plane excited

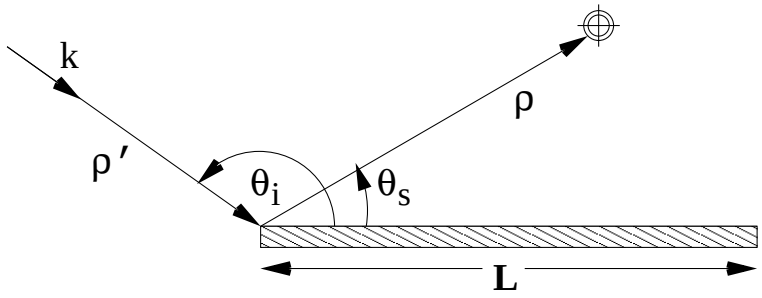

Figure 3-18: The geometry of the truncated half-plane problem

by a plane wave, and then truncate it, to give a finite plate solution (see Figure 3-18). The incident field $\mathbf{E}_i$ and total field $\mathbf{E}_t$ for any incoming angle θ_i is defined as:

$$\mathbf{E}_i(\rho', \theta_s) = \hat{z}\mathbf{E}_o e^{\jmath k\rho'(\cos\theta_s - \cos\theta_i)} \tag{3.37}$$

$$\mathbf{E}_t(\rho, \theta_s) = \hat{z}\sqrt{\frac{\jmath}{\pi}}\mathbf{E}_o[e^{\jmath k\rho\cos(\theta_s-\theta_i)}F(a_1) \mp e^{\jmath k\rho\cos(\theta_s+\theta_i)}F(a_2)] \tag{3.38}$$

where

$$F(a) = \int_a^\infty e^{-\jmath\tau^2}d\tau \tag{3.39}$$

$$a_1 = -\sqrt{2k\rho}\cos((\theta_s - \theta_i)/2) \tag{3.40}$$

$$a_2 = -\sqrt{2k\rho}\cos((\theta_s + \theta_i)/2) \tag{3.41}$$

Equation (3.38) represents the total field for both electric and magnetic field integral equations. The case when the $\mp$ sign is minus gives the electrically polarised diffracted field (soft polarization), while a plus sign gives the magnetically polarised diffracted field (hard polarization).

Using Maxwells equations:

$$\nabla \times \mathbf{E}_t = -\jmath\omega\mu\mathbf{H} \tag{3.42}$$

$$\mathbf{J} = \hat{y} \times (\mathbf{H}_1 - \mathbf{H}_2) \tag{3.43}$$

where $\mathbf{H}_1(\rho, \theta_s) = \mathbf{H}(x, 0^+)$ is the current on the upper half of the plate, and $\mathbf{H}_2(\rho, \theta_s) = \mathbf{H}(x, 2\pi^-)$ is the current on the lower half of the plate, satisfying the boundary conditions. Substituting equation (3.38) into equations (3.42) and (3.43) gives the current density $\mathbf{J}$ defined by:

$$\mathbf{J} = \hat{y} \times (\mathbf{H}_1|_{(\rho=x,\theta_s=0^+)} - \mathbf{H}_2|_{(\rho=x,\theta_s=2\pi^-)}$$

$$= \frac{\hat{z}}{\jmath\omega\mu}\left[\frac{1}{\rho}\left.\frac{dE}{d\theta_s}\right|_{(\rho=x,\theta_s=0^+)} - \frac{1}{\rho}\left.\frac{dE}{d\theta_s}\right|_{(\rho=x,\theta_s=2\pi^-)}\right] \tag{3.44}$$

The resulting $\hat{z}$ component of the current density $\mathbf{J}$ is:

$$J_z = \frac{k}{2}\sin\theta_i e^{\jmath kx\cos\theta_i}\left[F(a) \mp F(-a)\right]\sqrt{\frac{\jmath}{\pi}} + \sqrt{\frac{k}{8\jmath\pi x}}\sin\frac{\theta_i}{2}\left[e^{-\jmath kx} \mp e^{-\jmath kx}\right] \tag{3.45}$$

where $a = \sqrt{2kx}\cos\frac{\theta_i}{2}$.

Taking the cases of the EFIE current density J_z and MFIE current density M_z separately we have from equation (3.45) that:

$$J_z = 2J_{PO}\sqrt{\frac{\jmath}{\pi}}F(a) + \sqrt{\frac{k}{2\jmath\pi x}}\sin\frac{\theta_i}{2}e^{-\jmath kx} \tag{3.46}$$

$$M_z = J_{PO} \tag{3.47}$$

where $J_{PO} = \frac{k}{2}\sin\theta_i e^{\jmath kx\cos\theta_i}$ is the physical optics current defined on the infinite strip.

The above result J_z is defined by Rossi[72][1]. M_z was used in a paper by Brennan [16] in the context of a solution of a closed body terrain problem consisting of many connected strips. At this point the magnetic field is no longer required so it will be dropped from the analysis. We now calculate the scattered field by integrating over a finite closed interval $[0, L]$ of the plate. This will give us the truncation of the plate necessary to correct the problems in the UTD solution. The result is a integral for the electric scattered field $\mathbf{E}_s$ and magnetic scattered field $\mathbf{H}_s$ defined by:

$$\mathbf{E}_s = \int_0^L J_z(x)e^{\jmath kx\cos\theta_s}dx \tag{3.48}$$

Using integration by parts we obtain:

$$\begin{aligned}\mathbf{E}_s &= -k\sin\theta_i\sqrt{\frac{\jmath}{2}}\left[\frac{e^{\jmath k\zeta L}}{\jmath k\zeta}\mathcal{F}^-(a_1) - \frac{1}{\jmath k\zeta}\frac{\cos\frac{\theta_i}{2}}{\sin\frac{\theta_s}{2}}\mathcal{F}^-(a_2)\right] \\ &- \frac{1}{\sqrt{2\jmath}}\frac{\cos\frac{\theta_i}{2}}{\sin\frac{\theta_s}{2}}\mathcal{F}^-(a_2)\end{aligned} \tag{3.49}$$

where $a_1 = \sqrt{\frac{4kL}{\pi}}\cos\frac{\theta_i}{2}$, $a_2 = \sqrt{\frac{4kL}{\pi}}\sin\frac{\theta_s}{2}$, $\zeta = \cos\theta_i + \cos\theta_s$, and $\mathcal{F}^-(a) = \int_0^a e^{-\jmath\frac{\pi}{2}\tau^2}d\tau$ is the negative fresnel integral which can be numerically integrated.

[1]Rossi had a mistake in his formulation which meant that his scattered field result was incorrect

It proves easy to integrate over the range $[0, L]$ when truncating the half-plane, but in practice the formulation is easier to expanded about the centre point of each plate (see Figure 3-18). In this case the integral must be transformed to give a result over the range $[-L/2, L/2]$. This is given by the following simple translation:

$$J_z(x) \quad \rightarrow \quad J_z(x + \frac{L}{2})$$

resulting in the transformed results for $\mathbf{E}_s$:

$$\mathbf{E}_s \quad = \quad \int_{-\frac{L}{2}}^{\frac{L}{2}} J_z(x + \frac{L}{2}) e^{\jmath kx \cos\theta_s} dx = e^{-\frac{\jmath k\zeta L}{2}} \int_0^L J_z(x) e^{\jmath kx \cos\theta_s} dx$$

Physically this is equivalent to shifting the plate by a factor $-L/2$ along the x-axis. The discontinuity at $x = 0$ then resides at $x = -L/2$ and the incident and scattered field must be adjusted accordingly. This is achieved by making the exponential shift as in the previous equation.

So the final result for the scattered field is:

$$\begin{aligned} \mathbf{E}_s \quad &= \quad -k \sin\theta_i \sqrt{\frac{\jmath}{2}} \left[\frac{e^{\frac{\jmath k\zeta L}{2}}}{\jmath k\zeta} \mathcal{F}^-(a_1) - \frac{e^{-\frac{\jmath k\zeta L}{2}}}{\jmath k\zeta} \frac{\cos\frac{\theta_i}{2}}{\sin\frac{\theta_s}{2}} \mathcal{F}^-(a_2) \right] \\ &- \quad \frac{e^{-\frac{\jmath k\zeta L}{2}}}{\sqrt{2\jmath}} \frac{\cos\frac{\theta_i}{2}}{\sin\frac{\theta_s}{2}} \mathcal{F}^-(a_2) \end{aligned} \tag{3.50}$$

3.6.2 Numerical solution of Truncated Half-Plane method

The scattered field in equation (3.49) is solved numerically using an expression for the fresnel integral presented in mathematical tables [3], or one of the numerical methods defined in numerical recipes in C [68].

There are a few areas where equation (3.50) needs special attention. We would expect to have a problem at the reflective shadow boundary (when $\theta_i = \pi - \theta_s$) due to a singularity that exists there. Although the terms in equation (3.50) can be collected up to form a sinc function, the solution was found to be unstable. Instead a small argument expression can be used like that of the uniform theory of diffraction around the transition regions [7]. Extrapolating about either side of the shadow boundary yields the correct result. In this case $\mathbf{E}_s$ is found by the following formula:

$$\mathbf{E}_s(\theta_i, \theta_s) \quad = \quad \frac{\mathbf{E}_s(\theta_i, \theta_s - \epsilon) + \mathbf{E}_s(\theta_i, \theta_s + \epsilon)}{2} \tag{3.51}$$

The other case of concern is the case when $\theta_s = 0$. In this case the scattered field is defined as:

$$\mathbf{E}_s = -\frac{e^{-\frac{\jmath k\zeta}{2}}}{\sqrt{\jmath}}\mathcal{F}^{-}(\sqrt{\frac{4kL}{\pi}}) \tag{3.52}$$

3.7 Results: Truncated Half-Plane Versus UTD

3.7.1 Comparison for Plane Wave Incidence

We first present the results for the solution of the electric field integral equation for a flat plate of length 10metres, with frequency 900MHz, and incoming angle $\theta_i = 175^o$. The impinging wave is assumed to be plane, as in Figure 3-18. The results are presented for far field scattering in the range $[0^o, 180^o]$ at 200 points. The Truncated half-plane method was implemented using equation (3.49) along with its special cases defined by equations (3.51) and (3.52). The uniform theory of diffraction (UTD) result is presented using the Keller approximation. The method of moments result was calculated using a conjugate gradient squared method to include the backscattering (see Golub[26], Kenny[43]).

The results are excellent for the lower spectrum of angles up to 90^o, but start to deteriorate in the backscattering region. This is because the result obtained by the truncated half-plane (THP) method only contains a forward propagating term. The difference arises because the method of moments (MoM) and UTD contain the diffraction from the far end of the plate which gives the backscattering result. What is notable is the fact that the UTD is corrected in the problem area in this case where $\theta_s < 20^o$. This is the region of most importance since we wish to make the correction at low angles.

3.7.2 Comparison with Exact MoM result

In this example the three dimensional plate described in Section 3.5 along with 1201 scattered field points and a point source is set up. The geometry of the problem is shown in Figure 3-15. Figure 3-20 shows again how the THP result corrects the

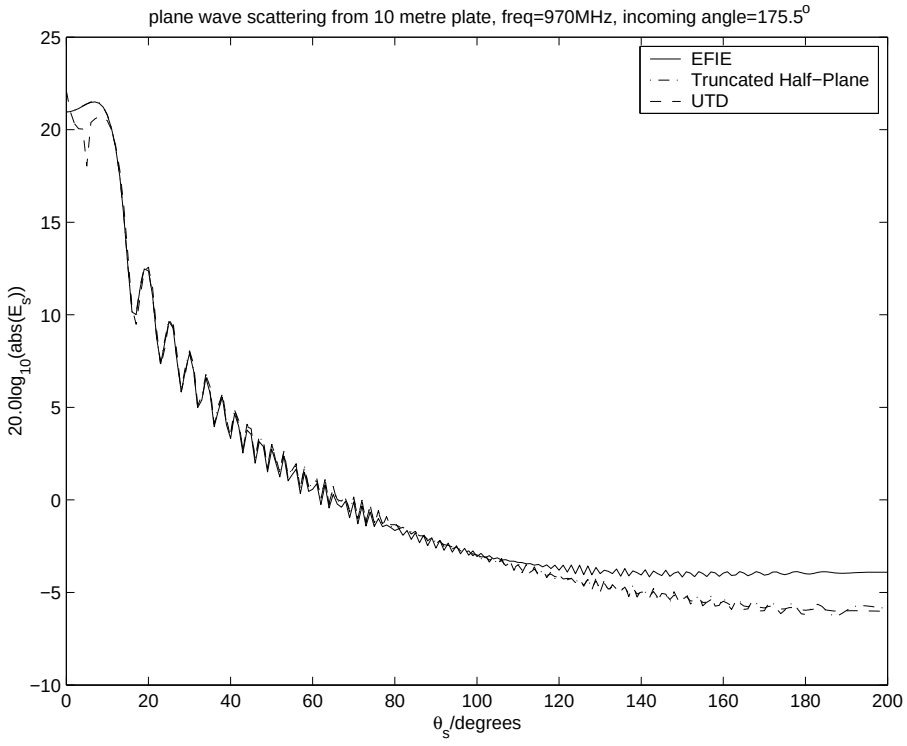

Figure 3-19: Comparison between full EFIE solution, Truncated half-plane method, and UTD.

ray-tracing in the problem area. There is not a perfect match but when plotting the result in decibels the error between the MoM and THP is very small.

This result was obtained by modifying equation (3.51) to change the incident planewave into a Hertzian dipole, also the scattered field points are not far field points, so these have to be expressed explicitly. So the formula used to obtain the point source result is:

$$\mathbf{E}_s^{PS}(\rho, s) \quad = \quad -\frac{jk\eta I_o l}{4\pi\rho_o} e^{-jk\rho_o} \sin\theta_i \mathbf{E}_s(\theta_i, \theta_s) \frac{e^{-jks}}{s} \tag{3.53}$$

where the fields produced by a half-wave Hertzian dipole with length $l = \lambda/2$ are given by

$$\mathbf{E}_i(\rho_o) \quad = \quad -\frac{jk\eta I_o l}{4\pi\rho_o} e^{-jk\rho_o} \sin\theta_i \hat{\theta} \tag{3.54}$$

and η is the impedance of free space, and $I_o = 1$ is the emitting current in the dipole.

In equation (3.53) the truncated half-plane formula is pre-multiplied by the dipole incident field and post-multiplied by the term necessary to represent the receiver point

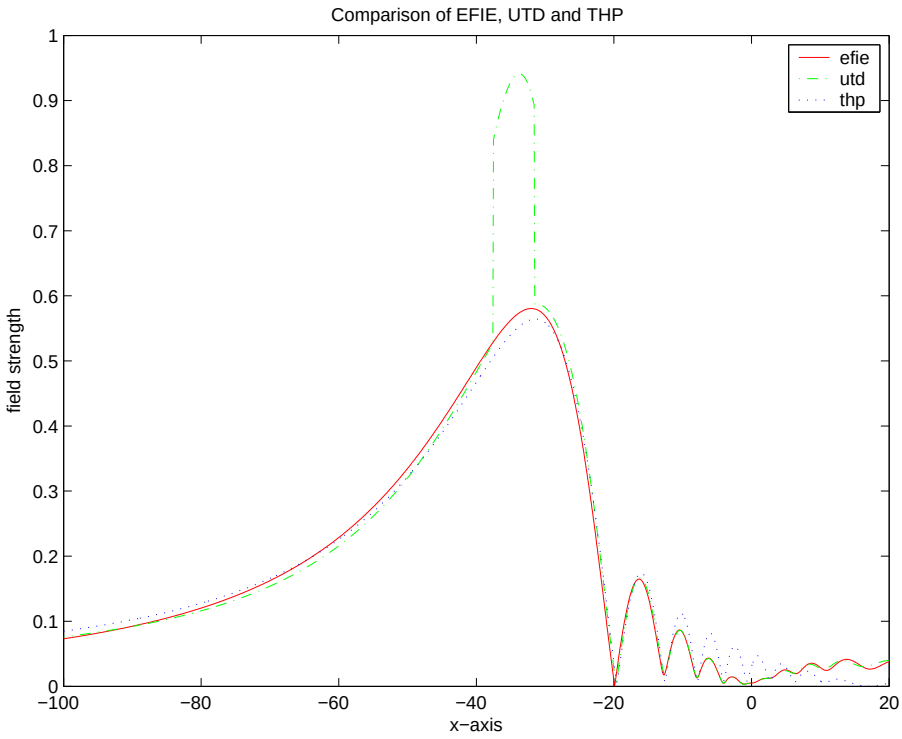

Figure 3-20: Correction to UTD obtained by THP solution

as a point-source. The angle θ_i is the angle made from the source to the centre of the plate ρ_o and the x-axis. θ_s is the the angle made from the centre point ρ_o to the scattered field point and the x-axis. As seen in Figure 3-16 the area between the turning points of the diffracted field from side A and side C is the area that has to be corrected in the UTD result. This is easily achieved by replacing the result with the THP result in the problem region as indicated by Figure 3-20.

3.8 Conclusions

The formulation of Burnside for internal reflections although reasonable and simple to calculate presupposes that all internal reflections in a slab originate from a number of planewaves each entering a dielectric slab at the same angle of incidence and arriving eventually at a receiver point outside the slab. Although this may be exactly correct for planewaves the emitting source is better described by a line source or point source in practice. Therefore in a ray-tracing solution of the problem the angles of incidence

of each ray entering the slab are in fact different. A novel numerical solution was found to yield different results in the lossless and lossy dielectric case which should be more physically meaningful than Burnside's result. The only way to be absolutely certain that the results are better is to compare the results with an integral equation solution of the full-wave problem.

The asymptotic solution of the full-wave problem using UTD diffraction coefficient was found to be incorrect for small scattering objects such as flat plates. Small scatterers such as these occur frequently in an indoor building environment. The discrepancy is likely due to coupling effects which can be corrected at a large computational cost by Holm's[31] method. The result is greatly improved by the novel numerical technique described in this thesis and is less computationally expensive than the usual UTD coefficient since it contains only two fresnel function terms.

Chapter 4

Building an Indoor Ray-Tracing Tool

The use of ray-optical methods to provide ray-paths in recent planning tool is well explained in the literature. There are three main varieties known as ray-tracing, ray-launching and beam-forming techniques. Ray-tracing seems to be the most commonly implemented form of ray-optical approach because it can give exact ray-paths between a source and receiver. Ray-launching on the otherhand relies on a spectrum of rays leaving the transmitter and arriving close to or at the receiver. The technique usually involves some sort of geodesic sphere theory. Beam forming is commonly implemented because the user of the planning tool wishes to calculate point-to-multipoint path-loss values, that is transmitter to many receivers. Within the communications group at Trinity College O'Brien, Kenny[65] worked on a point-to-multipoint ray-tracing code using a 2D beam-forming technique.

A large number of papers exist on the planning and design of indoor wireless networks such as in CINDOOR[81], Stola[76], Inanoglu[32] to name but a few.

In this thesis we consider a ray-tracing implementation containing a preassigned maximum order of reflection paths and up to one diffraction included in that path. Most ray-tracing solutions pre-compute or use some sort of visibility algorithm to ascertain information about the connectivity of the building. By visibility we mean that a point in space is visible if it is in front of some obstacle whilst it is considered

to be invisible if behind an obstacle. Using a visibility algorithm makes it easy to determine transmission points in front of an observation points, and reflection points around an observation point. The visibility algorithm is one of the most important issues in this new ray-tracing tool, because it determines the speed of the optimisation algorithm. More will be said about this now in the next section.

4.1 Building Storage Using Convex Spaces

The way in which a building geometry is stored determines how quickly one can extract visibility information. We need the visibility algorithm to determine the position of diffraction edges. A lot of planning tools use a drawing exchange format to store building geometries generated by Autodesk^{TM}. These geometrical constructions do present themselves in a way that is manipulable by a visibility algorithm, but it will be shown here that using a different arrangement of the building apriori, gives a naturally more reliable algorithm.

Since ray-tracing involves connecting a point in space to another point, it is natural to split the building into a series of convex spaces (six faced polyhedra). A convex space has the property that a line drawn through it will intersect at most two points on the boundary of a six faced polyhedron (see Figure 4-1). If a building is stored as a collection of convex spaces, it is possible to navigate from one point to another across many convex spaces very quickly. This will form the visibility algorithm for our ray-tracing. Assuming the building can be completely described by a set of convex spaces, the connections between each convex space need only be calculated once. This information is then stored away. The buildings described in this thesis were modelled as convex spaces and were input by data entry into a computer. It is intended in the future that the building could be converted into convex spaces using an automated process taking drawing exchange format (DXF) files directly from AutoCAD and analysing the facet information to generate each convex space. Storing visibility information for reuse is not a new idea, it has been used in ray-tracing algorithms for years [10]. A more complicated but similar algorithm to the one presented here was presented by Yun [86].

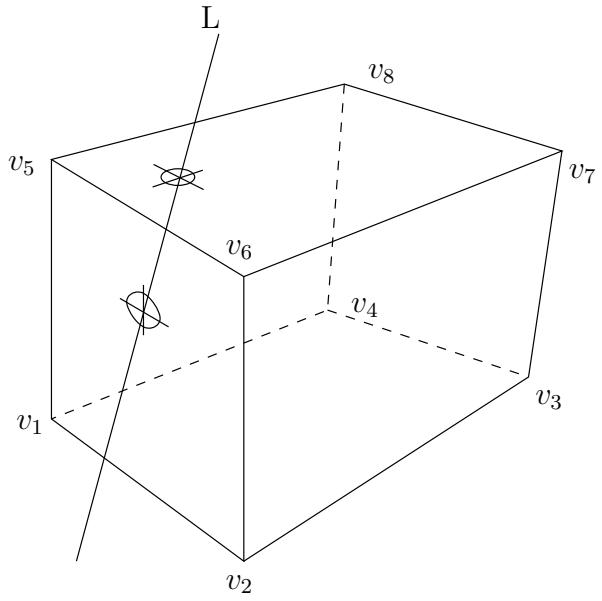

Figure 4-1: A convex space intersected by a line L.

Complicated building geometries including L-shaped rooms and torus shapes may be split into a discrete number of convex spaces (see Figure 4-2).

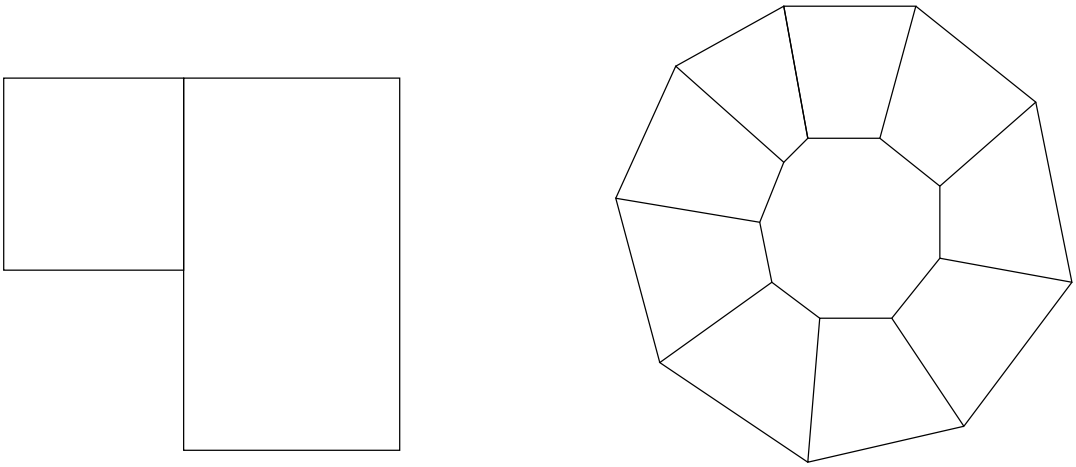

Figure 4-2: An L-shaped region seen from above and torus shaped region splitting into convex spaces.

Each convex space has six boundaries $\{B_j\}_{j=1}^{6}$, each of which is described by four vertices $\{v_i\}_{i=1}^{4}$ or by the equation of a plane. A useful numbering system for the boundaries is defined such that for two convex spaces C_i and C_j touching one another, if C_i is connected to C_j by boundary B_k, then C_j is connected to convex space C_i by

boundary B_{7-k} (see Figure 4-3).

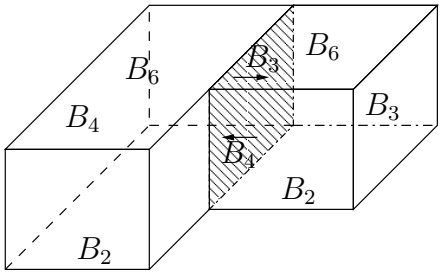

Figure 4-3: Two convex spaces connected at boundaries B_3 and B_4.

A building consists of filled or free convex spaces. By free convex space we mean that the convex space is assumed to contain free space. Filled convex spaces can be lossless or lossy dielectrics. If we want them to be impermeable then we define them to be perfect electric conductors.

A building contains floors and stories containing filled or free convex spaces. Stories contain rooms, and rooms contain free convex spaces (see Figure 4-4). Stories are sandwiched between floors. A diagram showing the connections is presented in Figure 4-5. Walls, interior walls, exterior walls and doors are all filled convex spaces which may contain zero volume.

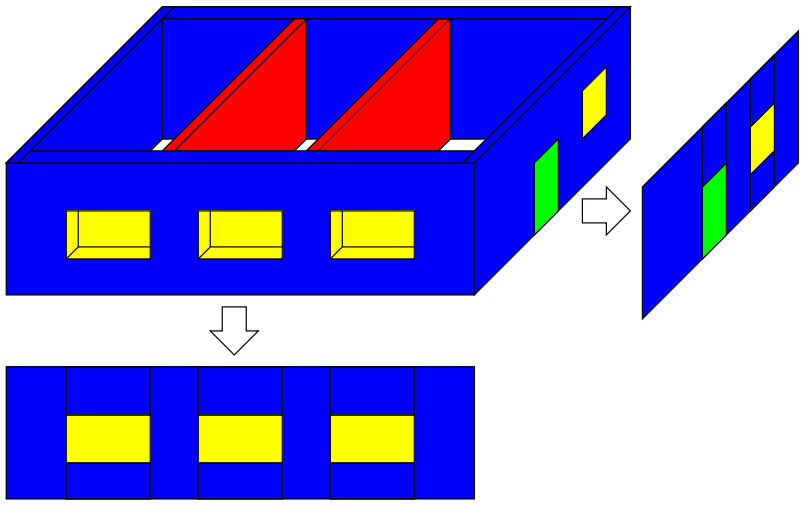

Figure 4-4: A building is made up of floors, stories, rooms and convex spaces.

A floor may contain apertures which are free convex spaces, to model lift shafts or stairwells. Doors and windows may have different depths when compared with the

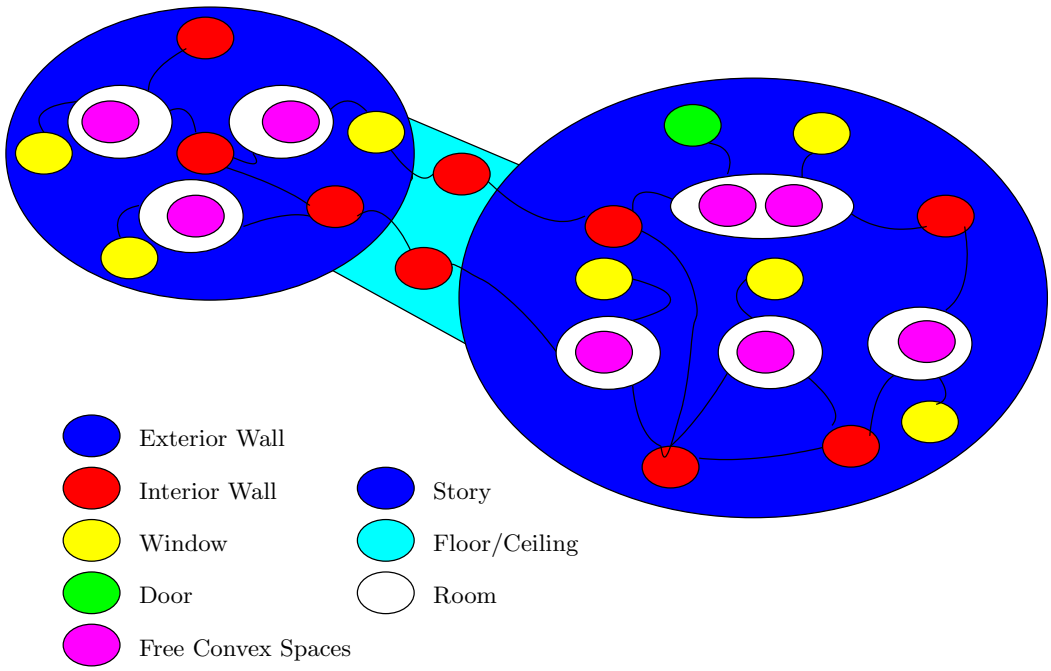

Figure 4-5: A schematic representation of a hierarchical description of a building.

surrounding walls to give more realistic modelling.

The way we obtain the connectivity information is by finding the equation of planes of the boundaries of our current convex space of interest, and determining which other convex spaces have boundaries that lie on the same plane. Then we determine whether a point on this same plane is contained in the boundary of the current boundary of interest. Doing this for the whole building will give us all the connections we need, and this is the information that need only be calculated once and stored away. If for some reason a new convex space is added to the building, the software will automatically recreate the inter-connectivity information to allow for the change.

4.2 Determining Reflection and Transmission Points

The steps required to determine the reflection and transmission points in a building without diffractions are:

1. Determine all images of a transmitter $T_x \equiv T_x(x, y, z)$ using the method of

images.

2. Determine the valid reflection points by tracing back from the receiver point to the image of a transmitter.

3. Pick out the transmission points along the way and store this information also.

We will now present each step of the algorithm in turn.

4.2.1 Point Method of Images

The method of images is used to determine the positions of the transmitter images in the building. This is a method widely used because it determines ray paths up to a given order. Ray launching could also be used but we will not be looking at that here. Because we have now described the building as a number of convex spaces, it is possible to use our compact storage of the building to speed up the method of images process.

The algorithm is defined as follows:

1. A set of reflective planes about the transmitter must be determined. We note that reflection points lie on the boundary of filled convex spaces, so we need not check the connections with free convexs inside rooms and apertures of floors. From each of the six boundaries of these filled convex spaces we determine a unique set of equations of reflection planes of the form $Ax + By + Cz = D$, oriented so that the point $\hat{n} = (A, B, C)$ defines an outward normal to the plane.

2. Once the reflection planes are obtained, the transmitter T_x is defined to be the 0^{th} order reflection point $T_x^{(0)}$ in a tree of images.

3. Determine if the transmitter $T_x^{(0)}$ is on the positive side of each reflective plane. By this we mean that the we test the condition $d = (T_x^{(0)} - v) \cdot \hat{n} > 0$ where v is some point on the reflective plane. If $d > 0$ then reflect the image point $T_x^{(0)}$ in the plane to obtain a new image point ${T_x}^{(1)}$. This operation is performed for all reflective planes until all first order images are created.

4. From a first order image $T_x{}^{(1)}$ second order images and higher order images are obtained by repeating the procedure in the previous step.

   The image tree is created in such a way that a node in the $(n+1)^{th}$ level of the tree can access the node in the n^{th} level of the tree. We do not need to store the information about the reflective planes that generated the image, because it is a simple matter to obtain the midpoint between the n^{th} and $(n+1)^{th}$ points and then obtain the reflective plane (see Figure 4-6).

4.2.2 Determining the Reflection Points in a Ray-Path

There are a number of algorithms which are required before finding the reflection points in a building. One important algorithm is finding the convex space containing the receiver or transmitter point of interest. We first know that the observation point is not inside a wall, so it must be in a free convex space. In Figure 4-5 we see that the free convex spaces are contained inside stories, so it is easy to determine which story the point is inside, and then it is a simple matter of finding which free convex space the point is contained in, by traversing through each free convex space.

The algorithm for determining the reflection points in a ray-path of order n for a specific branch of the image tree is now described as follows:

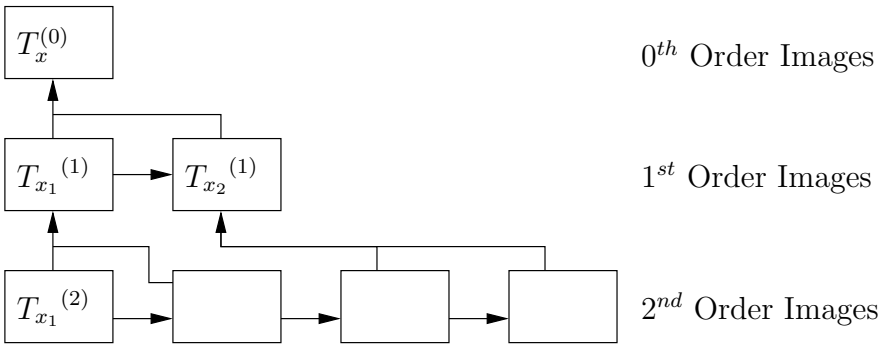

Figure 4-6: The image points generated by method of images.

1. First determine the free convex space where the receiver and transmitter lies using the algorithm just mentioned above. The receiver is pushed onto a stack

of points which will form a ray-path list. The receiver is also indicated by a key (see Figure 4-7).

2. Create a line segment from the receiver point to the n^{th} order image in the image tree.

3. We first intersect the line with the current convex space to give a point of contact P into the next free or filled convex space. If the point of contact P is on boundary b_i then we know that it is on the boundary of b_{6-i} in the adjacent convex space. We have already stated that all boundaries are connected to adjacent boundaries so it is easy to determine which adjacent convex space contains the point of contact.

4. If the point of contact P falls on a filled convex space then we need to update our transmission count. If we pass through too many filled spaces, that is, a number great than the maximum that we wish to allow, then we say that the ray-path is invalid and therefore we stop at this point.

5. If the point of contact P is on the positive side of the line, that is, $d = (P - v) \cdot \hat{n} > 0$ where v is some point on the reflective plane and n is the outward normal from the plane, we know that we must travel until $d = 0$. If we find that $d < 0$ then we have not found a point on the reflective plane, and therefore the ray-path is invalid, and we stop at this point.

6. The line segment can intersect at most two points on a convex space at P and Q. We know P already, so it is easy to determine Q on the opposite side of the convex space. We then continue our procedure as in the two steps above until we determine the point of reflection. Once we obtain this point of reflection we push it onto the ray-path stack, and this becomes our new start point for the algorithm. From this point we repeat the algorithm except that we use the previous image point to determine our line segment.

7. Repeat the process until no image points remain.

Points	Key
T_x	TRANSMITTER
P_1	REFLECTION
P_2	TRANSMISSION
P_3	TRANSMISSION
P_4	REFLECTION
R_x	RECEIVER

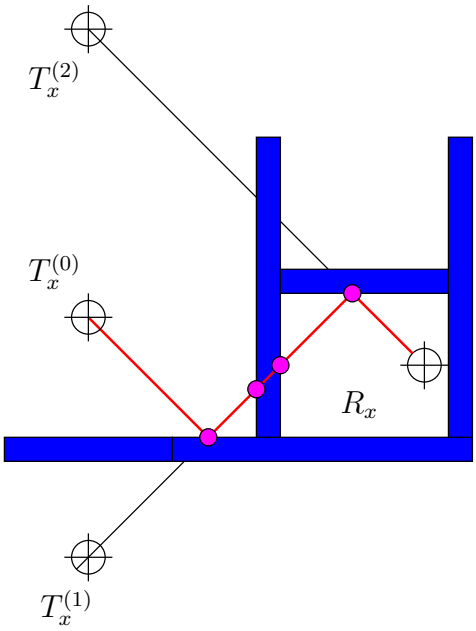

Figure 4-7: The reflection and transmission points generated by the method of images.

4.3 Finding Points of Diffraction

The algorithm for finding the valid diffraction points or in the case of corner diffraction finding virtual diffraction points, is described as follows:

1. Determine all diffraction edges in the building.
2. Sort the diffraction edges and images of the diffraction edges in a diffraction tree, created using the method of images.
3. Find the n^{th} order ray including one diffraction using the diffraction tree and reflection tree.

Each of the steps in the algorithm are covered in the next sections.

4.3.1 Determining Diffraction Edges of Filled Convex Spaces

The algorithm for finding all valid diffracting edges in an indoor environment incorporating the convex space methodology is defined as follows:

1. When using diffraction algorithms within a building we must first define all valid diffraction edges. Only filled convex spaces can generate a valid diffraction edge.

An edge is contained on two boundaries B_i and B_j of a convex space such that we obtain 12 permutations of the couple (i, j):

$$(1,2),(1,3),(1,4),(1,5)$$
$$(2,3),(3,4),(4,5),(5,2)$$
$$(6,2),(6,3),(6,4),(6,5)$$

2. If we extract a list A_i of the free convex spaces adjacent to B_i and a list A_j of the free convex spaces adjacent to B_j then for each convex space C_m in A_i and each convex space C_n in A_j we check to see if an adjacent boundary to C_m is in A_j or a adjacent boundary to C_n is in A_i. We say that this boundary is part of convex space C_k. Assuming there isn't a boundary, we have no valid diffraction edge, but assuming there is we need to do some further checks.

3. Intersecting the edge of C_k between B_i and B_j with boundary B_{6-j} of C_m and B_{6-j} of C_n we form a diffracting edge.

4. If B_{6-i} in C_m and B_{6-j} in C_n are coplanar then we have no valid diffracting edge, otherwise we do have a valid diffracting edge.

4.3.2 Creating a Method of Images Tree for Diffractions

If we describe the diffraction edge by its endpoints, then the method of images is identical to the method of images described for a point except that both points are reflected in reflective planes instead of one point.

The tree will contain many diffraction edges at the 0^{th} order layer, and will have images of the diffraction edges when reflected in planes at the 1^{st} layer (see Figure 4-8).

4.3.3 Calculating the Diffraction Point and Ray-Path

We will see that for an m^{th} order ray with one diffraction point positioned as n^{th} order term of the list, that there are $m-n-1$ reflections before the diffraction point, and there are n reflections from the diffraction point to the receiver point.

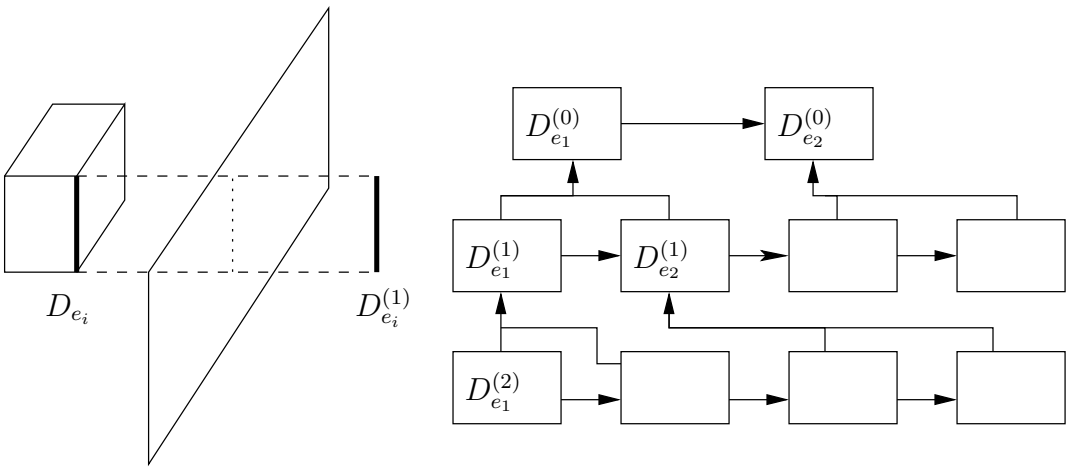

Figure 4-8: The image points generated by method of images of diffraction points.

Figure 4-9 shows how a 4^{th} order ray-path is decomposed into a path from $T_x^{(m-n-1)} = T_x^{(2)}$ to the diffraction point $P_{m-n} = P_{4-1} = P_3$ on the diffraction edge $D_e = [D_e^1, D_e^2]$. There is a path generated then from $D_e^{(1)} = [D_e^{1(1)}, D_e^{2(1)}]$ to the receiver point R_x.

Before calculating the ray path we need to describe in more detail how the point of diffraction P is found given that the ray-path contains $(m-n-1)$ reflections, one diffraction and n reflections:

1. Calculate the lengths $L_1 = (T_x^{(m-n-1)} - D_e^1) \times \hat{v}_1$ and $L_2 = (R_x^{(m-n-1)} - D_e^{2(n)}) \times \hat{v}_2$ using shortest distance formula to D_e and $D_e^{(n)}$ respectively (see Figure 4-10).

2. Construct the distances $d_1 = (T_x^{(m-n-1)} - D_e^1) \cdot \hat{v}_1$ and $d_2 = (R_x - D_e^{2(n)}) \cdot \hat{v}_2$ which in turn gives the points of contact $A_d = D_e^1 + \hat{v}_1 d_1$ and $B_d = D_e^{1(n)} + \hat{v}_2 d_2$.

3. Define the length $d = d_2 - d_1$.

4. Using the ratio $L_1 : L_2$ it is possible to locate P using the formula: $P = A_d + \hat{v}_1 \frac{L_1 d}{L_1 + L_2}$.

Now, once the diffraction point is found we are in a position to describe the method for finding the ray path. This algorithm will again be computationally fast because of the convex space description of the building. Another thing that makes this algorithm fast is the continual reuse of the diffraction tree. It is never a good

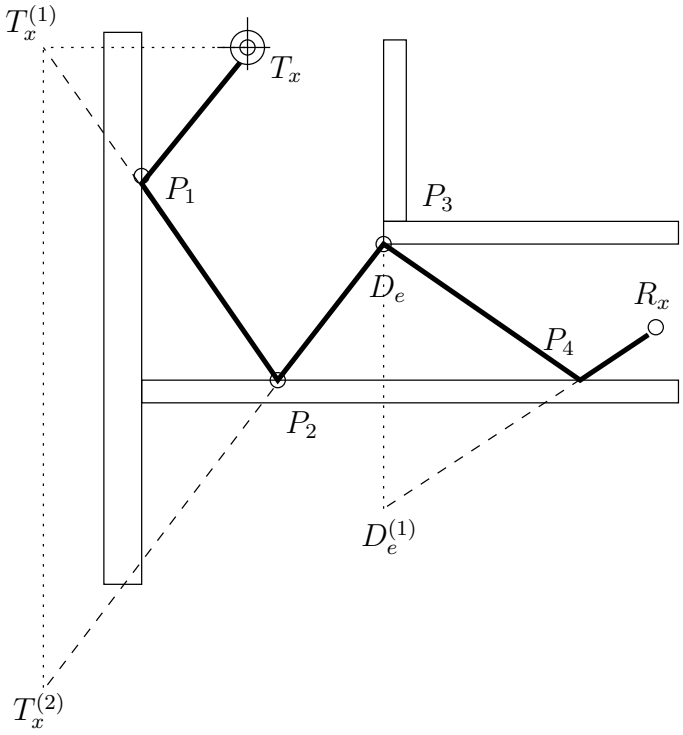

Figure 4-9: The ray path for a 4^{th} order ray including one diffraction point at P_3.

idea to build the diffraction tree into the point image tree although some authors have done this, instead it is better to know exactly what branch of the diffraction tree (n^{th}) needs to be extracted given that we know the order of reflection ($m-n-1$) before the diffraction point. This efficient method was described by Schettino[73] and many other authors. If the diffraction tree is inserted inside the point image tree then we end up with many multiple copies of the tree which is very inefficient.

The method for extracting ray-paths is described as follows:

1. Let the receiver R_x be the $(m+1)^{th}$ image point.

2. Looping over all n^{th} order diffraction edges of the diffraction tree, extract a single term $D_e^{(n)}$ and also determine its generating edge D_e. The generating edge is found by travelling back up to the 0^{th} order level of the diffraction tree (see Figure 4-8).

3. Extract a transmitter image of order $(m-n-1)$ and then construct the diffraction point P_{m-n} using the method described earlier in this section.

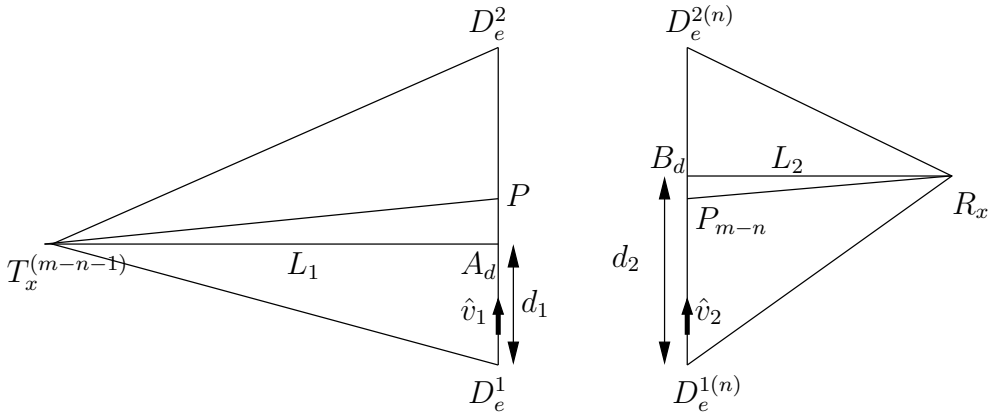

Figure 4-10: The ray path of order m unfolded with a diffraction point at the $(m-n)^{th}$ point.

4. If P_{m-n} is contained in D_e then it is a real diffraction point used with standard diffraction methods. If it is not a contained in D_e then it is still required for the corner diffraction techniques and is marked as a virtual diffraction point. Each reflection point P_{m-n+j} is constructed for all $j = 1, 2, \cdots, n$ by travelling back from the receiver point R_x to the diffraction point P_{m-n} using the algorithm in Section 4.2.2.

5. The reflection points P_j for all $j = 1, 2, \cdots, m-n-1$ are generated by travelling back from the diffraction point to the transmitter using the same algorithm in Section 4.2.2.

The construction of the double diffraction points is not so easy. In the past the method of finding the diffraction points was easily described for coplanar edges, but in practise the edges may point in any direction, especially in an indoor environment. The Newton-Raphson formula is easily applied (see Appendix A) to define an iterative solution which converges to the valid diffraction points. We did not concern ourselves with double diffraction point in this work.

4.4 Conclusions

The two dimensional convex space description of the building avoids the description of a standard visibility algorithm like that of Agelet[5] as explained by Yun[86] making a computational saving of 25% to 30%. It would be expected that this saving would also occur in a full three dimensional implementation like the one described in this thesis.

Because this algorithm avoids a conventional visibility algorithm related to the transmitter location, it is exactly what is needed to avoid computational slow downs in the optimisation procedure to be presented in Chapter 7.

The algorithm avoids any loss of ray information and in fact forms a path along which transmissions and reflections are easily found. In some ray-tracing algorithms finding the reflection points and transmission points results in a sorting algorithm having to be called to obtain the correct ordering of the transmission and reflection points along the ray-path.

The separation of the diffraction edge list tree from the reflection tree avoids repetition of the diffraction tree calculation and speeds up the algorithm as a result.

Chapter 5

Verification of Ray-Tracing and Comparison with Measurements

The correctness of any ray-path finding method needs to be tested thoroughly, especially when developing a commercial tool. Where possible a verification of the working modules written in C++ must be compared with previously generated results, or systems need to be devised to obtain another simple method of obtaining the same result. Also a comparison with real measurements is important since this verifies the validity of the assumptions made in the tool and verifies that the tool as a whole is working correctly.

5.1 Correctness of Diffraction and Reflection Ray-Paths

The diffraction method needed to be evaluated for a test case. A simple example suited to this uses a single room containing four diffraction edges yielding symmetries in the ray-path solution across the lines XX and YY (see Figure 5-1). The transmitter and receiver are set up in such a way that they always ensure symmetry. If the ray-paths are found to be anti-symmetric then it is clear that some of the paths were missing. Because there are a number of convex spaces meeting at one diffraction edge it is not such a simple matter to guarantee the correct ray-paths for the calculation.

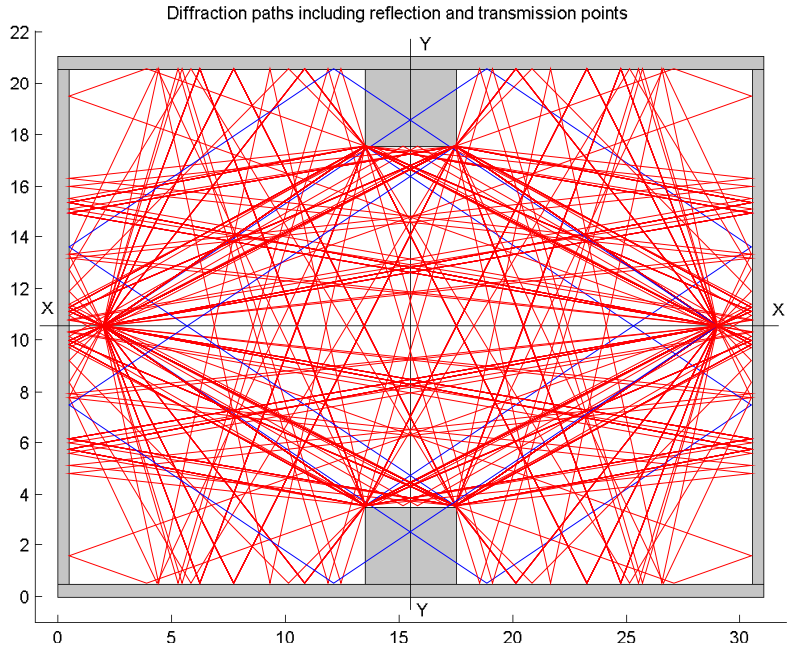

Figure 5-1: Diffraction paths mixed with reflections inside a one room building.

It was found that this test did show up errors in the Software Tool for Wireless Resource Optimisation (STIWRO) code which were easily fixed with some small case statements in our code. It turned out that when tracing a ray from the diffraction point back to the transmitter, it was important to move the starting point by a perturbation along the line to be traced so that the correct convex space containing the diffraction point was found, otherwise the algorithm starts off in the wrong convex space and can detect an extra transmission through a wall, which is incorrect.

Again setting up the one room building as for the diffraction case, the valid reflections should form a symmetric pattern through the line segments XX and YY. This is the case as can be seen in Figure 5-2.

5.2 Software Tests

A building was generated containing a total of 230 convex spaces, with 4 floors including the roof, 3 stories, with internal walls, external walls, doors, windows and 6 or 7 rooms per story. The floor contained apertures to represent stairwells. The

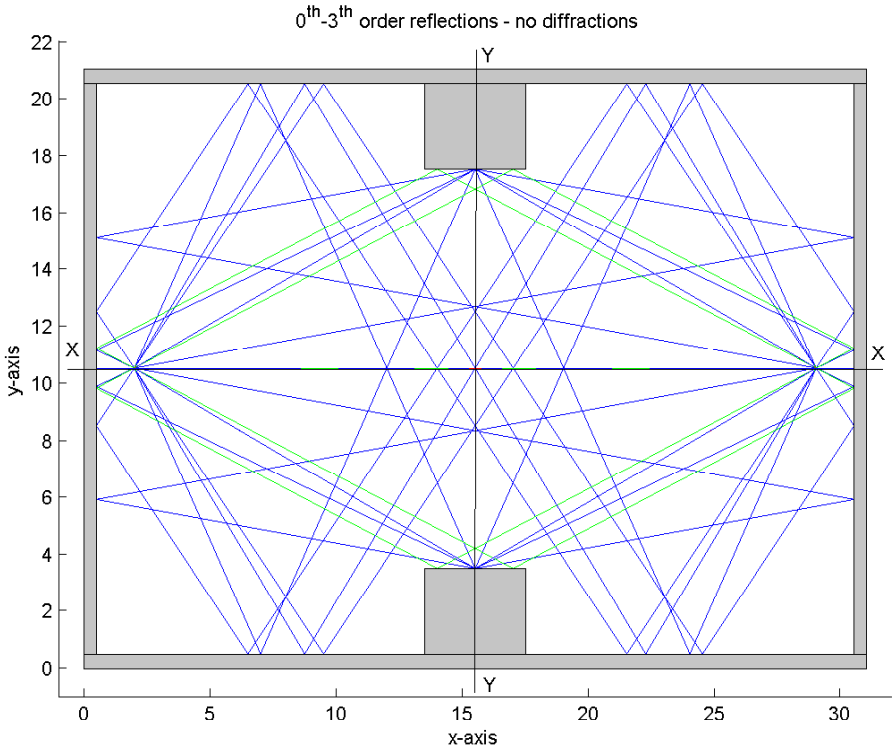

Figure 5-2: $0^{th} - 3^{rd}$ order reflections inside a one room building.

building plan can be seen in Figure 5-3. The second story contains an L-shaped room in the top right corner which must be split into two free convex spaces. The third story contains a corridor (room) which must be split into two or three convex spaces depending on the way it which it is split. For the examples that follow, the doors of each room are assumed to be closed. All plots in this section were easily generated using Matlab functions once the building was stored as convex spaces.

The constitutive parameters for the different dielectric materials making up the building are presented in Table 5.1. Although the values are frequency dependent we will assume they are constant values for frequencies greater than 900MHz.

5.2.1 Test 1: Reflections Inside a Single Story

Presented here is a sample of the type of results that can be obtained from running the ray-tracing with reflections up to 3^{rd} order and no diffractions. For the purposes of this illustration the number of transmissions was set to be a maximum of three. If

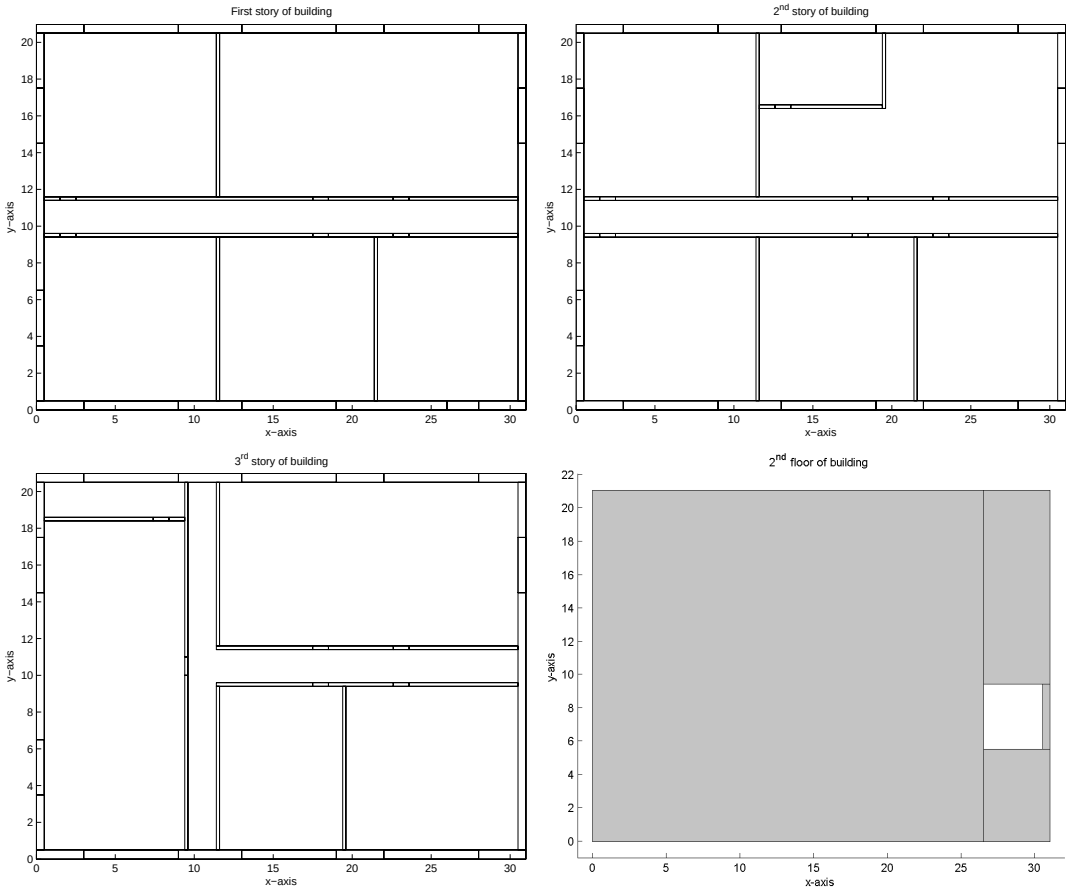

Figure 5-3: A plan view of three stories in the sample building and 2^{nd} floor.

a higher number of transmissions were specified then the number of rays would be too numerous to give a presentable plot. The transmitter is placed at location $(3, 18, 1.5)$ and the mobile terminal is placed at location $(26, 2, 1.5)$. The transmission frequency is defined to be 900MHz. All reflected rays of order zero to three are presented in Figure 5-4 along with an overlaid plan view of the first story of the building.

This plot does not display the full complexity of the ray-paths because it is shown along a two-dimensional cross section. In many cases if there are a sufficient number of transmissions allowed, the rays pass into other stories through floors and re-enter from the opposite side back into the story where the receiver lies.

Constitutive Parameters	ϵ	μ	σ
Free Convex Space	1	1	0
Exterior Walls	4.44	1	0.08
Interior Walls (guess)	4.0	1	0.04
Doors (glass, Balanis[7])	2.32	1	1.45×10^{-3}
Windows (glass)	2.32	1	1.45×10^{-3}

Table 5.1: Dielectric material properties for sample building

5.2.2 Test 2: Confirmation of Correctness of Reflected Rays

To validate the correctness of the reflected rays it was necessary to test the raytracing over an infinite flat plate (practically speaking this is is a large plate with no diffraction edges). The transmitter was placed at $(x, y, z) = (0, 0, 5)$ and assumed to be a hertzian dipole. The total field was calculated for the TM_z case. At each receiver point on a regular grid of size 30×20 metres the result was compared with the result obtained by reflecting the transmitter in the large plane, that is the geometrical optics (GO) solution. The results are shown in Figure 5-5.

It can be seen that the plots look identical for the perfect electric conducting case, which is what we would expect. In fact they are identical to 16 places of decimal, showing that all the ray-based coordinate systems and attenuation factors are working correctly.

5.2.3 Test 3: Diffractions Inside a Building Story

The transmitter is placed at location $(3, 18, 8.5)$ and the mobile terminal is placed at location $(26, 2, 8.5)$ so that we expect some diffractions from the edges of the corridor on the 3^{rd} floor of the sample building shown in Figure 5-3. As can be seen in Figure 5-6 this is the case. The order of reflections is 3, diffractions is 1 and transmissions is 3 for this plot. There is also a diffraction from an aperture that exists on the 3^{rd} floor in the room where the receiver is positioned. The 3^{rd} floor plan is identical to the 2^{nd} floor plan shown in Figure 5-3.

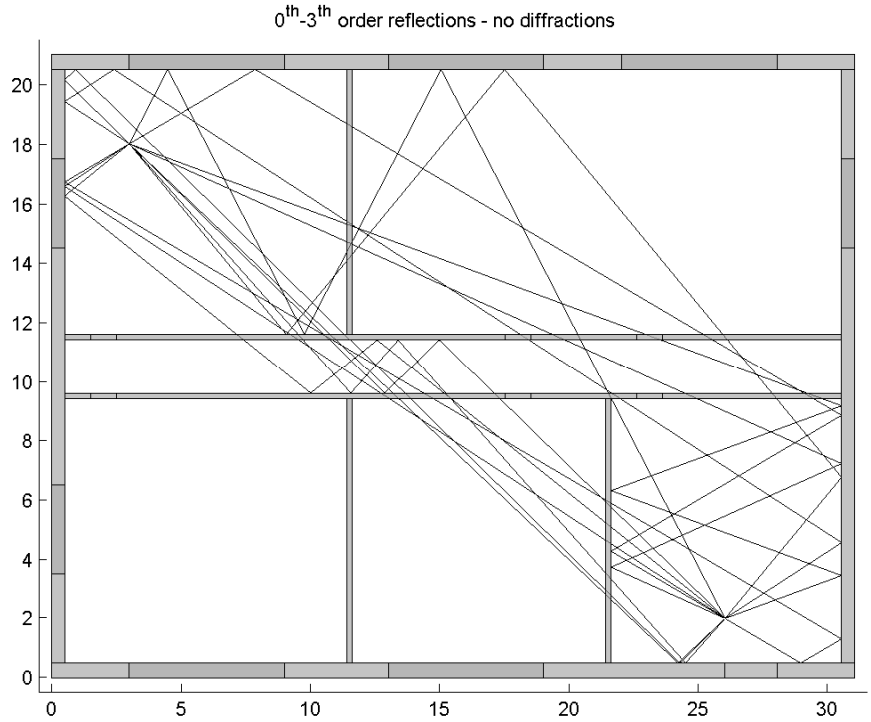

Figure 5-4: $0^{th} - 3^{rd}$ order reflections inside first story of the building.

5.2.4 Test 4: Path-Loss Grid Plot

This test assumes a regular grid between $(0.75, 0.75, 5.0)$ and $(30.75, 20.75, 5.0)$ with step size $\Delta x = 0.25$ and $\Delta y = 0.25$ leading to the path-loss computation at 9600 points covering the second story of the sample building. A frequency of 900MHz for a z-axis oriented hertzian half-wave dipole at location $(5.0, 5.0, 5.0)$ leads to the result in Figure 5-7 where the maximum number of reflections is 3, transmissions is 4, and diffractions is 1. The path-loss is plotted in decibel/metres but the building height is stretched in the z-axis, so that the story and path-loss grid can be overlaid. The results are easily interpreted showing large path-losses in areas which are heavily shadowed from the transmitter. The computational time on a 1700MHz Pentium 4 workstation was 42 minutes for all 9600 computations. The average number of valid ray paths would be of the order of 100, so that the average time for the calculation of the received total path-loss at each receiver is approximately 0.25 seconds. Some years ago an indoor ray-tracing code was developed by the group at Trinity College

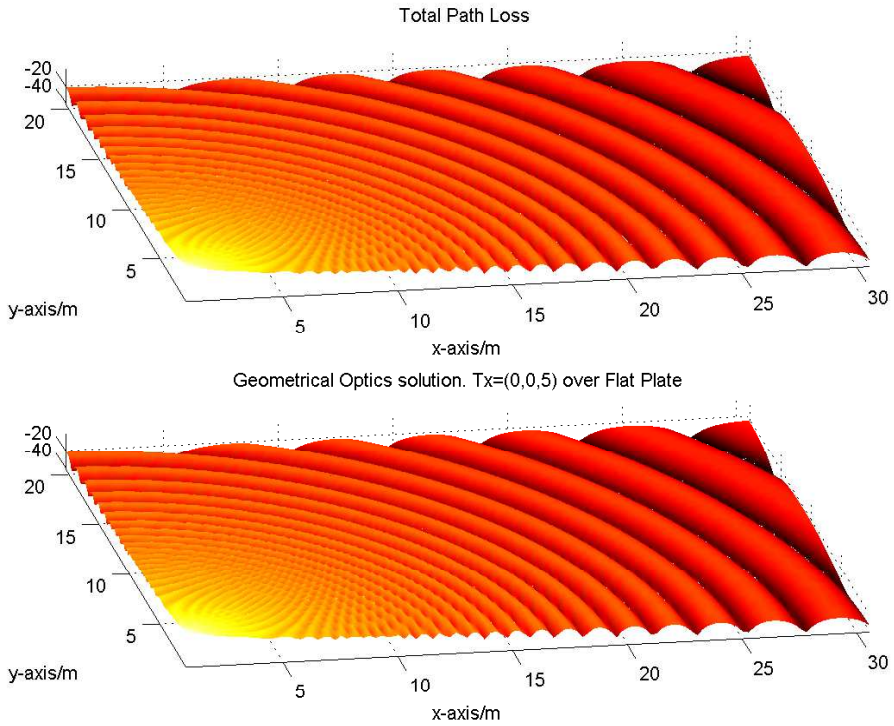

Figure 5-5: The ray-tracing result versus the geometrical optics result.

with computational times of about 40 minutes for a building with 12-15 convex spaces and 200-400 reciever points. With the increase in computing power this code would run on the Pentium 4 in about 10 minutes. Obviously the new ray-tracing code gives a far superior computation time since it contains over 200 convex spaces and 25-50 times more receiver points.

5.3 Verification of Two Measurement Sets

The communications group in the Printing House at Trinity College has at its disposal antennas, network analysers and draftsman drawings to perform its own measurement campaign. I obtained the draftsman drawing of the building and input the dimensions into the computer to form the top floor of the printing house with open or closed doors where necessary. An example of the building is shown in Figure 5-8.

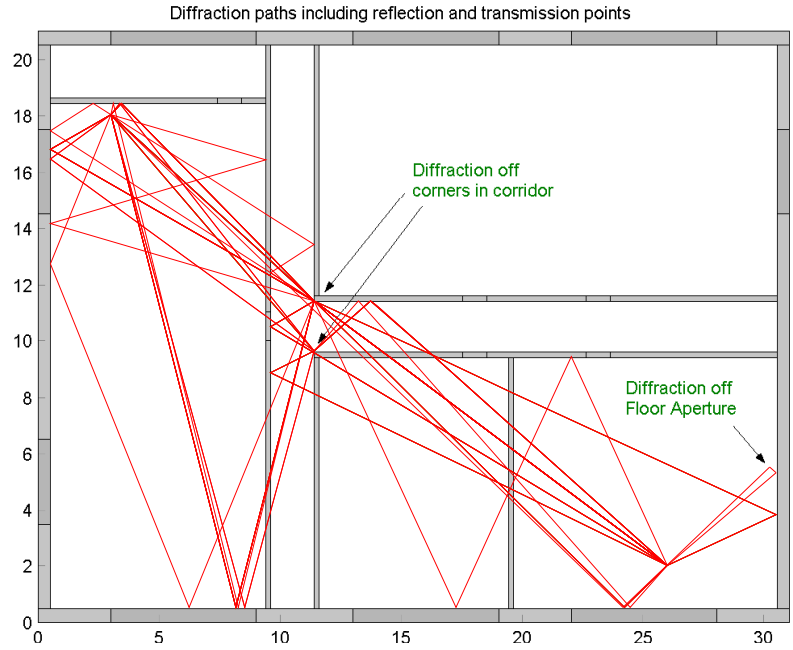

Figure 5-6: Diffraction paths mixed with reflections inside the third story of the building.

5.3.1 Measurement Set 1

A transmitter was placed in one of the rooms of the building at location $T_x = (5.468, 6.51, 1.45)$ inside the free convex space number 12 indicated in Figure 5-8. The receiver points were set up along the corridor and out into the landing area. Measurements were taken from an antenna mounted on a trolley as shown in Figure 5-9. For the first measurement set the building contained a number of open doors whilst other door are shut. All open doors are shown in Figure 5-8. The room containing the transmitter was its doors open so as to form some diffraction effects down the corridor. The transmission frequency was $1.0GHz$ and the spacing between receiver points was 1 metre for the west end of the corridor and 0.25 for the east end also shown in Figure 5-8. The shorter spacing was used to obtain a better measurement of the fluctuations in the field as it propagates in the corridor.

The measurement results along with the ray-tracing prediction are shown in Figure 5-10. Using a relative permittivity of 2.32 and conductivity of 1.45×10^{-3} the

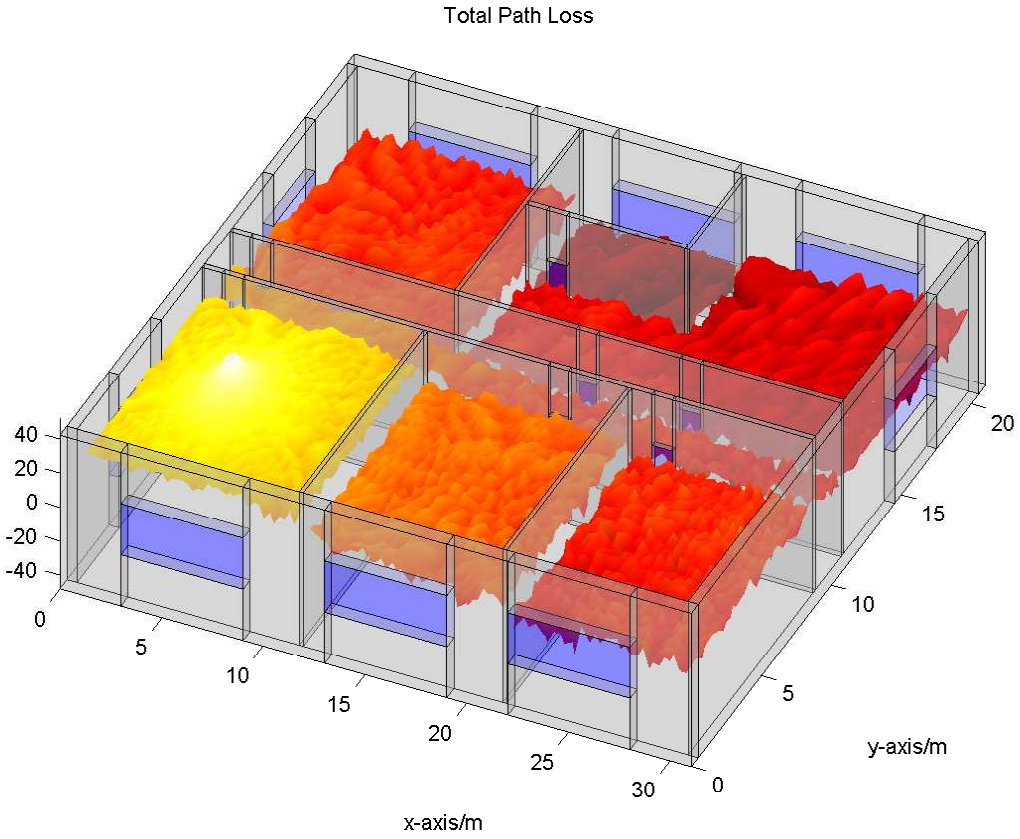

Figure 5-7: A path-loss grid generated for 9600 points on the second story of the sample building.

results agree quite well with the measurements. Changing the permittivity and conductivity gives closer agreement with the measurements, although each is a guess. The first set (indicated in red) are most likely the more realistic of the two because the permittivity and conductivity defined by Balanis[7] were assigned to the reinforced glass in the doors.

Again a ray-tracing prediction was performed with the doors closed and no doors at all on the office containing the transmitter just to show how the field can vary if the modelling of the building is incorrect. These results are shown in Figure 5-11.

5.3.2 Measurement Set 2

In the next measurement set the transmitter was placed in the corridor at position $T_x = (4.688, 4.516, 1.45)$ and the receiver is placed at the far end of the corridor in

front of some fire doors along the line $x = 14.774$ with all doors closed as shown in Figure 5-12.

The results are presented in Figure 5-13. The reference solution obtained using the ray-tracing contained up to order 3 reflections, order 4 transmissions and no diffractions. There are no diffractions anyway because all doors are closed. The solution shown in Figure 5-13 (green line) does not seem to correlate with the measurement results. To see if there was cancellation of the signal due to multi-path we ran the same ray-trace except that the maximum number of reflections was 1, shown by the red line in the plot. The results are much more similar to the measurements. The discrepancy is likely due to phase cancellation, building error or wrong complex permittivity for the walls and doors. To get an average value of the path-loss at each point a mean of a random walk can be used. This mean value will not be explained in detail here, although it is explained in great detail in Chapter 7. The results for the random walk mean with orders of reflection less than or equal to 1 give a path-loss value thats varies very little across the width of the corridor as shown by the blue line. This value is a little below the mean of the measurement results. It would seem obvious that increasing the order of reflections should increase this mean, and this was found to be the case as shown by the black line when using reflection up to order 3 with the random walk mean. The values are very close to the mean of the measurement values which is what we would have expected.

5.4 Conclusions

The simulations of the ray-tracing against real measurement sets were found to give good agreement without adding to or augmenting the simulation results.

Although the results are good it is possible to do better. The only way to improve on the results is to get very accurate positions of the wall, doors and windows in the building and to define the complex permittivity very accurately using a network analyser or some other equipment that will provide the true values.

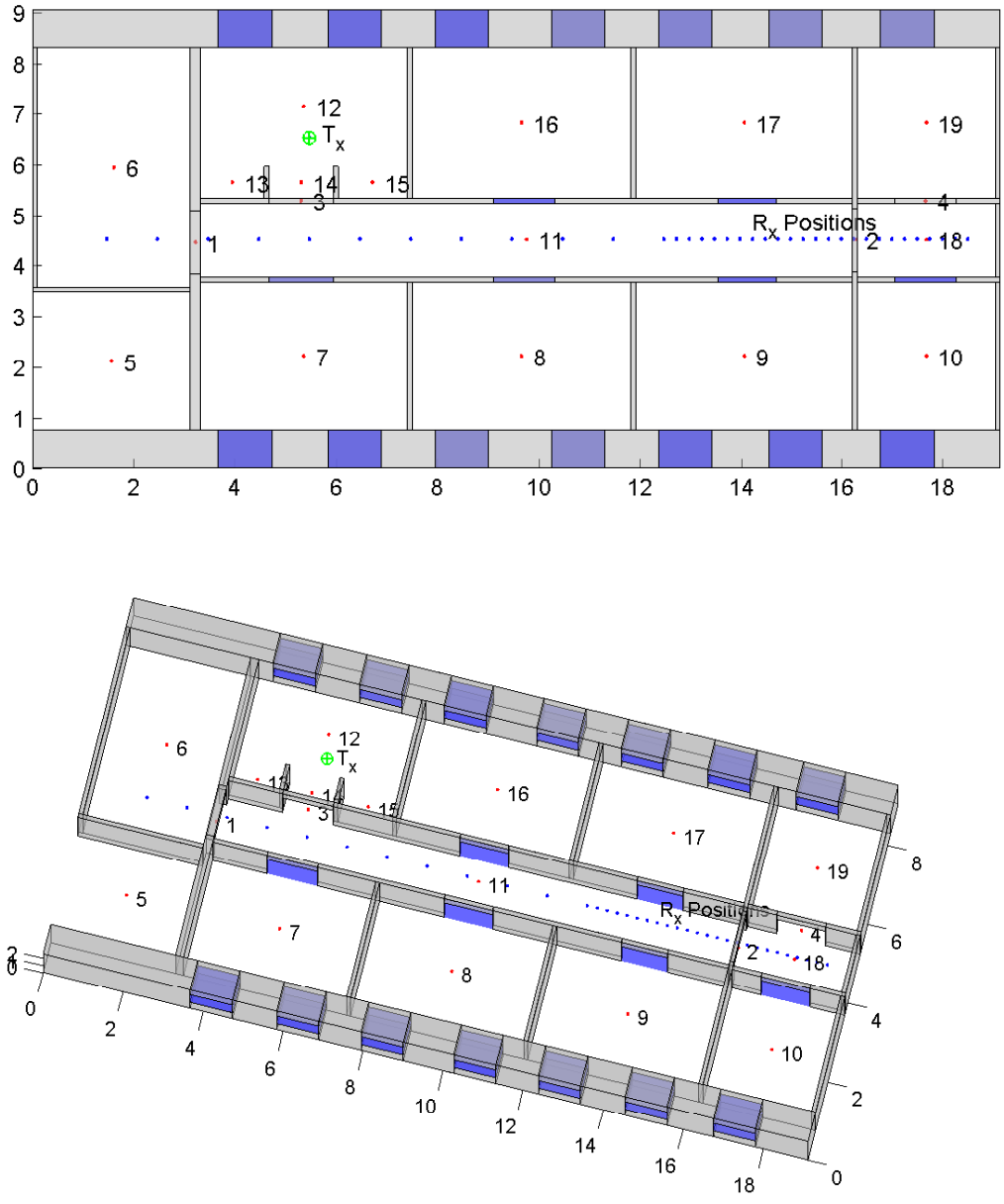

Figure 5-8: A three-dimensional view of the top floor of the Printing House at TCD.

Figure 5-9: A trolley with a half-wave dipole antenna set up to measure incoming signals from another antenna.

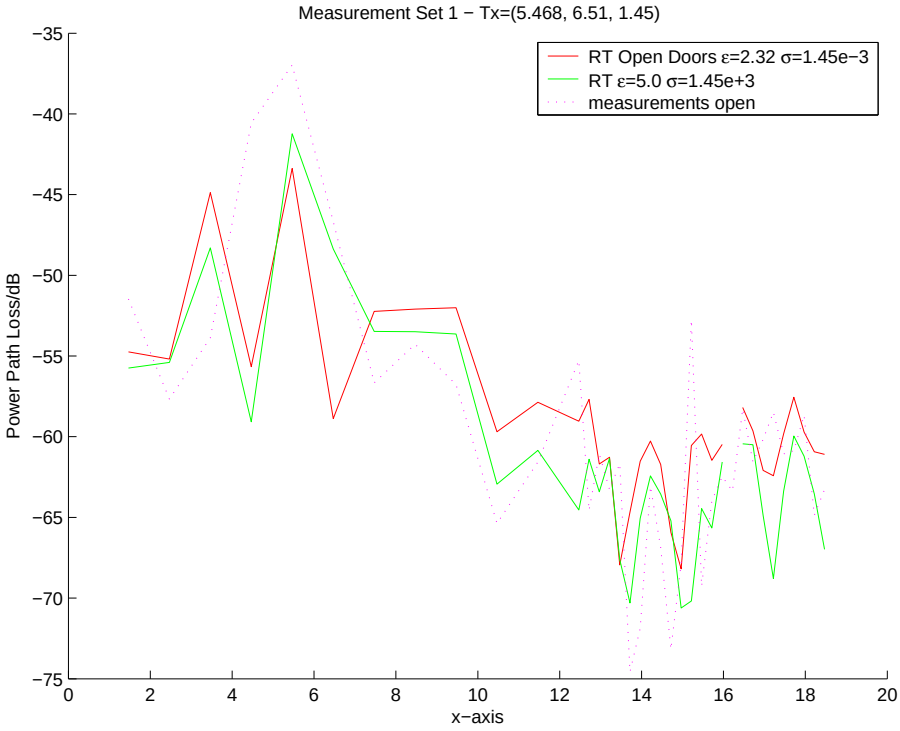

Figure 5-10: Measurements set in the corridor and overlaid ray-tracing predictions.

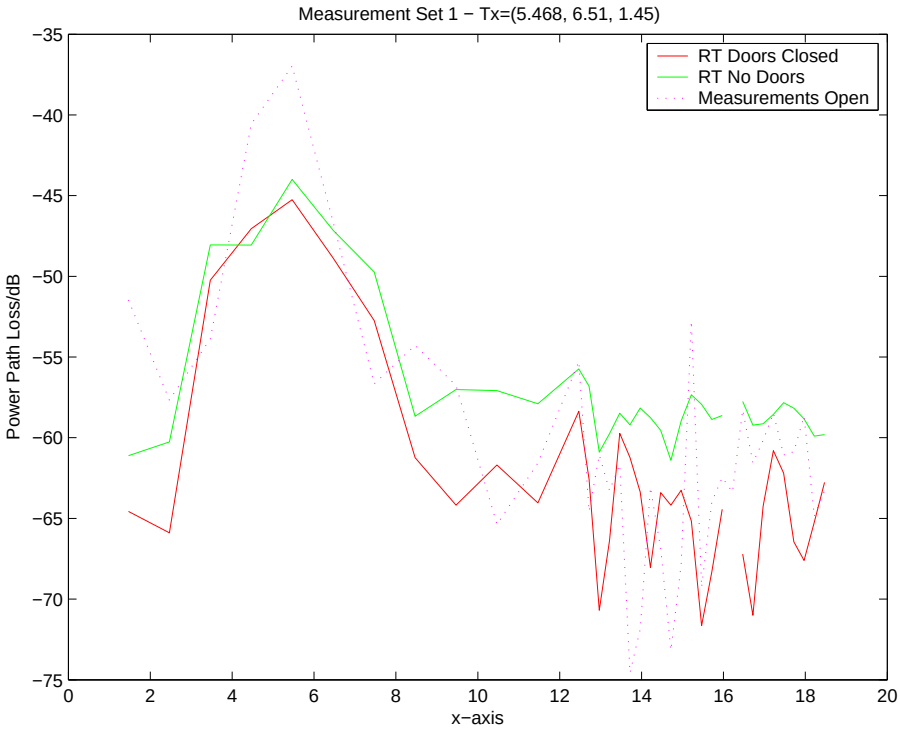

Figure 5-11: Measurements set compared with ray-tracing results obtained from an incorrectly modelled building.

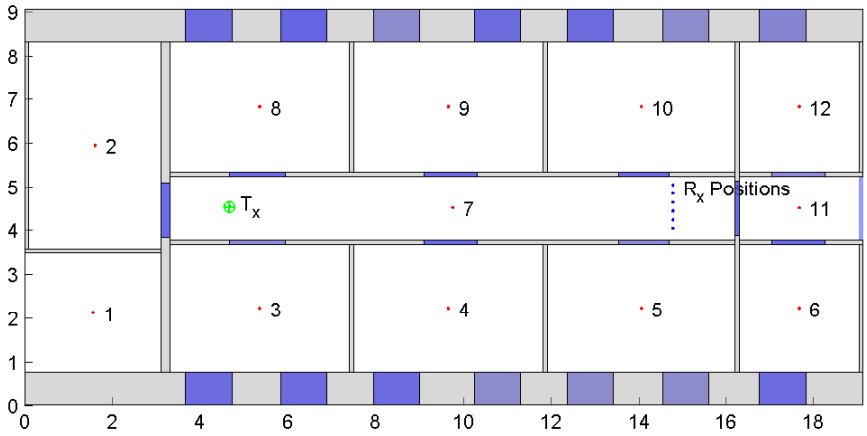

Figure 5-12: A plan view of the top floor of the Printing House at TCD with all doors closed.

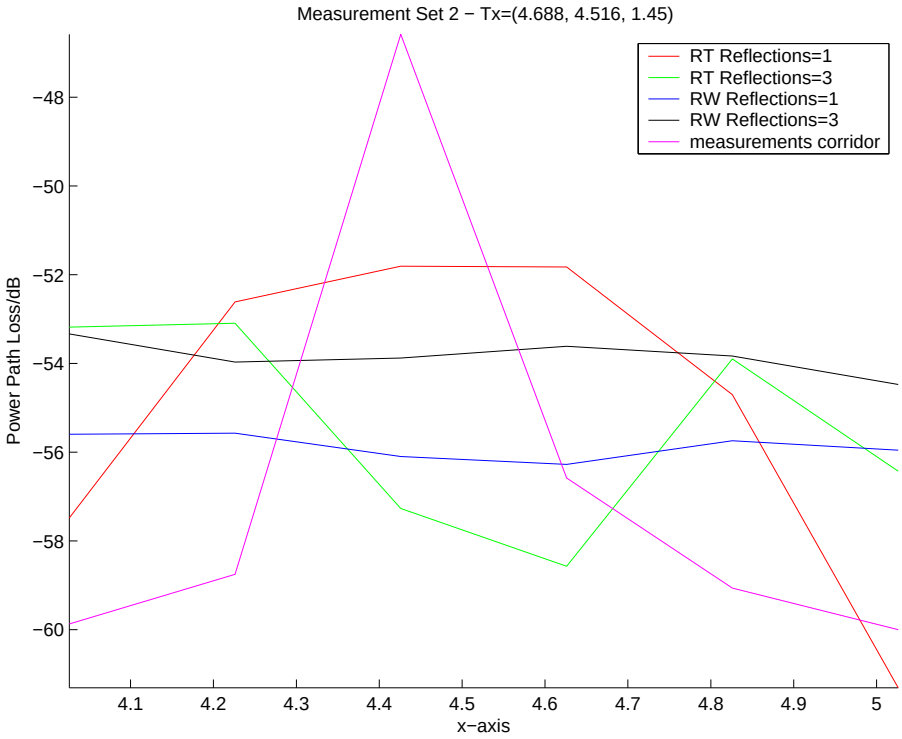

Figure 5-13: A plan view of the top floor of the Printing House at TCD with all doors closed.

Chapter 6

Convex and Non-Linear Optimisation Methods

The optimisation of a system depends on many issues. The nature of the function to be optimised is one issue and the type of constraints is another. A function to be optimised subject to some constraints results in what can be described as a linear or non-linear programming problem. Much of the background on convex problems or linear programming problems is covered by Boyd [12]. The method for solution of a programming problem is usually sought by a path-following method. These methods take an initial solution (sometimes a guess) for the unknowns in the problem, and iterate by following a path to the optimal solution. Such methods are well understood. For a very good overview of path-following methods consult Gonzaga[27].

Optimisation methods were known to be slow to solve when using primitive methods such as the simplex method, but Karmarkar's Algorithm [4] was able to achieve much faster orders of complexity for solving linear programming problems.

In the case of path-following techniques using steepest descent methods such as the conjugate gradient method, many authors such as Powell [67] use restart techniques to converge to a solution faster. What now follows is a brief overview of convex problems and an iterative technique to find the solution of a constrained convex optimisation problem.

6.1 Quick Overview of Convexity

Given a set $C \in R^n$ with any two points x_1 and x_2 in C, the space is said to be convex if the following holds

$$y = \theta x_1 + (1-\theta)x_2 \tag{6.1}$$

where y is always contained in C, and $0 \leq \theta \leq 1$. It just so happens that the convex space idea used in Chapter 4 is very much related to the convex optimisation formulation.

In the case of a function $f(x)$, the function is said to be convex if for any $x_1, x_2 \in R^n$ and λ is a scalar such that $0 \leq \lambda \leq 1$ the following identity must hold:

$$f(\lambda x_1 + (1-\lambda)x_2) \leq \lambda f(x_1) + (1-\lambda)f(x_2) \tag{6.2}$$

If a function or space can be split into domains that contain a finite number of convex functions or spaces then the function or space is said to be quasi-convex.

The terms quasi-convex and convex are well explained in Boyd[12]. If a space is neither quasi-convex or convex then it is usually a non-linear problem, or can be cast into some form of convex problem by a change of variables. For instance a fractional programming problem can sometimes be cast as a linear programming problem by changing some variables as explained by Boyd. In the case of a particular non-linear and non-convex problem Kandukuri and Boyd[50] showed that the problem could be cast as a geometrical programming problem.

6.2 Convex Optimisation Techniques

We define some notation for a convex optimisation problem as follows:

$$\begin{array}{ll} \text{minimize} & f_0(x) \\ \text{subject to} & f_i(x) \leq 0,\ i = 1, 2, \cdots, m \\ & h_i(x) = 0,\ i = 1, 2, \cdots, p \end{array} \tag{6.3}$$

where the function $f_0 : R^n \rightarrow R$ is the function to be optimised known as the objective function or cost function and $x \in R^n$ is the optimisation variable. The

functions $f_i(x)$ are the inequality constraint functions and $h_i(x)$ are the equality constraint functions.

The set of points for which the objective function is defined is called the domain D of the optimisation problem defined as:

$$D = \bigcap_{i=0}^{m} \text{dom } f_i \cap \bigcap_{j=1}^{p} \text{dom } h_j \tag{6.4}$$

A point $x \in D$ is feasible if it satisfies all the constraints. We want to find the optimal value of x usually represented by x^*. If it can be obtained then the problem is described as solvable. If x^* can only be obtained to within an error ϵ, then the solution is described as ϵ-suboptimal.

A simple example to illustrate convexity follows. Suppose we have 5 constraints each of the form $f_i = a_i x + b_i$. These are sometimes known as hyperplanes. If the intersection of all the hyperplanes form a polygon then they form a convex space since any point is connected to any other point in the space by a line. But it is possible to have 5 constraints that form two triangles. In this case there are at most 3 constraints met by a feasibility point. In this case the space is not convex and does not form a convex domain. So the functions themselves can be convex functions but their domain of intersection may not be convex making it impossible to find a feasibility point.

In electromagnetics we are well used to solving problems with one base station with fixed position and many mobile receivers. The solution is obtained from a linear systems of equations of the form $Ax = b$ where A is an $n \times n$ matrix and $x, b \in R^n$. This problem is a linear programming problem with no inequality constraints. But in the optimisation problem that we need to consider for indoor radio wave propagation, we have many antennas whose location must be optimised for many mobile terminals.

A lecture on this subject was presented by Boyd[12] implementing a linear fractional program. The program could be cast as a linear programming problem. The optimisation problem is described as:

$$\begin{aligned} \text{minimize} \quad & \tfrac{c^T x+d}{e^T x+f} \\ \text{subject to} \quad & Gx \leq h, \\ & Ax = b. \end{aligned} \tag{6.5}$$

where $c, d, e, f, x \in R^n$ and $G \in R^{m \times n}$ and $A \in R^{n \times n}$.

Rewriting this problem we can express the problem as a linear program of the form:

$$\begin{aligned} \text{minimize} \quad & c^T y + dz \\ \text{subject to} \quad & Gy - hz \leq 0, \\ & Ay - bz = 0, e^T + fz = 1, \\ & z \geq 0 \end{aligned} \tag{6.6}$$

where $y, z \in R^n$ are introduced to rearrange the problem.

We will now conclude this chapter with a path-following solution of a linear programming problem. In the next chapter we will see that the problem to be solved appears at first to be linear but is in fact non-linear, but the path-following technique presented here can be used to solve the problem.

The linear programming problem that we wish to solve will be of the form:

$$\begin{aligned} \text{minimize} \quad & c^T P \\ \text{subject to} \quad & AP \leq b, \\ & P \geq 0 \end{aligned} \tag{6.7}$$

where $c \in R^n$ is a cost function on the variable $P \in R^n$, and P is the output power of the each server.

We will not give any more details about our problem as of yet. What is stated above in equation (6.7) is sufficiently general for the approaches that we wish to now present. We first describe the barrier function and its purpose and then a method to converge towards an optimal solution (all described in Boyd[12]).

6.2.1 Barrier Functions

The logarithm barrier function is defined as:

$$\text{minimize} \sum_{i=1}^{m} -\ln(b_i - a_i^T x) \tag{6.8}$$

where we define $x = -\infty$ when the $b_i - a_i^T x \leq 0$, and the domain of the barrier function is given by:

$$\text{dom } f \quad = \quad \{x | a_i^T x < b_i \text{ for all } i = 1, 2, \cdots, m\} \tag{6.9}$$

We will see that the barrier function of equation (6.8) can be used to combine the inequality constraints with the objective function of equation (6.7) making the linear program more practical to solve. So assuming that we can combine the constraints and objective function what remains for the problem in equation (6.7) is to define a way of iterating from some starting solution in the domain where the feasible solution exists until we travel to the optimal point. One simple algorithm which can be used to do this is the steepest descent method. We define a change in direction by

$$x^{(k+1)} \quad = \quad x^{(k)} + v^{(k)} r^{(k)} \tag{6.10}$$

where $r^{(k)}$ is the distance covered in the k^{th} step and $v^{(k)}$ is the unit vector specifying the direction in which the variable x is moving.

6.2.2 Steepest Descent Algorithm

The algorithm for the general descent method then takes the form

given a start point $x^{(0)} \in \text{dom } f$

$k = 0$

repeat

  Determine a descent direction $v^{(k)}$

  Perform a line search. Choose some $r^{(k)} \geq 0$

  $x^{(k+1)} = x^{(k)} + v^{(k)} r^{(k)}$

  $k = k + 1$

until stopping criteria is met

There are many ways in which we can define a descent direction to obtain the vector $v^{(k)}$, one simple way is to define the steepest descent method which is obtained by taking the L_∞ norm of the gradient of the function f. The reason we might choose

this direction is because it indicates the worst direction in which the residue of the solution exists, and therefore the obvious direction to travel in is this direction, to try and correct the solution. This may not seem that obvious at first, but particularly in the case of the indoor optimisation problem described in the next chapter, it will be seen that this is a very natural direction to take. Many other possibilities exist, one which is commonly used is the Newton method, or the use of a method that uses the previous search direction to give information about the newest search direction (see Powell[67]).

The steepest descent algorithm is then defined as:

given a start point $x^{(0)} \in \text{dom } f$

$k = 0$

repeat

Determine the steepest descent direction $v_{sd}^{(k)} = -\|\nabla f\|_\infty$

Perform a line search. Choose some $r^{(k)} \geq 0$

$x^{(k+1)} = x^{(k)} + v^{(k)} r^{(k)}$

until stopping criteria is met

6.2.3 Line Search Methods

There are two types of line search algorithms usually used, either an exact one in which the value $r^{(k)}$ is calculated exactly, or using an iterative technique called the backtracking line search. This method is inexact so that it only approximates the search direction. The function f along the line $(x^{(k)} + r^{(k)} v^{(k)})$ must be reduced so that the solution is increasing. By increasing we mean that $f(x+h) > f(x)$ for some h. The algorithm is described as follow:

$t = 1$;

while$(f(x^{(k)} + r^{(k)} v^{(k)}) > f(x^{(k)}) + \alpha r^{(k)} \nabla^T f v_{sd})$

$t = \beta t$

end

The constant α have a value usually in the range $[0.1, 0.3]$ so that the evaluation of f at the point x be reduced by 10% to 30% each time a step is taken to a new point. The value β is usually about 0.5 so that the step length is halved obtaining a usable point in a reasonable amount of time. If we use too large a value of β then the line search will require a large number of iterations in many cases, while setting it too small can obtain a value that is not close enough to our required solution. It was found in practice that $\alpha = 0.3$ and $\beta = 0.5$ give solutions that converge quickly to their optimum.

6.2.4 Stopping Criterion

Defining a stopping criterion is usually related to the gradient of f, and takes the form $\|\nabla f\|_\infty < \eta$ where η is some small positive real number.

6.2.5 Sequential Unconstrained Minimisation Technique (SUMT)

For the linear program:

$$\begin{aligned} \text{minimize} \quad & c^T x \\ \text{subject to} \quad & Ax \leq b, \\ & x \geq 0 \end{aligned} \tag{6.11}$$

with the steepest descent direction, the line search, barrier method and stopping criterion defined, we can define a method known as the Sequential Unconstrained Minimisation Technique (SUMT). First the constraints are combined into the objective function to obtain an unconstrained problem. The logarithm barrier method is introduced to define the unconstrained linear programming problem as:

$$\text{minimize } f(x) = tc^T x - \sum_{i=1}^{m} \ln(b_i - a_i^T x) \tag{6.12}$$

where t is a value which is very small if we want to emphasise the constraint terms, and very large if we want to emphasise the objective function.

We require the gradient of the barrier function for the steepest descent gradient function.

$$\nabla\left(\sum_{i=1}^{m}\ln(b_i - a_i^T x)\right) \;=\; \sum_{i=1}^{m}\frac{a_i}{b_i - a_i^T x} = A^T d \tag{6.13}$$

where $d = 1/(b_1 - a_1^T x, b_2 - a_2^T x, \cdots, b_n - a_m^T x)$.

The complete SUMT method can be now defined as follows:

Define $\alpha \in [0.1 - 0.5], \beta = 0.5, \eta = 10^{-3}, \epsilon = 10^5, \mu = 5, t_0 = 10^{-3}$

$b, d \in R^m, A \in R^{m\times n}, x \in R^n$

$t = t_0$;

Repeat

{

do

{

$d = 1/(b - Ax)$;

$\nabla f = tc + A^T d$;

$v_{sd} = -\|\nabla\|_\infty = -\max(\nabla f_i)$;

} Steepest Descent Direction

$f(x) = tc^T x - \sum_{i=1}^{m}\ln(b_i - A_i^T x)$; } Unconstrained Objective Function

$r = 1$;

while ($f(x + rv_{sd}) > f(x) + \alpha r \nabla f v_{sd}$ or $f(x + rv_{sd})) = -\infty$)

{

$r = \beta r$;

}

} Line Search Method

$x = x + rv_{sd}$;

}

while ($\|\nabla f\|_2 \le \eta$)} Stopping Criterion

if ($m/t < \epsilon$ or $r < 10^{-10}$)

Stop;

} SUMT Stopping Criterion

$t = \mu t$;

}

This is the standard SUMT method described as described by Boyd[12], with a few small changes. The while loop contains a reference to the case when a line search crosses a constraint, when this happens the barrier function will have the value $-\infty$. The line search must continue until a point is found inside the domain. Also, added is a condition that if the distance travelled by the search is less than 10^{-10}, then the algorithm terminates. This is perfectly reasonable since the convergence is related to the length of the line search step. The smaller the step, the closer the point is to the optimal solution.

6.2.6 Example of SUMT method

What follows is an example of the SUMT method applied to a linear combination with two variables and seven constraints. The linear programming problem presented by Beasley[8] is described as:

$$\begin{aligned} \text{minimize} \quad & 180x + 160y \\ \text{subject to} \quad & 6x + y \geq 12 \\ & 3x + y \geq 8 \\ & 4x + 6y \geq 24 \\ & x \leq 5 \\ & y \leq 5 \\ & x, y \geq 0 \end{aligned} \tag{6.14}$$

If equation (6.14) is rewritten in the form of equation (6.11) then the form obtained is easily solvable using the SUMT method. This is exactly what will be done in the next chapter when solving the indoor resource optimisation problem.

$$\begin{aligned} \text{minimize} \quad & 180x + 160y \\ \text{subject to} \quad & -6x - y \leq -12 \\ & -3x - y \leq -8 \\ & -4x - 6y \leq -24 \\ & x \leq 5 \\ & y \leq 5 \\ & x, y \geq 0 \end{aligned} \tag{6.15}$$

Note that $c = (180, 160)$, $P = (x, y)$ and $a_i^T x \leq b_i$ for all $i = 1, 2, \cdots, 7$.

Drawing the constraints on a cartesian plane it is easy to see the region of feasibility for the solution. The domain or region of feasibility is marked in Figure 6-1 is shaded.

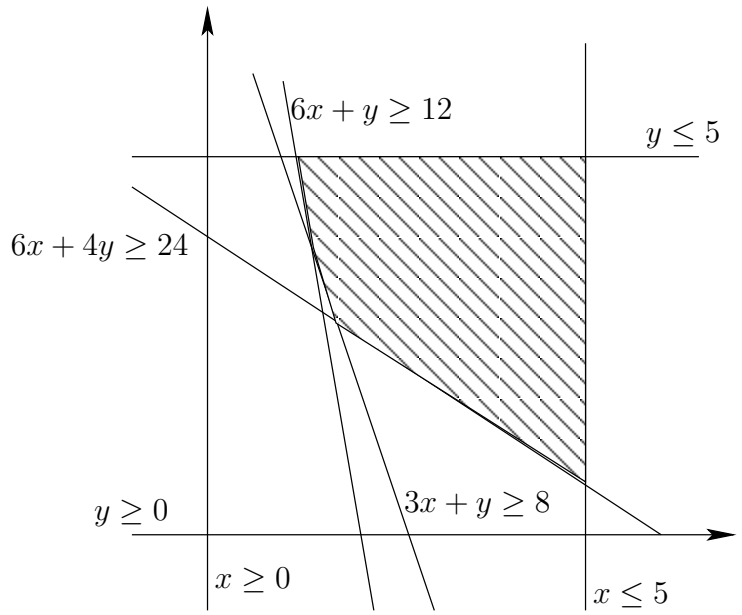

Figure 6-1: Feasible region for convex optimisation problem with 2 variables and 7 constraints

Starting at some point within the feasibility domain, say $x = (4.9, 4.9)$ it is possible to iterate to the optimal solution. The variables controlling the convergence of the method are set to be $\beta = 0.5, \alpha = 0.3, \eta = 10^{-3}, \epsilon = 10^{-5}, \mu = 5$ and $t_0 = 10^{-3}$. The solution converges in 13 iterations but even gives very good results after 10 iterations. Figure 6-2 show how the result converges to the optimal $x = 12/7, y = 20/7$.

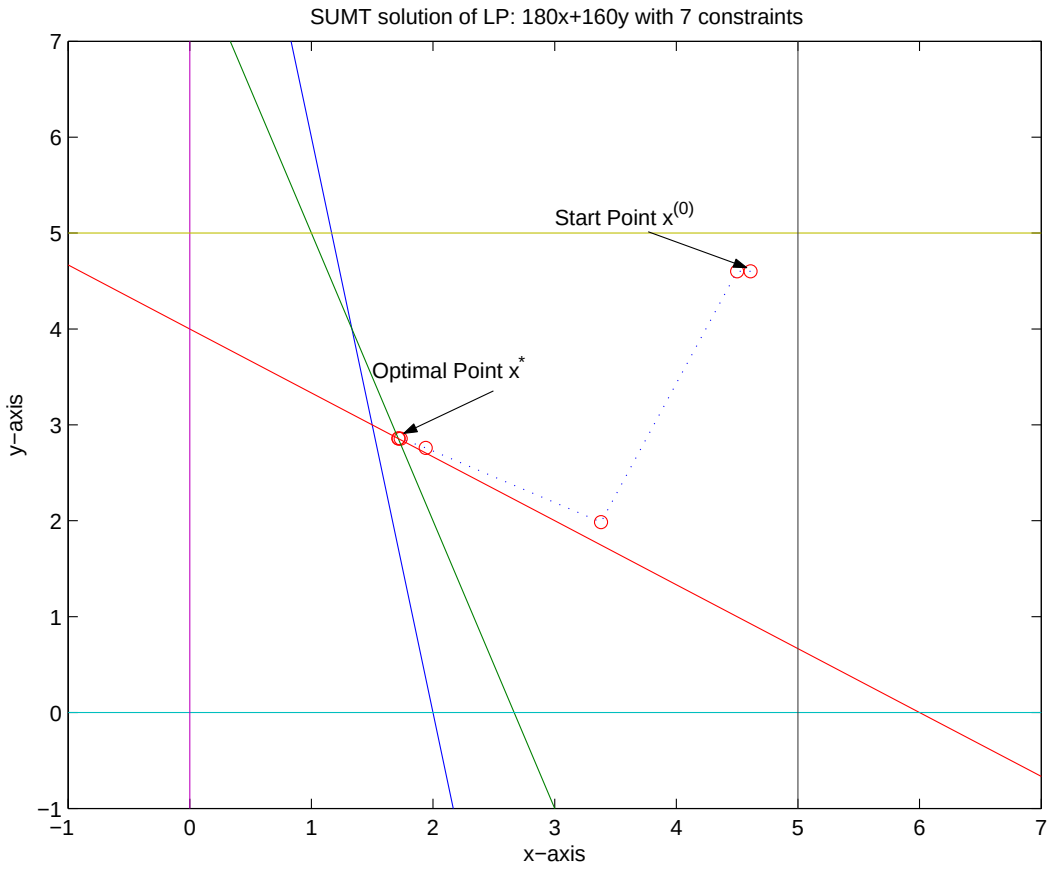

Figure 6-2: Convergence to the optimal result in 13 iterations of SUMT

Chapter 7

Indoor Resource Optimisation for TDMA

In a telecommunications system the downlink is the connection from many servers in a network to many receivers. These receivers are usually called user equipment (UE) because they range from voice links on mobile phones and palm-pilots to laptops and multimedia phones. The uplink is the connection from the UE back to a receiver in the server.

When a simulation is performed to obtain the optimal number of users required to be attached to the system, we usually perform what is known as a downlink and uplink optimisation. The downlink optimisation requires a number of user equipments with a particular capacity requirement assigned to each, to be connected to the system. The uplink optimisation determines how many can connect to the system assuming that each UE is possibly interfering with one another and that they are randomly distributed in the building.

7.1 Downlink Optimisation Requirements

Before beginning the description of the downlink optimisation algorithm it is necessary to describe:

1. the physical environment required by the model.

2. the traffic in the system.

3. the UMTS system requirements.

7.1.1 The Environment

The environment will be a multi-story indoor building defined exactly as in Chapter 4. The walls, doors, windows, floors and ceilings will consist of filled convex spaces having permittivity, permeability and conductivity parameters associated with them. For experimental purposes the filled convex spaces can be perfect electric conductors (PEC), lossless or lossy.

7.1.2 Traffic

User Equipment (UE) can be a mobile phone, lap-top or desktop computer. The receiver positions in the building will serve as positions where UEs can be placed. The capacity required by the UEs can be defined as the traffic of the system. Each user will require a service suitable for their needs. For instance if a person requires a mobile call they will require a voice link at 12.2 kbps. Whereas if a person is using a laptop they may require a high speed connection rate of 128 kbps or higher. The capacity of the system is a function of the area, number of users and capacity requirements of each user of the system. This can be expressed numerically as:

$$\overline{\gamma} \quad = \quad \sum_{i=1}^{N} \gamma(x_i, y_i, z_i) \tag{7.1}$$

where $\overline{\gamma}$ is the total capacity requirement in the system, and $\gamma(x_i, y_i, z_i)$ is the capacity requirement of a user at position (x_i, y_i, z_i), where there exists N users.

For a time division duplexing (TDD) based system the statistic of interest is not the path-loss, rather it is the signal to interference ratio (SIR). The target signal to interference ratio is related to the energy per bit per noise factor written Eb/No. At each user position we need to generate a measure of the required signal level S_L defined as follows:

$$S_L \quad = \quad \frac{I_m F_m R_s}{P_g} \tag{7.2}$$

where I_m is the interference margin, F_m is the fade margin, R_s is the receiver sensitivity, and P_g is the processing gain.

The receiver sensitivity is calculated using the following formula:

$$R_s = kTBN_fEb/No \tag{7.3}$$

where $k = 1.380658 \times 10^{-23} J/K$ is the Boltzman constant, $T = 290K$ is the temperature measured in Kelvin of the antenna, $B = 3.84MHz$ is the bandwidth and $N_f = 5dB$ for base stations and $7dB$ for receivers is the noise factor defined by Nokia[52].

We will see that in practise we can remove the fade margin from the calculations if we can define a mean signal value over a small area. We will see later that this can be achieved by the use of a mean random value of the signal value supplied by a ray-tracing model.

Table 7.1 shows the E_b/N_o, fade margin and processing gain based on measurements made by Nokia[52] defined in a book on the subject of UMTS.

In fact the target signal to interference ratio (tSIR) required for our problem will be defined as

$$tSIR = \frac{E_b/N_o}{P_g} \tag{7.4}$$

The interference margin is usually included in the SIR formula, but in this case is not defined because all interferers are known in the system.

7.1.3 UMTS System Constraints

Each base transceiver station (BTS) for the UMTS system contains a number of servers. Each server contains one antenna system. In practice the antenna can fall into one of the following four categories: it could be a dipole, be sectorized (usually into 90^o sectors), consist of an array or a smart antenna. For the optimisation tool we will assume that the antenna is omni-directional or sectorized for simplication purposes. A more complicated antenna type leads to a much later number of unknowns in the problem.

Direction	Service	Eb/No	Fast Fade Margin(dB)	Processing Gain (dB)
Downlink	12.2 kbps voice	9.4	5.5	12
	128 kbps real-time data	11.7	3.5	2.4
	128 kbps non real-time data	6.7	3.1	2.4
Uplink (receive diversity)	12.2 kbps voice	1.7	6.3	12
	128 kbps real-time data	1.0	6.3	2.4
	128 kbps non real-time data	0.3	3.4	2.4
Uplink (no receive diversity)	12.2 kbps voice	8.6	6.3	12
	128 kbps real-time data	8.7	6.3	2.4
	128 kbps non real-time data	6.4	3.4	2.4

Table 7.1: Table of E_b/N_o rates, fasde margins and processing gains.

Usually there is a cost function, in our case this will be related to the capacity requirements of the users only. The economic cost is not taken into account. The economic cost is related to the cost of certain antennas as well as the cost associated with where they can be positioned in a building. The economic cost can contain parameters such as installation, maintenance, health and appearance.

Power control at the BTS and the UEs is always discrete with a maximum permissible power level available which we will define as W_{max}. We define the power P_i in the i^{th} BTS to be an element of the discrete set $\{W_1, W_2, \cdots, W_{max}\}$. The maximum permissible power is defined as:

$$W_{max} = R_s I_m R_{min} \tag{7.5}$$

where R_s and I_m are already defined, and R_{min} is the minimum path-loss to

another base station from the current server in the current base station.

The receiver sensitivity is defined to be the signal required to provide a defined error output from the receiver. It is obvious from its definition that the receiver sensitivity is related directly to the signal to interference ratio (SIR). In the case of an uncooperative system we use the term acceptable interference level instead of receiver sensitivity. An uncooperative system is another system that is set up separately from the current system in use, and the telecommunication has no control over how it is run.

The interference margin is a statistic which states a value above the interference signals that the received signal must exceed. In the case of uncooperative systems we call this the protection ratio. It is a value below the receiver signal level, that the interferers signals may not exceed.

7.2 Non-linear Downlink Optimisation Algorithm

The algorithm described by Rappaport[71] employs a non-linear optimisation technique which places a number of base stations in a building and then uses a gradient technique to iterate to an optimal set of locations for the base stations subject to a number of path-loss constraints for a given distribution of UE's and an objective function consisting of a linear combination of minisum and minimax objective functions.

The form of the objective function at first seems very similar to the function mentioned in the previous chapter. What makes it different is the change in location of the base station at each step of the optimisation procedure. This also results in changes in the constraints since they are interrelated. This makes the whole problem non-linear since the domain of the objective function is changing at each step of the optimisation procedure.

In the previous chapter the general descent method was described as:

given a start point $x^{(0)} \in \text{dom } f$

$k = 0$

repeat

Determine a descent direction $v^{(k)}$

Perform a line search. Choose some $r^{(k)} \geq 0$

$x^{(k+1)} = x^{(k)} + v^{(k)} r^{(k)}$

$k = k + 1$

until stopping criteria is met

The optimisation technique requires a starting solution, a method to obtain the descent direction, a search direction to be chosen and a stopping criteria. The starting point $x^{(0)}$ is defined to be the locations of the base stations each of which is allocated at one point at the centre of gravity of a hyper-rectangle. These hyper-rectangles must be predetermined. The descent direction can be obtained by using a number of methods such as the conjugate gradient, Newton or Hookes and Jeeves method. The stopping algorithm is usually related to a measure of the gradient change as described in the previous chapter.

The method of Rappaport[71] was modified and improved in this thesis to include:

1. An improved layout for what he calls hyper-rectangles, these are rectangles in which a base station is given the freedom to be moved so long as that base station does not cross the perimeter of the rectangle. We found that we could base the algorithm for allocating the hyper-rectangles upon the amount of capacity required by a user in a certain area.

2. Instead of using a heuristic pathloss model Seidel, Rappaport[70] we used a ray-tracing method that can be iteratively applied in the optimisation algorithm for increasing orders of reflections.

3. The objective function of interest in the original method was based on signal strength (path-loss) but in this new approach the signal to interference is used giving a more descriptive representation of the interaction between the base stations in an indoor environment.

4. More complicated antenna systems can be incorporated into the problem, not just omni-directional antennae.

5. An alternative stopping algorithm is presented which includes a measure of user capacity reached by the system.

6. Annealing is used to jump out of local maxima.

7. A hard handover algorithm can be implemented to avoid overflow of a server. In TDD there is never soft handover. The base station hands over some of the UE's to another base station. This can be only implemented at the end of an optimisation procedure, otherwise it was found that the non-linear optimisation technique becomes unstable.

8. The mean of a random phase is applied to the ray-tracing so as to avoid fading. We want an average path-loss over a small area, so this is a good way to obtain a good estimate of the mean.

Each of these points are now discussed in each of the following sub-sections 7.2.1 to 7.2.7.

7.2.1 Allocation of Hyper-Rectangles where Base Stations Reside

The method of Rappaport[71] uses a centre of gravity approach to find the location of a hyper-rectangle where the initial position of the base stations is allocated, in the vicinity of receivers (x_i, y_i, z_i) each having an associated priority weight w_i, so that the centre of gravity c_j in the j^{th} hyper-rectangle will be calculated using the formula:

$$c_j = \left(\frac{\sum_{i=1}^{N} w_i x_i}{N}, \frac{\sum_{i=1}^{N} w_i y_i}{N}, z_i \right) \tag{7.6}$$

Rappaport does not suggest a physical interpretation for the weights, but we do know that they must be set by the user of the system. In this implementation the

weights $w_i = \gamma_i$ are related to the capacity γ_i in the system. So the starting location for our base stations will be the centre of capacity Γ_i:

$$\Gamma_i \quad = \quad \left(\frac{\sum_{i=1}^{N} \gamma_i x_i}{N}, \frac{\sum_{i=1}^{N} \gamma_i y_i}{N}, z_i \right) \tag{7.7}$$

This is exactly what you would expect, since the base station needs to be in close vicinity to the high capacity links and is not required to be as close to the lower capacity links.

Rappaports method for calculating the hyper-rectangles is given as follows:

1. The building is stored inside one hyper-rectangle.
2. Find the centre of gravity in all hyper-rectangles.
3. Split across the longest dimension in the x or y direction generating a new set of two hyper-rectangles.
4. Continue the algorithm as in steps 2-3 splitting the hyper-rectangles until the required number of base stations is obtained.

In our case we know that the capacity of the servers is $s_j = 2Mbps$, so that the server contains receivers whose capacity when added together will not exceed the capacity of the server. Therefore we can implement the constraint that

$$\sum_{i=1}^{N} \gamma_i \quad \leq \quad s_j \tag{7.8}$$

We define the splitting algorithm as follows:

1. The building is stored inside one hyper-rectangle.
2. Find the centre of capacity in all hyper-rectangle.
3. Split across the x and y direction to obtain two hyper-rectangles in each case. The hyper-rectangles that contain the smallest number of servers will be the chosen splitting direction for the hyper-rectangles.
4. Continue the algorithm as in steps 2-3 until all hyper-rectangles meet the server capacity constraint.

7.2.2 Objective Function and Constraints

The objective function f of Rappaport consists of a linear combination of a minisum objective function f_1 and minimax objective function f_2 subject to a number of placement constraints. These constraints as stated above are the boundaries of the hyper-rectangles. The minisum objective function has the drawback that it might ignore some remotely located UEs, while obtaining a good total weighted coverage. The minimax objective function on the other hand has the drawback that it concentrates on the worst case situation at the expense of the overall averaged weighted coverage. For this reason the linear combination of the two methods is implied. Rappaport uses a method based on signal strength while we know in practice that the signal to interference ratio is the statistic of real significance. Rappaports non-linear optimisation problem is stated as:

$$\begin{array}{ll} \text{minimize} & f(X,Y,Z) = \phi f_1(X,Y,Z) + (1-\phi) f_2(X,Y,Z) \\ \text{subject to} & 0 \leq x_j \leq h_{j1}, 0 \leq y_j \leq h_{j2}, \\ & 0 \leq z_j \leq h_{j3} \text{ for all } j = 1, 2, \cdots, n \end{array} \tag{7.9}$$

where

$$f_1 = \frac{1}{m} \sum_{i=1}^{m} w_i \left[p_i(X,Y,Z) + \mu_i \max\{0, p_i(X,Y,Z) - s_i\} \right] \tag{7.10}$$

$$f_2 = \frac{1}{n} \sum_{j=1}^{n} \max_{i \in S_j} w_i \left[p_i(X,Y,Z) + \mu_i \max\{0, p_i(X,Y,Z) - s_i\} \right] \tag{7.11}$$

and $X = (x_1, x_2, \cdots, x_n)$, $Y = (y_1, y_2, \cdots, y_n)$, $Z = (z_1, z_2, \cdots, z_n)$. (x_i, y_i, z_i) is the current position of the base station in the i^{th} hyper-rectangle H_i of the building. s_i is the required signal strength at a UE location and p_i is the calculated path-loss at m receiver points using the 914MHz path-loss model described in Rappaport[70]. μ_i are the penalty functions defined at each UE location.

When using a signal to interference based formula there is a significant change of constraints and of the functions f_1 and f_2.

Firstly the path-loss model is replaced with a ray path-loss model. $p_i(X,Y,Z) = (\|R(r_1 - r_{ik})\|, \|R(r_2 - r_{ik})\|, \cdots \|R(r_m - r_{ik}\|)$ is defined to be the ray-path loss from m transmitters to the receiver point r_{ik} that has best server k. The constraints $p_i > s_i$

are replaced with signal to interference ratio constraints of the form $SIR > tSIR$ where $tSIR$ is a target interference ratio to be met, described in Section 7.1.3. The modified objective function f_1 and f_2 take the form:

$$f_1 = \frac{1}{m}\sum_{i=1}^{m}\gamma_i\left[p_i(X,Y,Z)+\mu_i\max\{0,\mathrm{tSIR}_i(X,Y,Z)-\mathrm{SIR}_i\}\right] \quad (7.12)$$

$$f_2 = \frac{1}{n}\sum_{j=1}^{n}\max_{i\in S_j} w_i\left[p_i(X,Y,Z)+\mu_i\max\{0,\mathrm{tSIR}_i(X,Y,Z)-\mathrm{SIR}_i\}\right] \quad (7.13)$$

For the case of an omni-directional antenna the constraint equation is given by:

$$\mathrm{SIR}_i = \frac{P_i\|R(r_i-r_{ij})\|}{\sum_{k\neq i}P_k\|R(r_k-r_{ij})\|+n_t} > \mathrm{tSIR}_i \quad (7.14)$$

where r_i is the location of the i^{th} base station, r_{ij} is the j^{th} UE position that has best server r_i, P_i is the power transmitted from the i^{th} server. $\|R(r_k-r_{ij})\|$ is the total ray path-loss obtained by calculating a vector norm on all ray-path losses between server r_k and the point r_{ij}. The power P_i is set to be constant obtained by ensuring that the base stations do not interfer with one another. The ray-tracing technique is exactly the same as the one defined in Chapter 4. The power control derivation is described in the next section.

7.2.3 Power Control

In the case of an omni-directional antenna the formula for obtaining the transmitter power is defined by equation (7.5), where R^i_{min} is defined to be the minimum path-loss between the i^{th} base station and every other base station written as:

$$P_i = R_s I_m R^i_{min} \quad (7.15)$$

$$R^i_{min} = \min_{\forall j\neq i}\|R(r_i-r_j)\| \quad (7.16)$$

If the antenna is sectorized with m equally sized sectors $a^i_k \in \{a^i_1, a^i_2, \cdots, a^i_m\}$ then the power is multipled by a gain G_{ik} in the k^{th} sector a^i_k of the i^{th} base station to define the transmit power for that sector. The minimum path-loss for each sector is then defined as:

$$R^{ik}_{min} = \min_{\forall j\neq i}\|R(r_i-r_j)\|\mid_{a^i_k} \quad (7.17)$$

where the ray path-loss is restricted to the sector a_k^i.

We wish to set the gains G_{ik} so that the power from each sector a_k^i are given by $P_{ik} = R_s I_m G_{ik} R_{min}^{ik}$ are divided equally amongst each sector. The formula for the gain can then be defined as

$$G_{ik} = \frac{R_t^i}{m R_{min}^{ik}} \tag{7.18}$$

where $R_t^i = \sum_{k=1}^m R_{min}^{ik}$ is the total path loss for the base station. This has the effect that each sector emits P_i/m of the power where P_i is the total power output of the server.

In the case of a sectorized antenna the signal to interference ratio constraint on the optimisation changes to:

$$\mathrm{SIR}_i = \frac{\sum_{k=1}^m G_{ik} P_i \| R(r_i - r_{ij}) \|_{a_k^i}}{\sum_{k=1}^m \sum_{l \neq i} G_{lk} P_l \| R(r_l - r_{ij}) \|_{a_k^l} + n_t} > \mathrm{tSIR}_i \tag{7.19}$$

7.2.4 Stopping and Line Search Criterion

The stopping criterion is usually related to the gradient of the objective function as already stated in Section 6.2.4. In this case however an extra piece of information is added to the loop controlling the stopping criteria. We say that if the number of receivers reaching their target signal to interference ratio is above a certain percentage, then we will stop the algorithm. In practice it was found that 90% of receivers reach the required target SIRs.

Also we found that when performing the line search, we usually half the step length until we get convergence in the gradient calculation. We found that if you get an increased number of receivers reaching the target signal to interference ratio, then we should stop the line search at this point, and use the new positions as the next point in our continuing optimisation.

In the line search algorithm it is necessary to calculate finite difference derivatives to obtain the steepest descent path for the gradient method. The derivatives take the form:

$$\xi_{ij} = \frac{f(r_i + \delta e_j) - f(r_i)}{\delta} \tag{7.20}$$

giving a steepest descent direction V_{sd}:

$$V_{sd} = \max_{\forall i,j} \xi_{ij} \tag{7.21}$$

where e_j is a unit vector pointing in the x, y or z direction and ξ_{ij} is calculated for every base station position r_i. An exception to this rule is when the steepest descent direction has the effect of causing the server capacity to be exceeded. In this case the next best direction is assumed.

Rappaport used a value of 0.5 for δ for his methods and halved this twice in the next two steps to get the algorithm to converge nicely. The value was then reset again and the process would start all over again. We noted that this value should be set to be something highly physical when moving from one position to another. We know that a signal can fall sharply from one position to another by just moving centimetres at a time, so because of the sampling theorem we guessed that $\delta = \lambda/2$ would be a good starting point for the value of δ. In practice it was found that the method could become unstable if too small a value of delta was used since that would result in a line search algorithm that is moving around in fast fades. The results turned out to be meaningless in this case.

7.2.5 Annealing

It is presumed that the algorithm is in a local maximum if there is no significant change in the number of receivers meeting the signal to interference ratio, and if this happens, a step length of $\delta = 2\lambda$ is taken and the position with the highest number of receivers meeting the SIR is assumed to be the new starting point for the algorithm.

In some cases all directions for the steepest descent calculation result in the server capacity being exceeded. In this case the annealing step must be introduced to correct the problem.

7.2.6 Hard Handover

It is possible in some cases to find a position of the base stations where one server has exceeded its capacity requirement and then use a hard handover to another server

to balance the servers. It was something that we looked briefly at, but could make for a more promising algorithm in the future. Currently in the optimisation tool it is ignored.

7.2.7 Mean Path-loss Values

The mean of the path-loss for a point to point link can be calculated using the formula for the mean of a random walk. This involves taking each complex ray path E_{ij} separately between the i^{th} base station and j^{th} receiver and substituting them into a random walk formula. It should be noted that taking the random walk result yields a far more constrained system than just taking the sum of the complex ray paths. This can be seen from looking at the SIR formula:

$$\mathrm{SIR}_i \quad = \quad \frac{P_i \sum E_{ij}}{\sum_{k \neq i} P_k \sum E_{kj} + n_t} > \mathrm{tSIR}_i \tag{7.22}$$

The sum of complex numbers in the denominator tend to cancel out in phase giving a smaller absolute value of the field (path-loss), and in turn the target signal to interference ratio tends to be met more easily. We can not assume this is true in reality, since there may exist building measurement error, incorrect permittivity or neglected complexity of the building and therefore we can not exactly predict the phase of the complex number. The random walk mean value turns out to be physically more meaningful.

The total power at the mobile terminal (UE) is obtained by setting some norm on the individual ray path losses. Assuming the use of the Euclidean norm is not always correct. For instance, in a real environment their are effects due to scattering from walls that we can not predict exactly. They can be assumed to be random, so that the phase of the path loss leaving any scattering object is altered. If we want a measure of the received power at the mobile terminal, we can say that the result is obtained from a set of random variables. A good measure of the power is the mean power obtained at the receiver including gaussian random phase. An analogous way of looking at this is that we want the average power about some point so that we move the mobile terminal randomly around about its current position to avoid fading.

Takahashi[77],[78] describes a random phase summation applied to ray-tracing which is applicable for our problem.

The power loss along any ray path is a complex number of the form:

$$x_k + jy_k = E_k \exp(j\phi_k) \tag{7.23}$$

and r is the sum of N such random variables given by

$$r = \sum_{r=1}^{N} E_k \exp(j\phi_k) \tag{7.24}$$

where $E_k = \sqrt{x_k^2 + y_k^2}$ is the amplitude of the power and $\exp(j\phi_k)$ is the phase, ϕ_k is a set of independently and identically distributed uniform random variables in the range $[0, 2\pi]$.

The probability density function giving rise to the mean of the sum of the random variables is of the form

$$W_N(r) = r \int_0^\infty \xi J_o(\xi r) \prod_{k=1}^{k=N} J_o(\xi E_k) d\xi \tag{7.25}$$

The mean of the random variable is then given by

$$\overline{r} = \int_0^\infty r W_N(r) dr \tag{7.26}$$

It can be seen from the above equations (7.25) and (7.26) that the mean of the random variable is a doubly infinite integral which is quite time consuming to solve numerically. The alternative is to calculate the random variable r given by equation (7.24) n times, where n is very large and then apply the formula

$$\overline{r} = \frac{1}{n} \sum_{i=1}^{n} r_i \tag{7.27}$$

where r_i is the result of the i^{th} random variable calculation. It turns out that this procedure is even longer to calculate that the doubly infinite integral because it requires that n is of the order of 100,000 so that the error in the random mean is guananteed to be 1%.

We found that if you define a numerical quadrature rule of order 2, that is the trapezoidal rule, we can make a composite version which we apply to the calculation

of the $W_N(r)$ integral, converging to the correct solution quickly. The n^{th} order composite trapezoidal rule says that for an interval $[a, b]$ that

$$I_n = \frac{1}{2}(f(a) + f(b)) + h \sum_{i=1}^{n-1} f(a + ih) \tag{7.28}$$

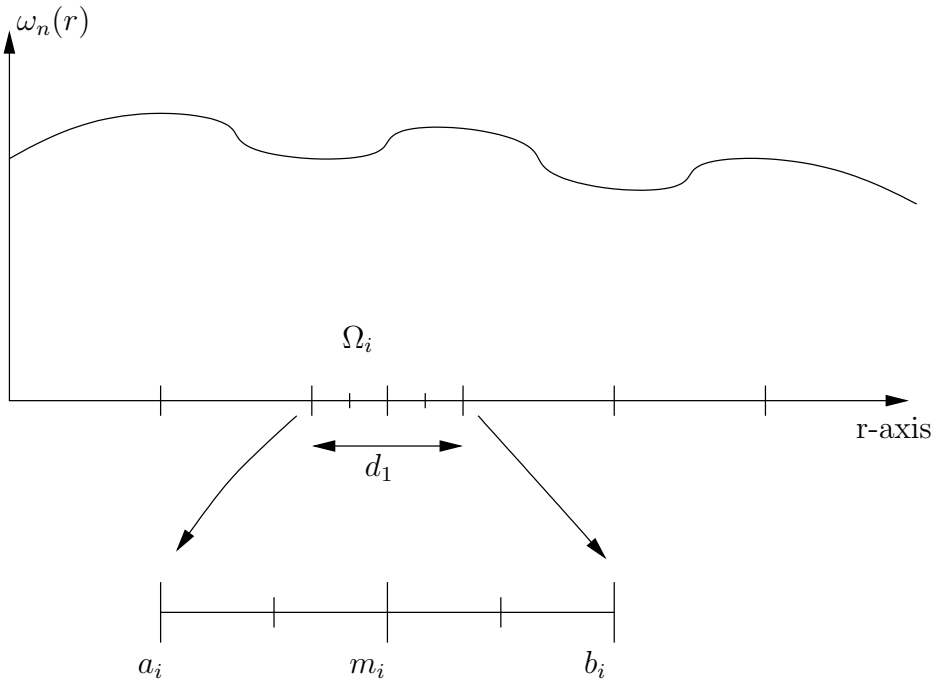

Figure 7-1: Intervals for $\mathcal{W}_n(r)$

The numerical integration $\mathcal{W}_n(r)$ of the integral $W_N(r)$ over the line $[0, \infty]$ with variable ξ must be first defined. The infinite line is divided into a number of finite intervals Ω_i of length d_2 such that $\Omega_i = [a_i, b_i] = [a_i + h_i(i-1), a_i + h_i i]$ (see Figure 7-1). A recursive trapezoidal rule is set up to find the accurate numerical solution of the integral over the subinterval Ω_i. This algorithm is defined as:

1. The 2^{nd} order composite trapezoidal rule is applied to the interval Ω_i giving an integral which uses three sample points a_i, b_i and m_i where m_i is the midpoint of the interval.

2. The 4^{th} order composite trapezoidal rule is defined by subdivided between $[a_i, m_i]$ and $[m_i, b_i]$. This integral contains 5 sample points. Note that only two function evaluations are required, since the previous three where retained

from step 1 and included in the calculation in step 2, making the algorithm much faster. This sort of speed up is not obtained easily from other quadrature rules, because the integral points do not necessarily appear in the same positions as in the previous ordered calculation.

3. A comparison between the 2^{nd} and 4^{th} order rules is made to see if there is a large error between the two.

4. The interval is then subdivided continually and the $2^{n^{th}}$ order composite result is compared with the previous calculation $2^{n-1^{th}}$ until the result converges to a satisfactory tolerance of error.

5. Iterate for increasing i until

$$\frac{\mathcal{W}_n}{\sum_{i=1}^{i=n} \mathcal{W}_n} < \text{tol}$$

Now the computation of the outer integral must be obtained. The algorithm is as follows:

1. Set a step size d_1 for the numerically finite integral I_n in the range $[0, nd_1]$ which will approximate the infinite integral equation (7.26) and assume an euler rule so that I_n takes the form

$$I_n = d_1 \sum_{i=1}^{n} r_i \mathcal{W}_N(r_i) \tag{7.29}$$

2. At each step of the calculation of the euler rule, we much calculate $r_i W_N(r_i)$ for $r_i = \{d_1, 2d_1, \cdots, nd_1\}$ until

$$\frac{r_n \mathcal{W}_N(r_n)}{I_{n-1}} < \text{tol} \tag{7.30}$$

When the tolerance is met, the integral has reached its desired accuracy and stops at that point.

This method is confirmed by comparing the numerical result with the result of equation (7.27).

7.3 Uplink Optimisation Requirements

The uplink optimisation is a simulation resulting in a number of users being able to connect to the closest base station (best server) and achieving their full capacity requirement or some percentage of their requirement.

It was decided that two types of simulations of a working system would be required. One where their is an initial set of users and more are connected or one where there are no users on the system and each user is connected one at a time. It turns out that the former is a subset of the latter by inspection so it was assumed that the population starts at nil and increases one at a time.

The choosing of the total population is directly related to the number of base stations in use. By total population it is meant the number of users that can possibly connect to the system at any one time. It is known that the number that can successfully connect at any one time to one base station in practice is 8, although the theoretical maximum is 16. Therefore we set our population to have size $8n$, where n is the number of base stations.

For any UE the following information is required:

- **Number** - An index to the mobile terminal.
- **Type** - The type of terminal either Voice, real-time data or non real-time data, will inform the user of the maximum data rate achievable for that type of use, and the height above ground of the user. For instance a PC is approximately one metre above the floor level, while a voice link is approximately 1.5 metres above floor level.
- **Reference Location** - This is an (x, y, z) coordinate which tells where in a particular story the terminal exists.
- **Final Location** - If the terminal moves then this is the position at its final state.
- **Maximum/Minimum Power** The maximum power or minimum power output from the UE must be known before commencing the initial population

selection.

7.4 Uplink Optimisation Algorithm

The algorithm for choosing the population is as follows:

- The reference location $P_i(x, y, z)$ for the UE is generated by setting x, y and z to be independent uniformly random variables. This location will be an item which if successfully connected will be pushed onto a linked list, otherwise it will be dropped and disregarded.

- Generate the UE position, if it is contained in a free convex space, i.e. not inside a wall, then it is a valid point, otherwise it must be re-generated until a valid point is found. The height is set according to the value obtained from the random number generator. Supposing it appears in the i^{th} story of the building, its height is then altered to be a height h above the floor level in accordance with the height stipulations mentioned above.

- The data rate is set using a random variable $R_i \in [0, 1]$ so that

$$\begin{array}{rl} R_i \leq a & \text{Set Voice Data} \\ R_i > a \text{ and } R_i \leq b & \text{Set non real-time data} \\ R_i > b \text{ and } R_i \leq 1 & \text{Set real-time data} \end{array} \tag{7.31}$$

  where each value a and b are predefined by the user of the system.

- Determine the best server for the current UE.

- Define the transmission power at the i^{th} UE to be P_{ij} with best server r_j as in the downlink optimisation. The transmission power in the UE must be set to incorporate power control. By this we mean that the received signal at the base station should be approximately equal for all UEs communicating with it. If the receiver sensitivity is R_s in the base station then the power at the UE must be set to be $P_{ij} = R_s \times R_{ij}$ where $R_{ij} = \|R(r_i - r_j)\|$ is the path-loss from the UE to its best server r_j.

- Next the signal to interference ratio is tested to see that it is met using the following formula

$$\frac{P_{ij}R_{ij}}{\sum_{k\neq j}\sum_{r_l\in S_k} P_{lk}R_{lj} + \sum_{r_l\in S_j} P_{lj}R_{lj} + n_t} \geq \text{tSIR}(T_{x_j}) \tag{7.32}$$

or for the case of multiple user detection (MUD)

$$\frac{P_{ij}R_{ij}}{\sum_{k\neq j}\sum_{r_l\neq S_k} P_{lk}R_{lj} + n_t} \geq \text{tSIR}(T_{x_j}) \tag{7.33}$$

In the case of multiple user detection the base station can determine which of the UEs connected to it is the correct one by analysing the encoded signal. This leads to the negligibility of the interference from the other UEs connected to that best server as can be seen from the missing term in equation (7.33).

- Now that all the information is available, such as position of the UE, maximum power and SIR information it is important to check that the capacity of the system can be met. The following steps need to be adhered to:

  1. If the signal to interference ratio is met then proceed to step 2, otherwise stop.
  2. If the number of connections to the current best server is less than 8 then proceed with current server to step 3, otherwise check next best server and proceed to step 3 if connection is possible. A failure on both, results in a dropped connection.
  3. If the total capacity in the current server is not exceeded and the total capacity will be met after adding the new UE, then proceed to step 4. Otherwise half the capacity requirement and try to meet total capacity upper bound again. Failing this an attempt is made to use the second best server and if the capacity requirement is met, again proceed to step 4.
  4. The capacity is met and connection is possible to the server so the UE is then connected to the system.

- Once the server is connected to the system, an attempt is made to add new connections, until the upper bound of $8n$ is reached.

This algorithm was run N times for a large number N to ascertain an average number of connections. So if the number of connections was x_k on the k^{th} attempt then the average was calculated using the formula:

$$\overline{x} = \frac{\sum_{k=1}^{N} x_k}{N} \tag{7.34}$$

7.4.1 Computational Savings

Another point that is important to consider is that as the number of UE connections increases, the calculation time of the signal to interference ratio in equation (7.32) and (7.33) will greatly increase, if the values are recalculated every time. Avoiding this overhead is quite simple if the signal to interference ratio is stored. The interference part of the SIR can be extracted and updated as new connections are established. Assuming that the i^{th} connection has just been added to the system each existing SIR_k for location r_k with best server r_l must be updated for $k = 1, 2, \cdots, i-1$. This can be achieved as follows:

$$\text{interference}_{old} = \frac{P_{kl} R_{kl}}{\text{SIR}_k} - n_t \tag{7.35}$$

$$\text{interference}_{new} = \text{interference}_{old} + P_{ij} P_{il} \tag{7.36}$$

$$\text{SIR}_k = \frac{P_{kl} R_{kl}}{\text{interference}_{new} + n_t} \tag{7.37}$$

Also the interference to the current server must be stored as SIR_i. The total capacity in each server and number of connections currently to each server may also be stored to increase efficiency in the algorithm.

7.5 Results

7.5.1 Downlink Optimisation for a Foyer Problem

A foyer problem with 3 large areas of high capacity links marked in brown in Figure 7-2 and low capacity links marked in blue will be used to rigorously test the correctness

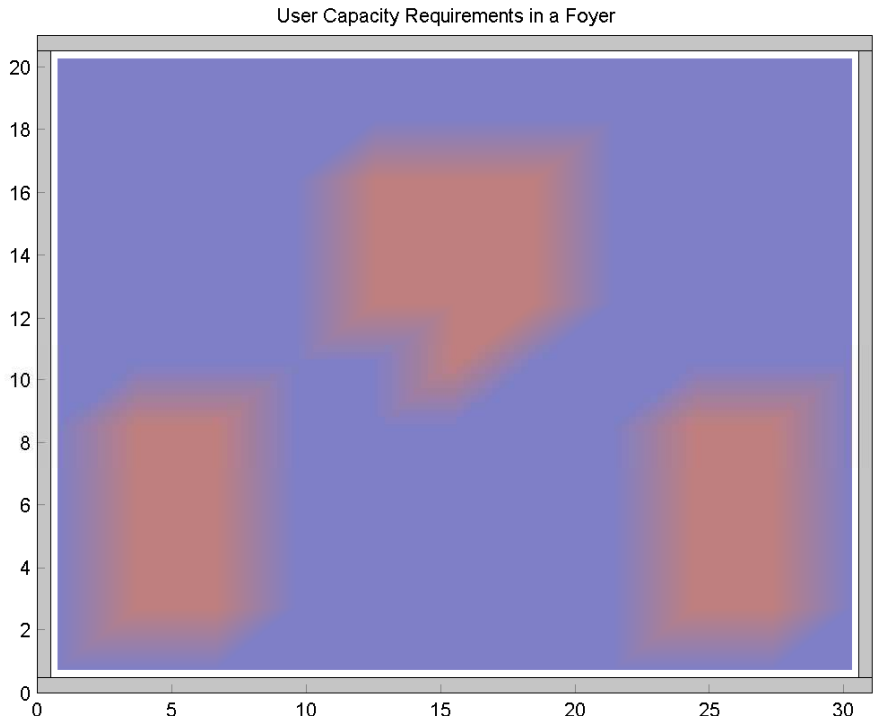

Figure 7-2: Three high capacity areas in a building foyer.

of the optimisation algorithm. For this simple configuration with a total capacity of 5 megabits, the splitting algorithm of Rappaport will split across the centre of the x-axis first, to give two hyper-rectangles each containing approximately 2.5 megabits, and then the splitting algorithm will split each of these across the y-axis to give a total of 4 hyper-rectangles each containing about 1.25 megabits.

The new algorithm determines that initially splitting across the x-axis will give 4 base stations while splitting across the y-axis initially will yield 3 base stations. The smaller number is preferred and therefore chosen. The result of the splitting is shown in Figure 7-3.

This example was specifically chosen to show how the method will define a smaller number of base stations to start with. For many tests without exception we found that this is true. Three areas of high capacity where chosen as shown in Figure 7-2 because the splitting algorithm is non-trivial in this case. If a symmetric problem was chosen the method of Rappaport would almost certainly give the same answer as the updated algorithm. These three areas represent hot-spots where we want to

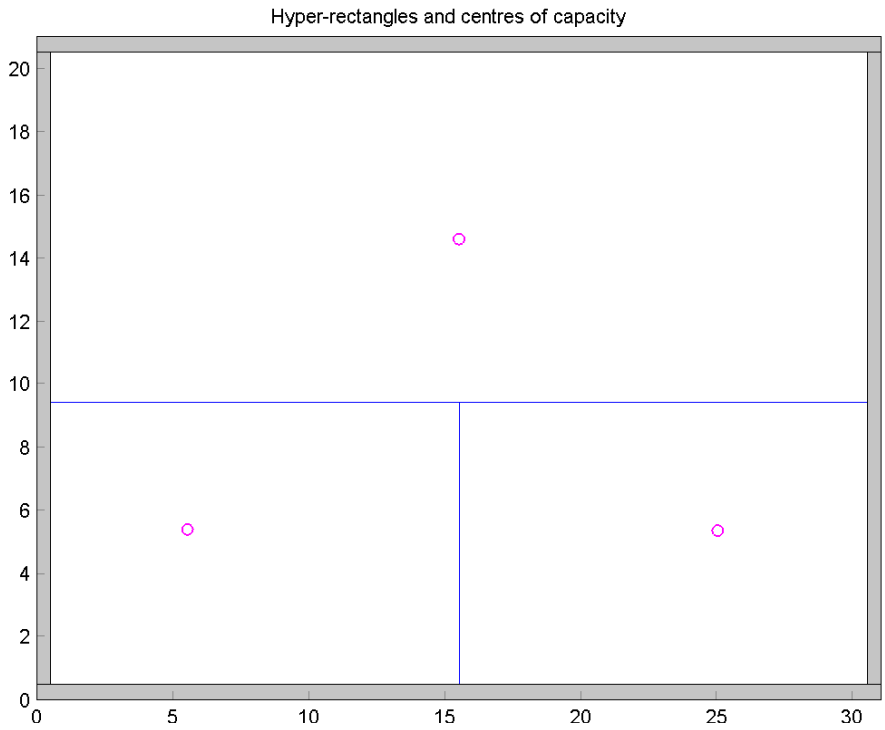

Figure 7-3: Three hyper-rectangles and centres of capacity generated using new algorithm.

try and guarantee coverage with high data rates. It is apparent when looking at the uplink optimisation part of the algorithm that users are not necessarily restricted to using high data rates in these areas. They may require high data rates elsewhere. The downlink positions of high capacity serve as a guide to how efficiently the system will meet the customers needs.

Next the downlink optimisation can be performed to achieve the optimal positions of the base transceiver stations (BTS). The chosen frequency for the simulation is 2GHz which is used for current bluetooth and WIFI technologies. The technique was able to obtain 90% of the required coverage for the user capacity requirements shown in Figure 7-2. The ray-tracing was set initially to have reflections of order 1, and then using the optimal positions obtained from this optimisation the algorithm was rerun with reflections of order 2. This is a useful way to run the algorithm, because it acts as a fine tuning in each increment. The best servers and their coverage are shown in Figure 7-4. The red, yellow and white areas correspond to the coverage points of

servers 1, 2 and 3 respectively. The black areas are the receiver positions that did not meet their SIR requirements. For this particular problem the parameters of Table 7.1 where used. The step length δ described in Section 7.2.4 was set to vary between $2\lambda = 0.3$ and $\lambda/2 = 0.075$. The noise factor in the UE for the downlink was set to be $7dB$.

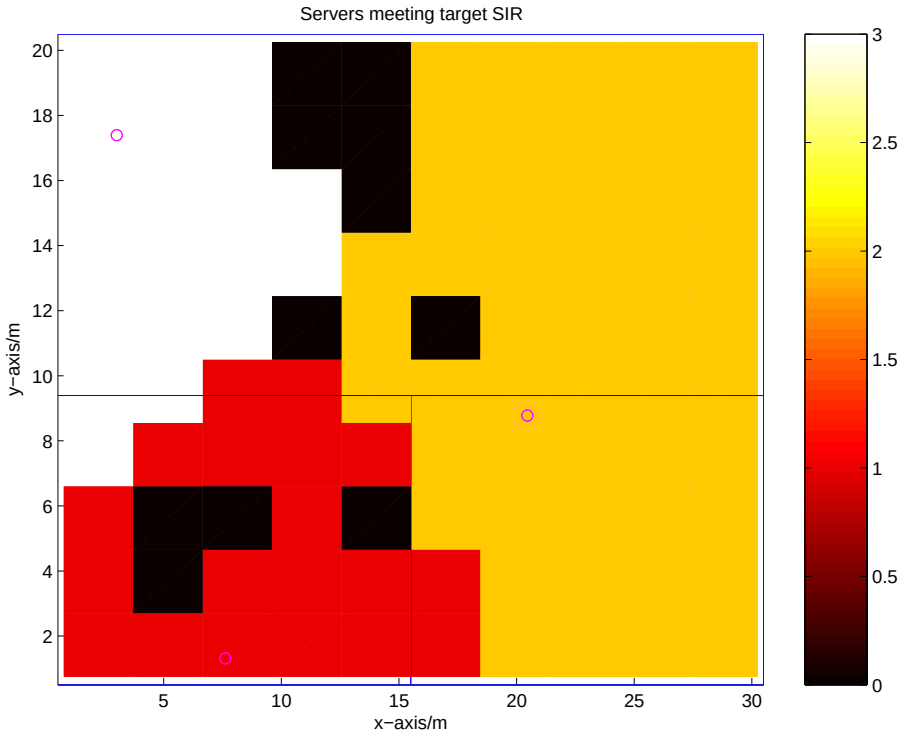

Figure 7-4: The three best server positions generated for a foyer problem used to meet 90% of the user capacity requirements.

To find the absolute theoretical optimal location for the base stations would require an order $O(N^3)$ computation where N is the number of possible base station locations defined on a regular grid. This computation could take a matter of days to run, whereas the downlink optimisation algorithm runs in just under 53 minutes.

7.5.2 Uplink Optimisation for the Foyer Problem

The uplink optimisation requires a noise factor of $5dB$ in the receiver at the BTS. A random sample of 24 points were placed in the foyer and the optimisation algorithm was run with parameters $a = 0.6$ and $b = 0.9$. This has the effect that 60% of the

connections will be voice connections, 30% will be non-real time data and 10% will require fast high speed data at $256kbps$. It turns out that the algorithm can not achieve a large number of connects at the full data rates, if the SIR is to be met. In fact only 3 or 4 connections were established in the simulations using the statistics of Nokia. Why might this be, one might ask? The first issue is that the test problem is an open foyer. This means that there are no barriers to reduce interference. Also, the SIR required for high data rates gives rise to high power levels in the UE, and this has the effect of swamping out other signals. The upshot of all of this is, that either the capacity requirements are reduced to a much smaller proportion of the required level, or some other technique must be used to achieve the high rates. In fact it has been observed in a WCDMA system currently operating in Manx Telecom in the Isle of Man, that high data rates are only achieved if the UE is almost on top of the emitting antenna. This information was obtained by private communication from a member of British Telecom. The reason for this is obvious. As the UE approaches the antenna the power required to obtain the capacity requirements is lowered, and then not as much interference is incurred by the other UEs.

Since we are interested in a TDMA system, that is one using time domain duplexing (TDD) it is possible to share the information to be sent over many time slots. This has the effect of lowering the capacity requirement in each time slot and therefore reducing the required SIR. An experiment was carried out by generating 100 samples of 24 UE locations, and the mean number of connections was found. The results are excellent from this experiment as expected. 18 out of 24 connections could meet their full required capacity. That means that about 75% meet their SIR.

7.6 Conclusions

Using a ray-tracing algorithm whose visibility algorithm does not depend on transmitter location allows the optimisation algorithm to run with reasonable computational times. If the computational times were too slow for the path-loss calculations then empirical methods would have to be used instead. This was not the case and this thesis shows conclusively that ray-tracing has a place in future optimisation techniques.

The objective function of the non-linear program is related to a measure of signal to interference ratio. In systems other than TDMA such as CDMA with FDD, a path-loss based objective function similar to that of Rappaport's could be used. The parameters described by Nokia or some similar parameters would still be required to define realistic system parameters.

The main novelty in the optimisation technique used in this thesis is in the initial placement of the base stations, the writing of the problem as a signal to interference problem, the use of realistic parameters, the use of a better norm on the path-loss value (mean path-loss) and introduction of more complicated antenna types.

Chapter 8

Conclusions

This work introduces two novel extensions to ray-tracing, one being the expression for the reflected field from a dielectric slab attempting to improve on the method of Burnside[18] and using a method that is faster than a conventional ray-tracing method of images to calculate all internal reflections in the slab. This method was shown to give different results from that of Burnside and should be more accurate since the angles of incidence are allowed to vary for each internal reflection whereas Burnside's formula assumes a constant angle of incidence for all rays inside the slab.

The second method is a truncated half-plane solution based on the Sommerfeld Wein-Hopf approximation to the diffracted field derived in two dimensions and modified for use in three dimensions. The result was applied to a small rectangular plate where there are known to exist large discrepancies in the scattered field when applying the uniform theory of diffraction solution. The novel method gives a much better approximation to the scattered fields for clearly defined angular ranges.

A new building description expressing the building volumetrically as a contiguous set of convex spaces was defined in this thesis. A ray-tracing method using the method of images is applied to find the reflection points. A tree of images of the transmitter is created, and the connectivity of the convex spaces is used to quickly trace from an image to any receiver point in the building. The convex spaces are used to determine the location of diffraction edges and a diffraction tree is created for each edge with up to one order less than the maximum order of the reflection images tree. The convex

space description replaces the standard visibility algorithms previously described in the literature, and makes the ray-tracing faster than most standard ray-tracing. In particular the fact that the connectivity is not related to the transmitter location means that the software can be run over and over again for different positions of transmitters without having to pre-compute a visibility tree. The connectivity of the building is precomputed just like a standard visibility algorithm except that it needs only to be done once and then never again. Because the convex space description of the building is used in this way it lends itself very well to optimisation algorithms where the base station location is changing at every iteration.

A number of quite involved tests were performed to clarify that the ray-tracing procedures coded in C++ were working correctly. These involved specific tests used to check any omission of ray-paths, and to check the correctness of the electromagnetic equations explained in chapter 2. A measurement campaign was also set up with two measurement set. Although the permittivity of the walls, doors and windows are unknown and therefore were guessed at, the results are good when comparisons were made between the ray-tracing and the measurement sets. No augmentation of the ray-tracing was required to get a good fit to the measurements.

The optimisation algorithm of this thesis is based on a non-linear optimisation technique of Rappaport[71]. It's novelty is in the changes to the original algorithm where the initial position of the antennas is redefined, an empirical path-loss model is replaced with the ray-tracing techniques mentioned above, the stopping algorithm is changed, and the constraints are changed to accommodate a TDMA system simulation. Fade margins are neglected when an average measure of the path-loss is used, to give a more constrained optimisation procedure. Meaningful system parameters are introduced in accordance with specifications by Nokia[52]. Simulations of the system show that other systems will not meet their capacity requirements as easily as a TDMA system.

Appendix A

Numerical Methods for Finding the Angle of Incidence into a Dielectric Slab

The methods explained in the following two sections are root finding methods. They start with some function $f(x) = 0$ with variable x. Either the bisectional algorithm or Newton-Raphson method is applied to the function f giving a root. In each case the correct root is found if a suitable range containing the root is defined at the start of the process.

A.1 Bisection Algorithm

In this thesis the bisection method is used to find the transmission points into a dielectric slab with a number of predetermined internal reflections. In many standard text books it is also used to obtain solutions of convex optimisation problems where the solution converges to an optimal solution.

The bisection algorithm requires a range of validity for the solution. If we have a function $f(x)$ containing n roots then we need to know something about the nature of the function so that we can pick our range of validity.

In the case of a dielectric slab we want to find the incoming angle θ_i but we know

that the value required is in the range $[0, \pi/2]$ from the geometry of the problem. We also know that if we obtained a reflection from the surface with no internal reflections, that the angle of incidence θ_0 is larger than the solution obtained from the cases where internal reflections are included. This leads us to the conclusion that a tighter range $[a_{lower}, b_{upper}] = [0, \theta_0]$ can be assumed.

Some books define the method in such a way that if an end point and middle point are the same sign, then the end point is set to be the middle point. Dividing the end point and midpoint values and seeing if that value is greater than zero is equivalent to doing a sign check.

We may apply the bisection algorithm as follows:

Define $a_{lower}, b_{upper}, f(x), \text{tol};$

$while(\mid b_{upper} - a_{lower} \mid > tol)$

{

$c_{middle} = \dfrac{(a_{lower} + b_{upper})}{2};$

$if(f(c_{middle})/f(a_{lower}) > 0)$

$a_{lower} = c_{middle};$

$else$

$b_{upper} = c_{middle};$

}

A.2 Newton-Raphson Method

The Newton-Raphson method requires the function $f(x)$, its derivative $f'(x)$ and a starting guess $x^{(0)}$. The starting guess used in the dielectric slab problem is either $x^{(0)} = \pi/2$ or $x^{(0)} = \theta_i^0$.

The algorithm is defined as:

Define $f(x), f'(x), \text{tol};$

Set initial guess $x^{(0)} = \theta_i^0;$

$n = 0;$

$$
\begin{aligned}
&while(x^{(n)} - x^{(n-1)} > \text{tol})\\
&\{\\
&\quad x^{(n+1)} = x^{(n)} - \frac{f(x^{(n)})}{f'(x^{(n)})};\\
&\quad n++;\\
&\}
\end{aligned}
$$

Appendix B

Future Work

B.1 Verification of Improvement to Burnside's formula

The numerical technique used to improve on Burnside's formula explained in Chapter 3, needs to be verified by an exact solution of the slab problem obtained using an integral equation approach.

B.2 Extensions of Truncated Half-Plane Solution

Considering the truncated half-plane result obtained for a three dimensional problem as in Chapter 3, it should be possible to apply the two-dimensional result to some indoor three dimensional cases. The area where the application could prove beneficial is in corridors where a number of walls are intermittently split by doors (see Figure B-1). The field is scattered off many corners at low angles where the UTD solution breaks down. Also the multiple diffractions need to be accounted for. Taking a two dimensional cross-section of the corridor and applying the result obtained in chapter 3 recursively as in the TIM method of Brennan[14] would seem a natural idea to try to apply. Preliminary results for scattering from a two-dimensional terrain profile have been obtained but need to be confirmed to be applicable in an indoor environment.

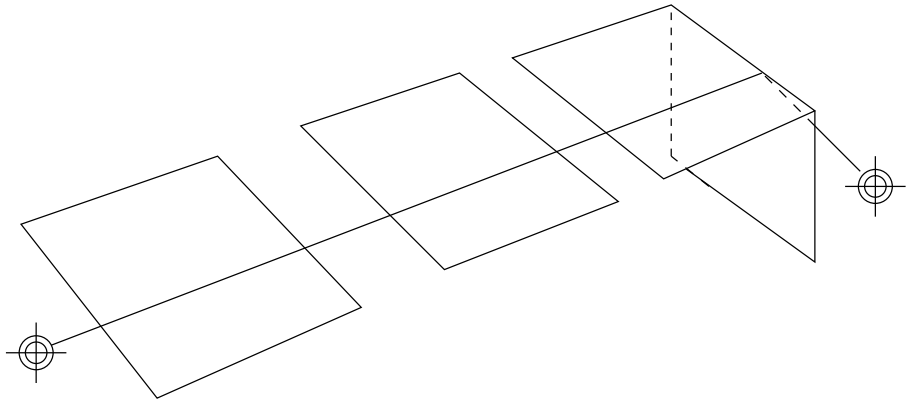

Figure B-1: A corridor with 2 doors and diffraction around the corner

B.3 Extensions to Convex Space Algorithm

The C++ software used to define the convex space algorithm, at the moment only allows for rectilinear shapes, but should be extended to include four vertex polyhedra and 6 vertex polyhedra. These will allow the building to be modelled more exactly. Also as mentioned in Chapter 4, the convex space representation of the building needs to be automated because at the moment it is input by hand. The algorithms for such an automation need to be succinct and cleverly written.

B.4 Tests on Software

The ray-tracing algorithms need to tested more thoroughly in a large building by an independent party so that the software can be altered to output information that meets the telecommunications industries needs.

Appendix C

Software Tool for Indoor Wireless Resource Optimsation (STIWRO) User Guide

C.1 Directory Hierarchy

The C++ software contained in the STIWRO project was created in Visual C++ version 6 using a single workspace containing many projects as shown in Figure C-1. The runtime workspace (*runtime.dsw*) contained in the runtime directory shown in Figure C-2 contains 20 projects in all. Some of these projects were created for test purposes to confirm that different parts of the software work correctly, or were used to generate specific results used in the thesis of Eamonn Kenny and as part of the software description. All C++ modules are stored in .cpp files in the directory STIWRO-C++ along with appropriate .h header files. The software was designed in such a way that all object files are shared between projects, in other words if one project is compiled and then another is compiled, the common object files are not recompiled if they remained unchanged in the intermediate period. This was easily achieved by setting the Release and Debug directories to be the same for each project. This is not the default setting in the Visual C++ software.

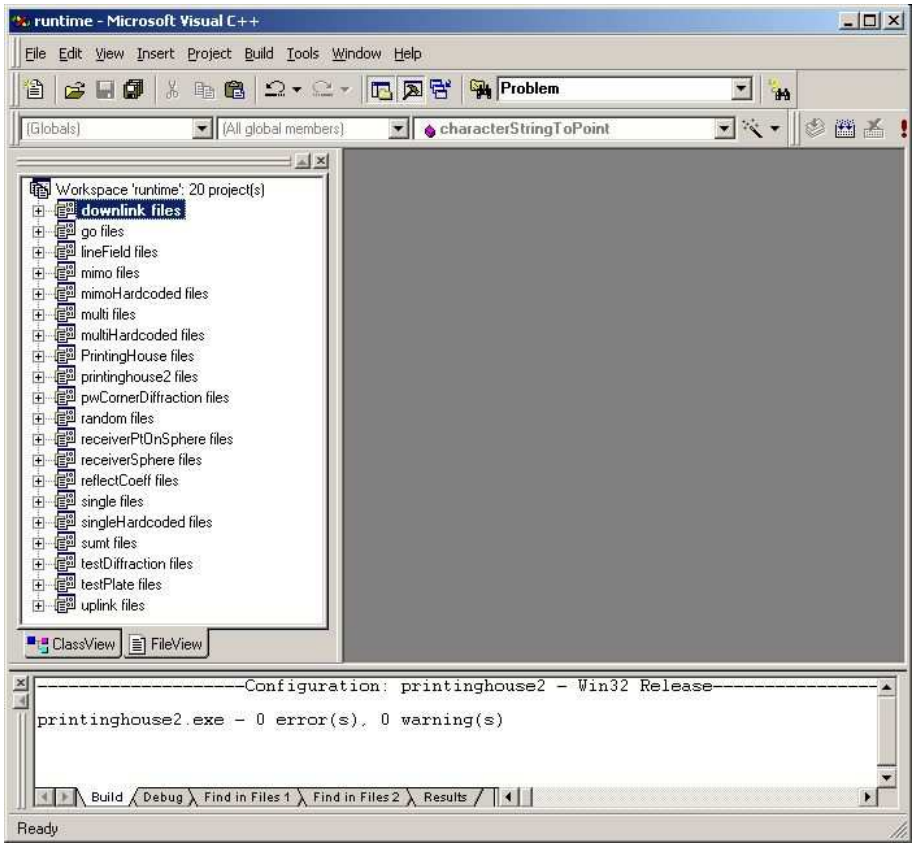

Figure C-1: The Visual C++ window containing all projects.

C.2 File Formats

C.2.1 Building Files

In the Runtime directory a large number of sample buildings and contained rooms exist for testing (see Figure C-2). They were created to use as inputs for the simulation of downlink and uplink optimisation algorithm, as well as sample ray-tracing code contained in approximately ten of the projects.

The input files for the building could be generated by AutoCAD if a DXF convertor was written to convert the files into the format required by the STIWRO tool. At present the files are built by hand. The building file containing all convex spaces, is defined to be a .dat file. The room connectivity is defined in the .roo file. The convex space information is stored as in Table C.1.

Note that the number of floors in this case is N+1 including the roof of the

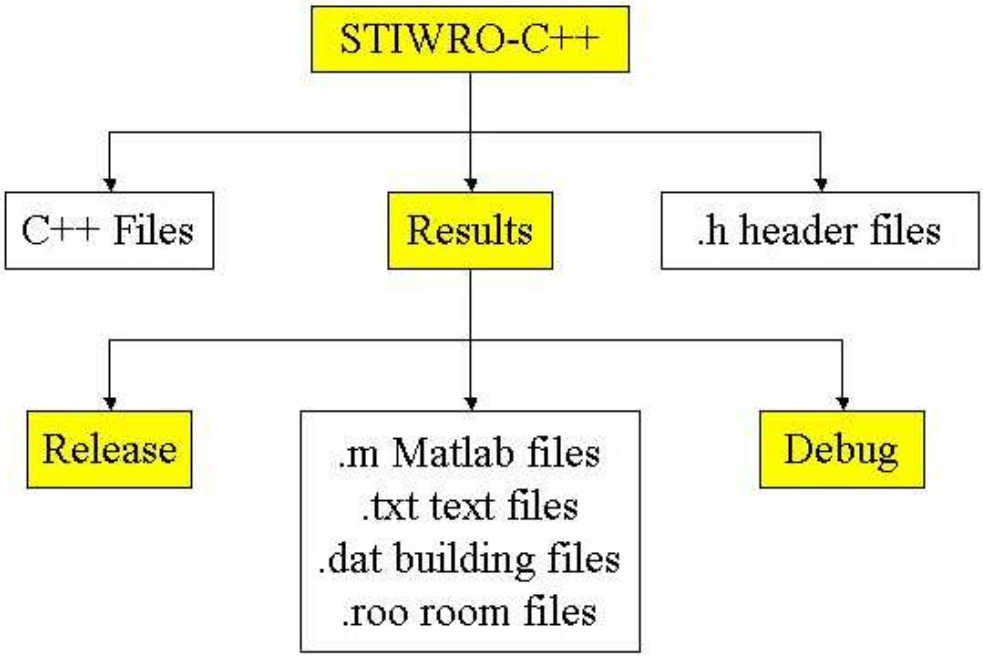

Figure C-2: The hierarchical structure for the project code.

building. The stories are interlaced between the floors. The building number is a number associated with the building. Each floor or story contains at least one filled convex space of the form is described as in Table C.2. <sometype> can be either Door, InteriorWall, ExteriorWall or Window. Defining a free convex space <sometype> takes on the value Room.

The storage of the room connectivity takes the form of Table C.3. The connections must be made to the floors above and below as well as the same floor so that it is easy to traverse from room to room.

The buildings once defined by the .dat and .roo files can be easily presented by Matlab. At present the software tool will send any story or floor of a building to an output file of the users choosing, by including one call to the story( ) or floor( ) methods in the C++ Matlab class contained in the Matlab.cpp file. The results in Figure C-3 are generated in this way, and then *story3d.m* is called from within Matlab to generate the three-dimensional building. Rotating the building shows the doors and windows more clearly. A breakdown of all the C++ projects will be presented in a later section.

Building	Building Number		
Floors	Number of Floors		
Stories	Number of Stories		
Floor	1		
...			
Story	1		
...			
Floor	N+1		
...			

Table C.1: The basic layout of the input building data file

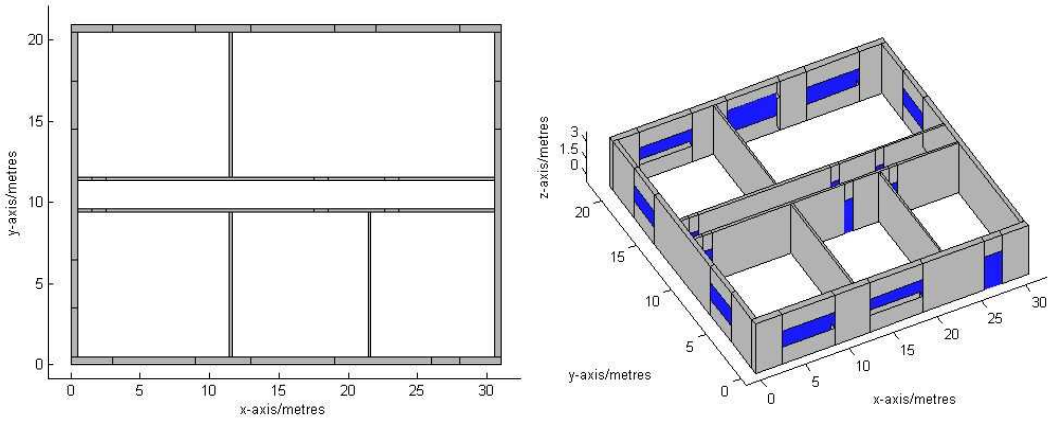

Figure C-3: A sample story of a building including doors, windows, exterior and interior walls.

C.2.2 Base Transceiver Station (BTS) files

The base transceiver station is a description of a general transmitter plus the requirements for the ray-tracing algorithm. The best way to describe the contents of the file is by providing an example as shown in Table C.4

Table C.4 contains a flag to say the file is a BTS file, an ID number, the region were the antenna is placed e.g: GraftonStreet, the location of the server, the default transmitting power, the frequency band, the orientation of the antenna specifying tilt and azimuth, the cost, the number of channels, the noise factor in the receiver at the BTS, the noise factor in the user equipment (UE), the maximum number of

Convex<sometype>			
	X1	Y1	Z1
	X2	Y1	Z1
	X2	Y2	Z1
	X1	Y2	Z1
	X1	Y1	Z2
	X2	Y1	Z2
	X2	Y2	Z2
	X1	Y2	Z2
DielectricParameters			
	Permittivity - ?	Permeability - ?	Conductivity - ?

Table C.2: The Structure of the input required to describe a filled convex space.

ROOM N		
BelowAdjacent1	BelowAdjacent2	$\cdots$
SameAdjacent1	SameAdjacent2	$\cdots$
AboveAdjacent1	AboveAdjacent2	$\cdots$

Table C.3: The connection of Room N to room in the same floor and below and above floors.

reflections in the ray-tracing, the maximum number of transmissions, the maximum number of diffractions, a flag to specify whether a point source or hertzian dipole is used, a random walk flag to specify whether a random mean is taken of the complex ray-paths when summed together, a corner diffraction flag to specify whether it is being used, the maximum capacity in the server, a diagram for the antenna, and a polar diagram not currently used in the present configuration.

C.2.3 Downlink and Uplink Optimisation Parameter File

The files are identical in layout for the definition of parameters necessary to run the uplink and downlink optimisation routines. Statistics must be give for voice, real-

time and non real-time data links. In each case Eb/No the energy per bit noise ratio must be specified, along with the fade margin and processing gain.

BTS	
001	
Region	
Location	(5.0,7.0,2.0)
Power	1
FrequencyBand	[900.0-900.0]
Orientation	$< 0, 0 >$
Cost	0
NumberOfChannels	1
NoiseFactorAtBTS	7.0
NoiseFactorAtUE	5.0
Reflections	3
Transmissions	4
Diffractions	1
HertzianDipole	0
RandomWalk	0
CornerDiffract	0
capacity	2.0
omni.diag	
polar.dat	

Table C.4: Sample BTS file

Interference Margin		
Voice Eb/No	Voice Fade Margin	Voice Processing Gain
Real Time Data Eb/No	Real Time Data Fade Margin	Real Time Data Processing Gain
Non Real Time Data Eb/No	Non Real Time Data Fade Margin	Non Real Time Data Processing Gain

Table C.5: Nokia Parameters File Layout

C.3 Running C++ Projects

C.3.1 Downlink Optimisation Project

Project	downlink
Main Caller	main-optimiseh.cpp
Input Files	foyer.dat foyer.roo bts2000.dat capacity.txt downlinkparam.dat
Output Files	location.txt newcells.txt bestserver2.txt
Matlab Runfiles	capacitygrid.m newbestserver.m

Table C.6: Downlink Project Description

The main calling function can be modified to allow the software to run for different buildings and parameter details. The input files are set at the moment to run the case of a foyer building (one single room) with capacity details defined in *capacity.txt*. The capacity file consists of 3 patches of high capacity. These patches are created and visualised using the Matlab runfile *capacitygrid.m* (see Figure 7-2). The software can then be run, and the results generated can be visualised using the Matlab runfile *newbestserver.m* (see Figure 7-4). The results generated contain the final positions of the base station locations upon completion of the downlink optimisation. Also, the best servers are indicated at each user equipment point that achieves its capacity requirement. If the capacity requirement is not met, then a black square indicates this since no best server exists.

C.3.2 Geometrical Optics (GO) Project

This project performs a comparison between a Hertzian dipole located over a large flat plate and the geometrical optics approach to the same problem. Assuming that no diffraction exist for each result, the plot of the pathloss coverage obtained by running the Matlab runfiles *gopathloss.m* and *spathloss.m* results in exactly the one values (see Figure 5-5).

Project	go
Main Caller	main-go.cpp
Input Files	largeplate.dat largeplate.roo bts1800.dat
Output Files	gopathloss.txt pathloss.txt
Matlab Runfiles	gopathloss.m spathloss.m

Table C.7: Geometrical Optics Project Description

C.3.3 Comparison of UTD versus Exact Solution (linefield) Project

Project	lineField
Main Caller	main-linefieldx.cpp
Input Files	plate.dat plate.roo bts900.dat
Output Files	linefieldx.txt reflectionfield.txt diffractionfield.txt incidentfield.txt linex.res
Matlab Runfiles	linefieldx.m

Table C.8: Linefield Project Description

This project performs a comparison between the UTD based ray-tracing solution over a small flat plate of size $6\lambda \times 6\lambda$ and the exact integral equation (IE) solution obtained by Conor Brennan[17] for the same plate. The pathloss is calculated along a line of length 120 metres with 1201 sample points. A very detailed set of results with many windows can be presented to the user by running the Matlab runfile *linefieldx.m*. The plots show the incident field, reflected field and diffracted fields in isolation. There is also a plot of the total scattered field from both the ray-tracing and the exact solution. A large disagreement is obtained (see Figure 3-16) that is explained in the software description[46].

Project	mimoh
Main Caller	main-mimo.cpp
Input Files	<user_defined_building>.dat <user_defined_building>.roo bts<user_defined>.dat points.dat
User Define Flags	Gaussian Random Variable = On/Off
Output Files	raypaths_i_j.txt
Matlab Runfiles	none

Table C.9: MIMO Project Description

C.3.4 Multiple Input Multiple Output (MIMO) Project (Standalone Version)

The multiple input, multiple output (MIMO) project was created specifically for a Socrates student project written by Maurizio Salvino. In his project he was required to set up a number of transmitters that would send signals to one another. This C++ project was created specifically for his purposes. It outputs the ray-paths *raypaths_i_j.txt* from transmitter i to transmitter j. A point to point result is calculated in all cases. If i is transmitting to j then it is assumed that the calculation of j back to i is reflective, so that it can be neglected. The main function *main-mimo.cpp* provides a standalone executable that can be run from within Matlab for a number of different building or BTS files. A flag can be set from the command line or from within Matlab so that the ray-paths are multipled by a random phase or left unchanged.

C.3.5 Multiple Input Multiple Output (MIMO) Project (Hard-coded Version)

This multiple input, multiple output (MIMO) project was created specifically for tests required by Eamonn Kenny to ensure that the software delivered to Maurizio Salvino was working correctly. Instead of using user defined buildings and BTS files, specific files are hard-coded into the main function call *main-mimoh.cpp*. The

Project	mimoHardcoded
Main Caller	main-mimoh.cpp
Input Files	building.dat building.roo bts900.dat points.dat
Output Files	raypaths_i_j.txt
Matlab Runfiles	none

Table C.10: MIMO Hard-Coded Project Description

building file *building.dat* and *bts900.dat* are the hard-coded files. There is no random phase multiplication in the results as in the previous standalone version.

C.3.6 Point to Multi-Point (multi) Project (Standalone Version)

Project	multi
Main Caller	main-multi.cpp
Input Files	<user_defined_building>.dat <user_defined_building>.roo bts<user_defined>.dat
Output Files	pathloss.txt
Matlab Runfiles	pathloss.m

Table C.11: Multi-Point Coverage Project Description (Standalone)

This project is used to present coverage on a rectangular grid for a single transmitter. The building and BTS files are defined by a user from the command line or from within a Matlab runfile.

C.3.7 Point to Multi-Point (multi) Project (Hard-Coded Version)

This project provided a multi-point calculation resulting in a path-loss coverage plot for a given transmitter and receiver hardcoded into *main-multih.cpp*. The Matlab runtime file *pathloss.m* produces a coverage plot that overlays the building walls.

Project	multiHardCoded
Main Caller	main-multih.cpp
Input Files	building.dat building.roo bts900.dat
Output Files	pathloss.txt
Matlab Runfiles	pathloss.m

Table C.12: Multi-Point Coverage Project Description (Hard-coded)

All walls are set to be transparent so that the path-loss can be seen clearly, and to emphasise the fall off in signal as the signal propagates through the walls (see Figure 5-7. This is probably the most descriptive and well presented plot that the communications group at Trinity have produced, and yet was very easy to generate due to the power of the Matlab engine.

C.3.8 Printing House Measurement Set 1 Project

Project	PrintingHouse
Main Caller	main-printing.cpp
Input Files	printinghouse.dat printinghouse.roo bts1000.dat conornodoors.dat conorclosed.dat measurementoffice.dat
Output Files	corridoropendoor1.txt corridoropendoor2.txt corridorclosed1.txt corridornodoors.txt
Matlab Runfiles	measureoffice.m aspect3d.m

Table C.13: Printing House Measurement Campaign (Hard-coded)

This project provided a point calculation of path-loss in a corridor for comparison with that obtained by measurement set 1. The Matlab runtime file *measureoffice.m* produces a coverage plot that overlays all results as presented in Figure 5-10. The runtime file *aspect3d.m* presents the building, transmitter, receiver points and convex space centres as shown if Figure 5-8.

C.3.9 Printing House Measurement Set 2 Project

Project	PrintingHouse2
Main Caller	main-printing2.cpp
Input Files	printingclosed.dat printingclosed.roo bts1000.dat
Output Files	corridorclosedR1.txt corridorclosedR1RW.txt corridorclosedR3.txt corridorclosedR3RW.txt
Matlab Runfiles	measureacross.m aspect3d.m

Table C.14: Printing House Measurement 2 Campaign (Hard-coded)

This project provided a point calculation of path-loss in a corridor for comparison with that obtained by measurement set 2. The Matlab runtime file *measureacross.m* produces a coverage plot that overlays all results as presented in Figure 5-13. The runtime file *aspect3d.m* presents the building, transmitter, receiver points and convex space centres as shown if Figure 5-12.

C.3.10 Corner Diffraction with Far Field Scattering Project

Project	pwCornerDiffraction
Main Caller	main-linediag.cpp
Input Files	plate.dat plate.roo bts750.dat
Output Files	diffractionfield.txt
Matlab Runfiles	cornerdiff.m

Table C.15: Far Field Corner Diffraction Description

This routine attempts to generate the results of McNamara[58] for the far field pattern generated by a flat plate with a monopole plated at the centre. The scattered field points are generated along a diagonal hemisphere from the plate. The plate *plate.dat* used in other projects was retained for this sample problem, although the frequency was altered so that the problem would give exactly the same results at that obtained by McNamara. The corner diffraction option is turned on in *bts750.dat*. The

Matlab runfile *cornerdiff.m* is used to generate the far field results shown in Figure 2-11.

C.3.11 Random Number Generator Project

Project	random
Main Caller	main-random.cpp
Input Files	none
Output Files	none
Matlab Runfiles	none

Table C.16: Random Number Generator Description

This function is a simple program to test the generation of random variables using a time dependant seed to ensure that the generator is sufficiently random.

C.3.12 Field Strength at Receiver due to a Point on a Sphere Project

Project	receiverPtOnSphere
Main Caller	main-ptonsphere.cpp
Input Files	plate.dat plate.roo bts900.dat
Output Files	reflections.txt diffractions.txt
Matlab Runfiles	sreflection.m sraytrace.m sdiffraction.m

Table C.17: Transmitter Point on Sphere Description

This is a single point to point path-loss calculation performed between a point on a sphere and some receiver point, both hard-coded into the main caller *main-ptonsphere.cpp*.

Project	receiverSphere
Main Caller	main-sphere.cpp
Input Files	plate.dat plate.roo bts900.dat
Output Files	pathloss.txt
Matlab Runfiles	pathloss.m

Table C.18: Field Strength on Sphere Description

C.3.13 Field Strength at Receiver Points on a Sphere Project

This is a point to multi-point path-loss calculation performed between a point on a sphere and many receiver points on a hemisphere, both hard-coded into the main caller *main-sphere.cpp*.

C.3.14 Reflection Coefficients Project

Project	reflectCoeff
Main Caller	reflectCoeff.cpp
Input Files	none
Output Files	singleReflect.txt singleTransmission.txt infiniteReflect.txt correctedReflect.txt infiniteTrans.txt correctedTrans.txt infiniteReflectPS.txt geometry.txt infiniteReflectPW.txt meanInfinitePS.txt r*.txt t*.txt
Matlab Runfiles	reflectCoeff.m runPWvsPS.m balanisref.m runExactDielvsSingle.m runExactDielvsSingleFar.m runExactvsBurnside.m

Table C.19: Reflection Coefficients Description

This is probably the most detailed project of them all. It contains a large amount of result files used to make comparisons between a full ray-tracing solution, single reflection solution and Burnside's solution[18] for internal reflections in a slab. There are a large number of Mablab runfiles. The runfile *reflectCoeff.m* provides a plot as in Figure C-4 of the single reflection results and infinite reflection results obtained by

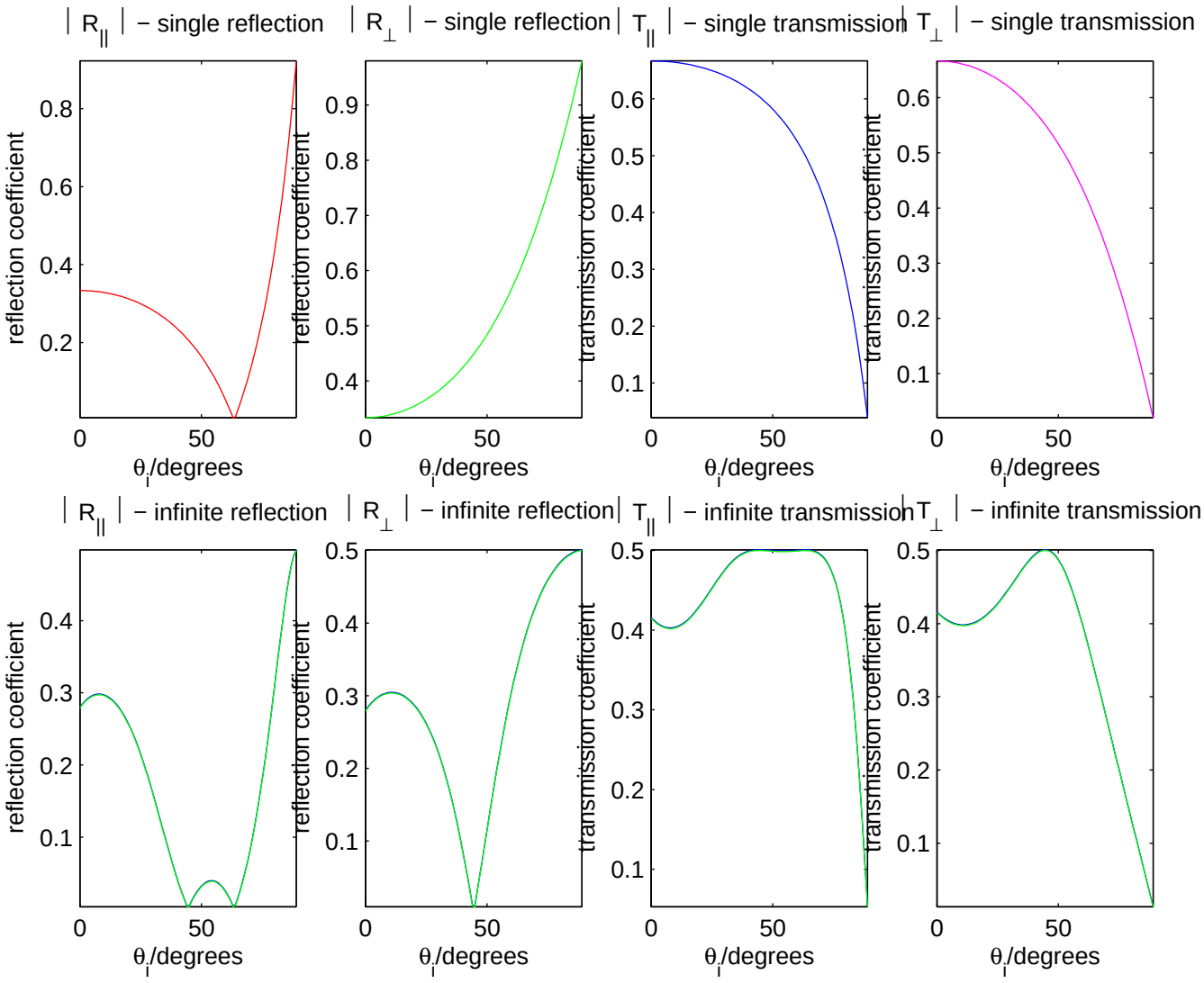

Figure C-4: Single versus Infinite reflection and transmission coefficients.

using the single reflection result file *singlereflection.txt* and *infiniteReflect.txt*. Likewise the transmission results are obtained from *singleTransmission.txt* and *infiniteTrans.txt*. Results for the comparison of single reflection, Burnside and ray-tracing are presented using *runExactvsBurnside.m* and the results are shown in Figure 3-6. Results for the lossy case can be presented using *runExactDielvsSingle.m* for a point close to a plate, and *runExactDielvsSingleFar.m* for a point far from a plate. The results of Balanis[7] for the reflection and transmission coefficients can be generated by setting different permittivities ϵ within *reflectCoeff.cpp* and then generating a file r<number>.txt and t<number>.txt representing the reflection and transmission co-

efficients for a given permittivity=<number>. The runfile *balanisref.m* expects that the all files are created for a varying number of permittivities, the values of which are $\epsilon = 2.56, 4, 9, 25, 81$.

C.3.15 Single Point to Point Ray-Tracing Project (Standalone Version)

Project	single
Main Caller	main-single.cpp
Input Files	<user_defined_building>.dat <user_defined_building>.roo bts<user_defined>.dat
Output Files	reflection.txt diffraction.txt
Matlab Runfiles	sraytrace.m sdiffraction.m

Table C.20: Point to Point Description

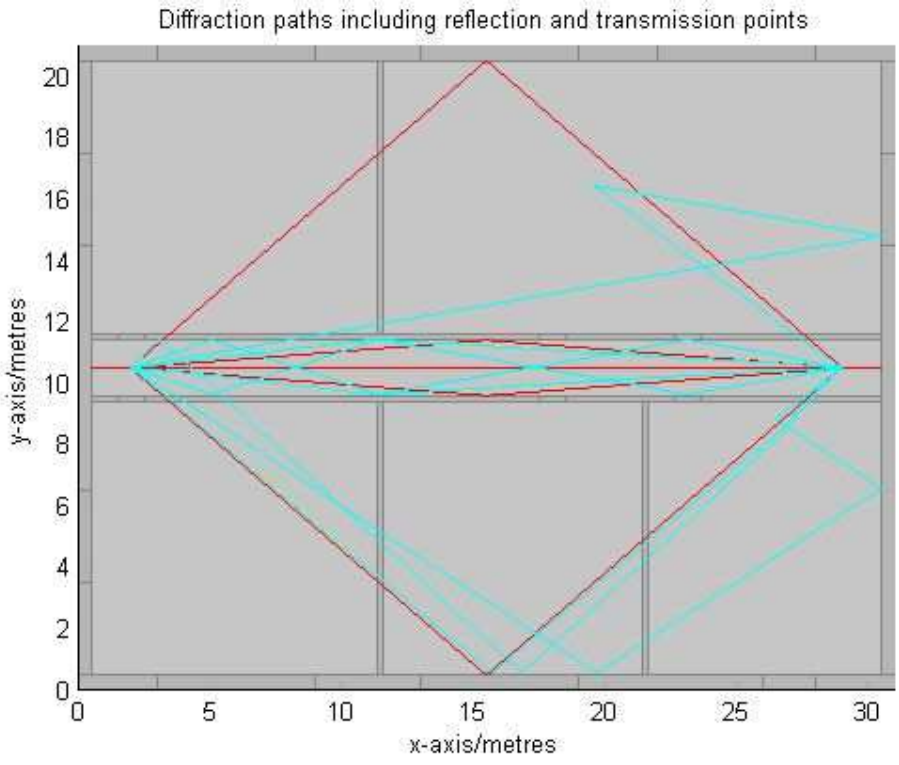

Figure C-5: Diffraction paths between two points.

This is a standalone version of a point to point path-loss calculation performed for a user defined building and BTS file. At the moment the transmitter and receiver are hard-coded, although this could be easily changed. The results are presented for all reflected rays using *sraytrace.m*. The diffraction paths are presented using *sdiffraction.m* as show in Figure C-5.

C.3.16 Single Point to Point Ray-Tracing Project (Hard-coded Version)

Project	singleHardcoded
Main Caller	main-singleh.cpp
Input Files	building.dat building.roo bts900.dat
Output Files	reflection.txt diffraction.txt
Matlab Runfiles	sraytrace.m sdiffraction.m sreflection.m

Table C.21: Point to Point Hardcoded Description

This is a hardcoded version of a point to point path-loss calculation performed for a given building and BTS file. At the moment the transmitter and receiver and hardcoded into the main caller. The code can be run and the reflections presented from within Matlab all at the same time, using *sreflection.m*. This is achieved by using a DOS call from within Matlab to the executable *singleHardcoded.exe* located in the Release directory of the runtime directory (see Figure C-2 for the directory layout).

C.3.17 Sequential Unconstrained Minimisation Technique (SUMT) Project

This project contains a simple linear programming problem with two unknowns and 7 constraints described by Beasley [8]. The starting solution is a point (x_0, y_0) representing the two unknowns as they would appear on a cartesian plane. The initial guess is moved using a path-following algorithm until the optimisation solution is

Project	sumt
Main Caller	main-sumt.cpp
Input Files	none
Output Files	sumt.txt
Matlab Runfiles	sumt.m

Table C.22: SUMT Description

found. All the points along the path are sent to *sumt.txt*. The Matlab runfile *sumt.m* is then used to plot the region of feasibility and shows the convergence of the solution to it's optimal point $(12/7, 20/7)$ as in Figure 6-2.

C.3.18 Diffraction Testing Project

Project	testDiffraction
Main Caller	main-diffraction.cpp
Input Files	none
Output Files	diffract.txt diffract2.txt
Matlab Runfiles	sumt.m

Table C.23: Diffraction Testing Description

This project is used to test that the UTD diffraction coefficients used in the ray-tracing agree with results obtained from a Matlab code. They were shown to be the same in all cases. The Matlab code was written by Derek Bell long before the C++ code was written.

C.3.19 Receiver Grid over Flat Plate Project

This project was set up just like the linefield project mentioned earlier in this Chapter, except that instead of presenting points along a line, the results are presented on a uniform rectangular grid, allowing them to be plotted using *pathloss.m*. This project is very similar also to the *multih* project mentioned previously in this Chapter also.

Project	testPlate
Main Caller	main-testPlate.cpp
Input Files	plate.dat plate.roo bts900.dat
Output Files	pathloss.txt
Matlab Runfiles	pathloss.m

Table C.24: Receiver Grid over Flat Plate Description

C.3.20 Uplink Optimisation Algorithm Project

Project	uplink
Main Caller	main-uplink.cpp
Input Files	foyer.dat foyer.roo bts2000.dat capacity.txt uplinkparam.dat
Output Files	pathloss.txt
Matlab Runfiles	pathloss.m

Table C.25: Uplink Optimisation Description

This project uses the results obtained by a downlink optimisation algorithm to see how many users can possibly connect to the system by calculating the solution N times and then calculating the average number of connections for those N solutions. The result is a number which is printed for the user to see.

Bibliography

[1] M. A. Abdel Moneum, Z. Shen, J. L. Volakis, "Hybrid PO-MoM Analysis of Large Axi-Symmetric Radonnes", IEEE Trans. Ant. Prop., Vol. 49, No. 12, Dec, 2001.

[2] K. R. Aberegg and A. F. Peterson, " Integral Equation Asymptotic Phase Method to Two-Dimensional Scattering", IEEE Trans. Antennas and Prop., Vol.43, No.5, 1995.

[3] M. Abramowitz, I. Stegun, Handbook of Mathematical Functions with formulas, graphs, and Mathematical Tables, ISBN 0900492325, New York: Dover Publications, 1965.

[4] I. Adler, N. Karmarkar, M. G. C. Resende, G. Veiga, "An Implementation of Karmarkar's Algorithm for Linear Programming", Mathematical Programming, Vol. 44, pp. 297-335, 1989b.

[5] F. A. Agelet, A. Formella, J. M. H. Rabanos, F. I. de Vicente, F. P. Fontan, "Efficient ray-tracing acceleration techniques for radio propagation modelling", IEEE Trans. Veh. Tech., Vol. 49, pp.2089-2104, Nov. 2000.

[6] J. B. Andersen, University of Aalborg: Personal Communication, Published IEEE AP, Jan. 1995, (1993).

[7] C. A. Balanis, Advanced Engineering Electromagnetics, ISBN 0471621943, pp. 793-796, New York: Wiley, c1989.

[8] J. E. Beasley, Two Mines Company Example, Operations Research Course Notes, http://mscmga.ms.ic.ac.uk/jeb/or/basicor.html

[9] J. E. Berg and H. Holmquist, "An FFT Multiple Half-Screen diffraction Model", Proc. IEEE VTC94 Stockholm, Sweden, pp. 195-199, 1994.

[10] J. Bittner, P. Wonka and M. Wimmer, "Visibility preprocessing for urban scenes using line space subdivision", Computer Graphics and Applications, 2001. Proceedings. Ninth Pacific Conference on, pp. 276-284, 2001.

[11] M. Born, E. Wolf, "Principles of Optics: Electromagnetic Theory of Propagation Interference and Diffraction of Light", ISBN: 0080264824, 6th Ed., Oxford: Pergamon, 1980.

[12] S. Boyd, L. Vandenberghe, "Convex Optimization", A draft for a book to be published in 2003. http://www.stanford.edu/~boyd/cvxbook.html

[13] C. Brennan and P. J. Cullen, "Application of the Fast Far-FieldApproximation to the computation of UHF path loss over irregular terrain", IEEE Trans. Ant. Prop. Vol. 46, No. 6, 1998.

[14] C. Brennan and P. J. Cullen, "Tabulated Interaction Method for UHF terrain propagation problems", IEEE Trans. Ant. Prop. Vol. 46, No. 5, pp. 738-739, 1998.

[15] C. Brennan and P. J. Cullen, "Multilevel Tabulated Interaction Method applied to UHF propagation over irregular terrain", Submitted to IEEE Trans Antennas and Prop., 1999.

[16] C. J. Brennan, P. J. Cullen, L. Rossi, "An MFIE-based Tabulated Interaction Method for UHF terrain propagation problems"

[17] C. Brennan and P. J. Cullen, "A Novel Iterative Solution to the Three-Dimensional Electric Field Integral Equation", ICEAA03, Torino, Italy, Sept, 2003.

[18] W. D. Burnside, K. W. Burgener, "High Frequency Scattering by a Thin Lossless Dielectric Slab", IEEE Trans. Ant. Prop. Vol. 31, No. 1, pp.104-110, Jan 1983.

[19] F. A. Sikta, W. D. Burnside, T-T. Chu, L. Peters. Jr., "First Order Equivalent Current and Corner Diffraction Scattering from Flat Plate Structures", IEEE Trans. Ant. Prop. Vol. 31, No. 4, pp. 584-589, July 1983.

[20] C. R. Cockrell, F. B. Beck, "Note on Use of Slope Diffraction for Aperture Antennas on Finite Ground Plane", NASA TEhnical Memorandum 110192, NASA Langley Research Center, Hampton, Virginia, August, 1995.

[21] I. De Coster, "Deterministic Propagation Prediction for Wireless Communication Systems", Thesis, Katholieke Universiteit Leuven, October 2000.

[22] E. Di Giampaolo, F. Bardati,"A Method for Multiple Diffracted Ray Sampling in Forward Ray-tracing", Ant. Prop. Society, 2001 IEEE Int. Sym., Vol. 1, pp. 468-471, July, 2001.

[23] H. M. El-Sallabi, G. Liang, H. L. Bertoni, I. T. Rekanos, P. Vainikainen, "Influence of Diffraction Coefficient and Corner Shape on Ray Prediction of Power and Delay Spread in Urban Microcells", IEEE Trans. Ant. Prop. Vol. 50, No. 5, May 2002.

[24] D. Erricolo, G. D'Elia, P. L. E. Uslenghi, "Measurements on Scaled Models of Urban Environments and Comparisons With Ray-Tracing Propagation Simulation", IEEE Trans. Ant. Prop., Vol. 50, No. 5, May 2002.

[25] T. Funkhouser, I. Carlbom, G. Elko, "A Beam Tracing Approach to Acoustic Modelling for Interactive Virtual Environments", ISBN: 0-89791-999-8, Proc. 25th Int. Conf. on Computer Graphics and Interactive Techniques, pp. 21-32, 1998.

[26] G. H. Golub, C. F. Van Loan Matrix Computations, ISBN 0946536058, Oxford: North Oxford Academic, 1983.

[27] C. C. Gonzaga, "Path-following Methods for Linear Programming", Siam Review, Vol. 34. No. 2, pp. 167-224, June 1992.

[28] R. C. Hansen, ed., *Moment Methods in Antennas and Scattering.* Artech, Boston London, 1990.

[29] R. F. Harrington, "Field Computation by Moment Methods", New York, Macmillan, 1968.

[30] M. Hassan-Ali, K. Pahlavan, "A New Statistical Model for Site-Specific Indoor Radio Propagation Prediction Based on Geometric Optics and Geometric Probability", IEEE Trans. Wireless Comm., Vol. 1, No. 1, pp. 112-124, Jan 2002.

[31] P. D. Holm, "UTD-Diffraction Coefficients for Higher Order Wedge Diffracted Fields", Vol. 44, No. 6, pp. 879-888, June, 1996.

[32] H. Inanoglu, E. Topuz, "Hybrid Ray-Mode Modelling of Indoor Propagation for Wireless Applications", 6th IEEE Int. Symp. on Personal Indoor and Mobile Radio Communications", Vol. 3, pp. 1186-1189, 1995.

[33] A. Ishimaru, "Electromagnetic Wave Propagation, Radiation and Scattering", ISBN 0132490536, London: Prentice-Hall, pp. 346-347, 1991.

[34] U. Jakobus, F. M. Landstorfer, "Improvement of the PO-MoM Hybrid Method by Accounting for Effects of Perfectly Conducting Wedges", IEEE Trans. Ant. Prop., Vol. 43, No. 10, pp. 1123-1129, October, 1995.

[35] U. Jakobus, F. M. Landstorfer, "Improved PO-MM Hybrid Formulation from Three-Dimensional Prefectly Conducting Bodies of Arbitrary Shape", IEEE Trans. Ant. Prop., Vol. 43, No. 2, pp. 162-169, Feb, 1995.

[36] U. Jakobus, F. M. Landstorfer, "Improved Physical Optics Approximation for Flat Polygonal Scattering", Institut für Hochfrequenztechnik, University of Stuttgart, Germany.

[37] G. L. James, "Geometrical Theory of Diffraction for Electromagnetic Waves, 3rd Edition", ISBN 0901223832, Stevenage: Peregrinus, pp. 153-154, 1976.

[38] Janaswamy, J. B. Andersen, "Path-loss prediction in urban areas with irregular terrain topography", COST 259 TD(98)060.

[39] Z. Ji, B-H. Li, H-X. Wang, H-Y. Chen, T. K. Sarkar, "Efficient Ray-Tracing Methods for Propagation Prediction for Indoor Wireless Communications", IEEE Ant. Prop. Mag., Vol. 43, No. 2, pp. 41-49, Apr 2001.

[40] P. M. Johansen, "Uniform Physical Thoery of Diffraction Equivalent Edge Currents for Truncated Wedge Strips", IEEE Trans. Ant. Prop., Vol. 44, No. 7, pp. 989-995, July, 1996.

[41] D. S. Jones, "Methods in Electromagnetic Wave Propagation", ISBN 0198562624, 2nd Edition, New York: Clarendon Press, Oxford University Press, 1994.

[42] J. B. Keller "Geometical theory of diffraction," J. Opt. Soc. Amer., Vol. 52, No. 2 pp. 116-130, Feb 1962.

[43] E. Kenny, P. J. Cullen "Fast numerical calculation of UHF propagation over two-dimensional dielectric irregular terrain using an integral equation method", Proceedings IEEE Vehicular Technology Conference VTC 97, ISBN 0-7803-3659-3, pp. 1118-1121, June 1997.

[44] E. Kenny, P. J. Cullen "Automatic model selection scheme for propagation in macrocellular and microcellular environments", Proceedings IEEE Vehicular Technology Conference VTC 99, May 1999.

[45] E. M. Kenny and P. J. Cullen, "A hybrid Geometrical Optics, Integral Equation propagation model for fast accurate UHF propagation computation in urban microcells", Submitted to VTC 99, Houston.

[46] E. M. Kenny, "Software Description: Final Report for Software Tool for Indoor Wireless Resource Optimisation", Delivered to Enterprise Ireland, Sept, 2003.

[47] M. Kline, "An asymptotic solution of Maxwell's equations," in The Theory of Electromagnetic Waves, Interscience, New York, 1951.

[48] E. F. Knott, J. F. Shaeffer, M. T. Tuley, "Radar Cross Section", 2nd Ed., Chapter 5, Boston; London: Artech House, 1993.

[49] R. G. Kouyoumjian "The geometrical theory of diffraction and its applications," *in Numerical and Asymptotic Techniques in Electromagnetics*, R. Mittra (Ed.), Springer, New York, Chapter 6, h1975.

[50] S. Kandukuri, S. Boyd, "Simultaneous Rate and Power Control in Multirate Multimedia CDMA Systems", IEEE 6th Int. Symp. on Spread-Spectrum, NJ, USA, Spet. 2000.

[51] R. G. Kouyoumjian, P. H. Pathak "A Uniform Geometrical Theory of Diffraction for an Edge in a Perfectly Conducting Surface", Proc. IEEE, pp. 1448-1460, Vol. 62, No. 11, Nov, 1974.

[52] J. Laiho, A. Wacker, T. Novosad, "Radio Network Planning and Optimisation for UMTS", ISBN 0471486531, Chichester, Wiley, 2002.

[53] D. L. Laurenson, "Indoor Radio Channel Propagation Modelling by Ray-Tracing Techniques", PhD Thesis, University of Edinburgh, 1994.

[54] C. C. Lu and W. C. Chew, "Fast Far Field Approximation for Calculating the RCS of Large Objects", Micro. Opt. Tech. Lett. Vol. 8, No. 5, pp. 238-241, 1995.

[55] W. C. Chew, J-M. Jin, E. Michielssen, J. Song "Fast and Efficient Algorithms in Computational Electromagnetics", ISBN 1-58053-152-0, pp. 20-22, Artech House, London, 2001.

[56] R. K. Luneberg, "Mathematical theory of optics," Brown University Notes, Providence, RI, 1944.

[57] M. Martínez-Búrdalo, A. Martín, R. Villar, "Unifrom PO and PTD Solution for Calculating Plane Wave Backscattering from a Finite Cylindrical Shell of Arbitrary Cross Section", IEEE Trans. Ant. Prop., Vol. 41, No. 9, Sept, 1993.

[58] D. A. McNamara, C. W. I. Pistorius, J. A. G. Malherbe, "Introduction to The Uniform Theory of Diffraction", Artech House, London, 1990.

[59] A. Michaeli "Equivalent Edge Currents for Arbitrary Aspects of Observation," IEEE Trans. Ant. Prop. Vol. AP-32, No. 3, March, 1984.

[60] A. Michaeli "Elimination of Infinities in Equivalent Edge Currents, Part I: Fringe Current Components", IEEE Trans. Ant. Prop., pp. 912-918, Vol. 34, No. 7, July, 1986.

[61] A. Michaeli "Elimination of Infinities in Equivalent Edge Currents, Part II: Fringe Current Components", IEEE Trans. Ant. Prop., pp. 1034-1037, Vol. 34, No. 8, August, 1986.

[62] A. Michaeli Comments on "First-Order Equivalent Current and Corner Diffraction Scattering from Flat Plate Structures", IEEE Trans. Ant. Prop., pp. 1011-1012, Vol. 32, No. 9, September, 1984.

[63] D. T. Moroney and P. J. Cullen, *A Fast Integral Equation Approach to UHF Coverage Estimation,* In Mobile and Personal Communications, Ed. E. Del Re, Elsevier, 1995.

[64] D. T. Moroney and P. J. Cullen, "The Green's Function Perturbation Method for the solution of Electromagnetic Scattering Problems", Progress In Electromagnetic Research, PIER 15, pp. 221- 252, 1997.

[65] L. O. Brien, E. Kenny and P. J. Cullen, "An efficient implementation of a three-dimensional propagation tool for indoor and outdoor urban environments", Submitted to IEEE Trans. Veh. Tech. 1999.

[66] P. H. Pathak and R. G. Kouyoumjian, "The dyadic diffraction coefficient for a perfectly conducting wedge", Technical Report 2183-4 (AFCRL-69-0546), Ohio State University, ElectroScience Lab., 1970.

[67] M. J. D. Powell, "Restart Procedures for the Conjugate Gradient Method", Mathematical Programming, pp. 241-254, North-Holland Publishing Co., 1977.

[68] W. H. Press, S. Teukolsky, W. T. Vetterling, B. P. Flannery, Numerical Recipes in C, 2^{nd} Edition, ISBN 052135465X, Cambridge University Press, 1992.

[69] S. Rao, D. Wilton, D. Glisson, "Electromagnetic Scattering by Surfaces of Arbitrary Shape", IEEE Trans. Ant. Prop, Vol. 30, No. 3, pp. 409-418, May 1982.

[70] S. Y. Seidel, T. S. Rappaport "914 MHz Path Loss Prediction Models for Indoor Wireless Communications in Multi-floored Buildings", IEEE Trans. Ant. Prop., Vol. 40, No. 2, Feb 1992.

[71] H. D. Sherali, C. M. Pendyala, T. S. Rapport"Optimal Location of Transmitters for Micro-Cellular Radio Communication System Design", IEEE Jour. on Selected Areas in Communications, Vol. 14, No. 4, May 1996.

[72] L. Rossi, "Efficient Methods for the Computation of High Frequency Electromagnetic Wave Scattering from Piecewise Smooth Surfaces using the Integral Equation Formulation", PhD Thesis, University of Dublin, 1999.

[73] D. N. Schettino, D. H. D. Carvalho, F. J. S. Moreira, "An Efficient Algorithm for Radiowave Coverage Prediction in Urban Microcells", IEEE International Telecommunications Symposium (ITS2002), Natal, RN, Brazil, September 2002.

[74] M. Schneider, R. J. Luebbers, "A General, Uniform Double Wedge Diffraction Coefficient", IEEE Trans. Ant. Prop., Vol. 39, No. 1, Jan 1991.

[75] R. A. Shore, A. D. Yaghjian, "Shadow Boundary Incremental Length Diffraction Coefficients Applied to Scattering from 3-D Bodies", IEEE Trans. Ant. Prop., pp. 200-210, Vol. 49, No. 2, Feb, 2001.

[76] L. Stola, P. Tenani, G. L. Urso, "Indoor Propagation: Experimental Validation at 1.7GHz of a UTD-Based Approach", Wireless Personal Communications, pp. 225-241, Vol. 3, No. 3, 1996.

[77] S. Takahashi, Y. Yamada, K. Ogura, "BER Estimation with Random Phase Summation Applied to Ray Tracing", 48^{th} IEEE VTC 98, pp. 855-859 May, 1998.

[78] S. Takahashi, K. Taira, Y. Yamada, "Estimation of Multipath Propagation Characteristics Using Ray Tracing with Random Phase Summation", Proc. APCC 97 3rd Pacific Conf. Comm., pp. 558-562, Vol. 1, No. 1, 1997.

[79] K. P. Thakur, W. S. Holmes, "Reflection of Plane Wave from Multi-layered Dielectrics", Microwave Conference, Asia-Pacific, Tapai, 2001.

[80] R. Tiberio, G. Pelosi, G. Manara, P. H. Pathak, "High-frequency scattering from a wedge with impedance faces illuminated by a line source– Part I: Diffraction", IEEE Trans. Ant. Prop, Vol. 37, pp. 212-218, Feb 1989.

[81] R. P. Torres, L. Valle, M. Domingo, S.Loredo, M. C. Diez, "CINDOOR: An Engineering Tool for Planning and Design of Wireless Systems in Enclosed Spaces", IEEE Ant. Prop. Mag., pp. 11-22, Vol. 41. No. 4, August 1999.

[82] P. Y. Ufimtsev "Method of edge waves in the physical theory of diffraction," translated by U.S Air Force Foreign Technology Division, Wrght-Patterson AFB, OH, September 1971.

[83] P. Y. Ufimtsev Comments on "Improvement of the PO-MoM Hybrid Method by Accounting for Effects of Perfectly Conducting Wedges", IEEE Trans. Ant. Prop., pp. 1440, Vol 45., No. 9, September, 1997.

[84] A. D. Yaghjian, "Incremental Length Diffraction Coefficients for Arbibrary Cylindrical Scatters", IEEE Trans. Ant. Prop. pp. 1025-1032, Vol. 49, No. 7, July, 2001.

[85] L. Yin, J. Wang, W. Hong, "A Novel Algorithm Based on the Domain-Decomposition Method for the Full-Wave Analysis of 3-D Electromagnetic Problems", IEEE Trans. Ant. Prop., pp. 2011-2017, Vol. 50, No. 8, August, 2002.

[86] Z. Yun, Z. Zhang, M.F. Iskander, "A ray-tracing method based on the triangular grid approach and application to propagation prediction in urban environments", IEEE Trans. Antennas and Prop., Vo. 50, No. 5, pp. 750-758, May, 2002.